UNIVERSITÀ DEGLI STUDI DI PADOVA

Department of Civil, Environmental and Architectural Engineering

Master’s Degree Programme in Water and Geological Risk Engineering

MASTER’S THESIS

Soil Characterization and Sensor Performance Evaluation of a Monitored Levee Section in San Giorgio al Tagliamento

Candidate

Mahmoud Aly Hassan Elshanawany

Matricola: 2112181

Supervisor

Prof. Francesca Ceccato

Academic Year 2025/2026

Table of Contents

List of Figures

List of Tables

Chapter 1 Introduction

1.1 Background and motivation

River embankments play a fundamental role in flood-risk mitigation by protecting settlements, agricultural land, infrastructure, and economic activities located in low-lying floodplain areas. Their safety and long-term performance depend not only on their geometry and construction materials, but also on the hydraulic and mechanical processes that develop within the embankment body and its foundation over time. Among these processes, transient seepage, rainfall infiltration, groundwater fluctuations, and unsaturated soil response are especially important because they directly affect pore-water conditions, suction, water content, and, consequently, the stability and serviceability of the structure. The interpretation of these processes has become increasingly relevant in the context of climate variability, extreme hydrological events, and the need for more reliable levee-management strategies.

In recent years, field monitoring has become one of the most valuable tools for investigating the real behaviour of embankments under natural conditions. Time-series measurements from tensiometers, hygrometers, piezometers, and rainfall gauges make it possible to observe how an embankment responds to environmental forcing such as rainfall and river-stage fluctuations. However, the interpretation of monitored data is not straightforward. Long-term datasets often contain spikes, offsets, resets, flatline behaviour, missing data, and other anomalies that may mask or distort the true physical response of the system. Therefore, meaningful interpretation cannot rely on raw data alone, but requires a rigorous framework that combines site characterization, laboratory evidence, quality control, and physically based analysis.

Within this context, the present thesis focuses on the monitored levee section at **San Giorgio principal station (GP)**, located along the right-bank levee system of the Tagliamento River in northeastern Italy. The Tagliamento is a dynamic gravel-bed river characterized by active geomorphological processes, a wide floodplain corridor, and significant hydrologic variability. The San Giorgio site provides a valuable case study because it combines a monitored embankment section with available site investigations, including borehole SA1, CPT soundings, laboratory soil characterization, and long-term monitoring records of tension and water content. This combination makes it possible to investigate the hydro-mechanical response of the embankment in a site-specific and integrated way.

The motivation for this thesis lies in the need to move from raw monitoring observations toward a defensible engineering interpretation of embankment behaviour. In particular, the study addresses how tension and humidity measurements evolve over time and depth, how these responses relate to rainfall and hydrometric forcing, how stratigraphic variability influences the observed behaviour, and how sensor reliability affects the interpretation of seasonal trends and field-derived retention relationships. In this sense, the thesis is not only an analysis of monitoring results, but also an attempt to establish a structured methodology for extracting reliable information from imperfect field data.

1.2 Problem statement

The hydro-mechanical behaviour of levees is governed by complex interactions among soil properties, hydraulic boundary conditions, climatic forcing, and internal stratigraphic variability. In unsaturated conditions, these interactions become even more difficult to interpret because changes in suction and water content may be influenced simultaneously by infiltration, evapotranspiration, water-level fluctuations, permeability contrasts, and delayed response with depth. Although field monitoring provides direct access to these processes, the recorded signals do not automatically translate into reliable physical interpretation. Instead, the data must first be examined critically to distinguish real soil behaviour from instrumental artefacts and inconsistencies.

A further challenge is that embankment materials are rarely homogeneous. At the San Giorgio site, the monitored levee section is associated with a man-made embankment body overlying natural fluvial/alluvial deposits, with sandy to silty-sandy materials, local finer interlayers, and coarser deposits at depth. Such a setting naturally leads to both vertical and lateral variability in hydraulic response. Therefore, differences observed among sensors may reflect not only depth, but also location within the cross section, local material contrasts, and the connectivity of hydraulic pathways. Without a site-specific stratigraphic framework and supporting laboratory information, the interpretation of the monitoring response would remain incomplete.

The core problem addressed by this thesis is therefore the following: **how can long-term monitoring data from a levee be transformed into a reliable interpretation of hydro-mechanical behaviour when the dataset is affected by variable sensor quality, local stratigraphic heterogeneity, and transient environmental forcing?** To answer this question, the thesis adopts an integrated workflow in which literature-based concepts, site characterization, laboratory evidence, data-quality assessment, seasonal analysis, and field-derived water-retention interpretation are brought together within a single case study.

1.3 Aim of the thesis

The main aim of this thesis is to investigate the hydro-mechanical response of the San Giorgio principal levee section through an integrated interpretation of field monitoring data, local stratigraphic characterization, laboratory soil properties, and data-quality assessment, with particular attention to unsaturated conditions and their seasonal evolution under environmental forcing.

More specifically, the thesis seeks to understand how suction/tension and water content vary in time and with depth within the monitored embankment, how these variations relate to rainfall and river-stage conditions, and to what extent reliable water-retention behaviour can be inferred from the field records after suitable cleaning and validation procedures. At the same time, the work aims to demonstrate that rigorous quality control is an essential prerequisite for any physically meaningful interpretation of long-term monitoring datasets.

1.4 Specific objectives

To achieve the overall aim, the thesis is organized around the following specific objectives:

1. To review the main theoretical concepts and research developments related to embankment behaviour under transient hydraulic and climatic conditions, with particular emphasis on unsaturated soil mechanics, suction, water-retention behaviour, monitoring interpretation, and the role of environmental forcing.

2. To describe the study area and monitoring framework, with a specific focus on the San Giorgio principal station, and to establish a site-specific stratigraphic model by integrating borehole data, CPT soundings, levee geometry, and supporting laboratory evidence.

3. To characterize the soils of the study area through laboratory investigations, including grain-size distribution, hydrometer analysis, Atterberg limits where applicable, and soil classification, in order to provide the material basis for interpreting field response. This objective also includes the use of predictive hydraulic interpretation to place the monitored behaviour within a broader soil-water retention framework. This objective is consistent with the later thesis chapters built on laboratory interpretation and supporting evidence for the stratigraphic framework.

4. To develop and apply a systematic quality-control procedure for the monitoring dataset, capable of identifying anomalies such as spikes, resets, flatline behaviour, discontinuities, and unrealistic values, and of distinguishing reliable, partially reliable, and unreliable sensor records before further interpretation. The monitoring chapters explicitly frame the subsequent analysis around validated measurements only.

5. To analyse the temporal and seasonal behaviour of tension and humidity measurements at the San Giorgio principal station, and to relate the observed trends to rainfall, hydrometric fluctuations, sensor depth, and spatial position within the monitored levee section. The monitoring network at GP was designed specifically to investigate both vertical variability with depth and lateral variability across the cross section.

6. To explore representative field-derived water-retention relationships from paired tension and humidity observations, and to assess how data cleaning and quality control influence the physical consistency of these relationships within the monitored field environment. This objective follows directly from the thesis framework linking unsaturated-soil concepts, monitoring interpretation, and WRC-based analysis.

1.5 Scope of the work

This thesis is focused specifically on the **San Giorgio principal monitoring station (GP)** within the broader Tagliamento levee monitoring system. Although the overall monitoring network includes several stations in both the San Giorgio and Bevazzana sectors, the present work restricts the detailed interpretation to the principal GP section in order to develop a coherent and sufficiently detailed case study. This focus allows direct integration of monitoring observations with local site investigations, updated levee geometry, and supporting laboratory data.

The scope of the work includes:

- the literature framework required to interpret embankment behaviour under transient hydraulic and climatic conditions.
- the site description and stratigraphic reconstruction of the San Giorgio principal section.
- the laboratory characterization of representative soils from the study area.
- the cleaning, validation, and classification of long-term monitoring data.
- the seasonal interpretation of tension and humidity records in relation to external forcing.
- and the analysis of representative field-derived retention behaviour.

At the same time, some aspects are intentionally outside the scope of the thesis. The work does not attempt a full comparison among all monitoring stations of the Tagliamento system, nor does it develop a complete numerical seepage or stability model calibrated against the monitoring data. The thesis instead prioritizes the development of a robust interpretative framework based on monitored observations, stratigraphic evidence, and laboratory support. This delimitation is necessary in order to keep the study focused and methodologically consistent. The chapter descriptions in the draft consistently position later chapters around characterization, quality control, and temporal interpretation rather than full predictive modelling.

1.6 Methodological overview

The methodological structure of the thesis follows a progressive workflow from theory to interpretation. First, the relevant literature on unsaturated soil behaviour, levee hydraulics, monitoring, and water-retention concepts is reviewed to define the theoretical background of the study. This step establishes the importance of suction, hydraulic forcing, seasonal variability, and monitoring-data reliability in the analysis of embankment response.

Second, the study area and monitoring network are described, with particular attention to the San Giorgio principal station. The site-specific stratigraphic framework is then reconstructed using borehole SA1, CPTG1, CPTE1, the updated levee geometry, and supporting laboratory information. This provides the physical basis needed for interpreting lateral and vertical variability in the monitoring records.

Third, laboratory investigations are used to characterize the soils of the study area and support the interpretation of the monitored response. Grain-size distribution, hydrometer results, plasticity where applicable, and classification information help define the material context in which suction and humidity variations occur. These data are then used as supporting evidence for both stratigraphic interpretation and hydraulic understanding. The Chapter 3 dataset description explicitly states that laboratory classification results are used as supporting evidence, with detailed presentation deferred to Chapter 4.

Fourth, the monitoring dataset is subjected to a quality-control procedure aimed at identifying anomalous behaviour, preserving the time structure of the series, and defining which data can be considered reliable for interpretation. This step is essential because the monitoring records include artefacts that would otherwise bias temporal analysis, statistical summaries, and field-derived retention relationships. The literature review already highlights these issues as a major challenge in long-term monitoring interpretation.

Finally, the validated monitoring data are analysed to investigate seasonal behaviour, depth-dependent response, and forcing-response relationships with rainfall and hydrometric conditions. Representative paired tension–humidity datasets are then used to explore empirical water-retention behaviour under field conditions. Through this sequence, the thesis develops an integrated framework for moving from raw observations to site-specific hydro-mechanical interpretation.

1.7 Structure of the thesis

The thesis is organized into eight chapters.

Chapter 2 presents the literature review. It discusses the main concepts related to river embankment behaviour under transient hydraulic and climatic forcing, with particular emphasis on unsaturated soil mechanics, suction, the Soil–Water Retention Curve, monitoring interpretation, and the geomorphological context of the Tagliamento River. This chapter establishes the theoretical and methodological foundation for the study.

Chapter 3 describes the study area, the monitoring system, and the stratigraphic framework, focusing on the San Giorgio principal station. It introduces the site context, summarizes the available datasets, and develops the stratigraphic interpretation that supports the later analysis of monitoring data.

Chapter 4 presents the laboratory characterization of the soils and the supporting hydraulic interpretation used to frame the field behaviour within a material-based context. As already indicated in Chapter 3, laboratory classification results provide supporting evidence for the interpretation of the monitored section.

Chapter 5 explains the monitoring-data methodology, including preparation, cleaning, and the treatment of anomalous values. This chapter establishes the workflow used to transform raw time-series data into validated datasets suitable for analysis, as anticipated by the literature review.

Chapter 6 evaluates sensor performance and reliability. It classifies the monitoring records according to their quality and identifies the main limitations affecting individual sensors or intervals. This chapter provides the basis for deciding which monitored data can be interpreted with confidence. This role follows directly from the QC and long-term monitoring challenges highlighted earlier in the thesis.

Chapter 7 presents the seasonal interpretation of validated tension and humidity records, relating them to rainfall, hydrometric forcing, depth, and spatial position within the levee section. It also includes the discussion of representative field-derived water-retention behaviour based on paired monitoring observations. This chapter corresponds to the final analytical stage anticipated by the literature framework and site/monitoring descriptions.

Chapter 8 summarizes the main findings of the thesis, highlights the key contributions and limitations of the work, and provides recommendations for future research and monitoring-based levee assessment. This closing role is consistent with the overall structure established across the completed draft.

1.8 Final introductory remarks

The present thesis is positioned at the intersection of unsaturated soil mechanics, field monitoring, and site-specific embankment interpretation. By focusing on the San Giorgio principal station, it seeks to show how hydro-mechanical understanding can be strengthened when theoretical concepts, local stratigraphy, laboratory characterization, and validated field measurements are considered together rather than separately. In this sense, the work aims not only to interpret a specific monitoring dataset, but also to demonstrate a practical framework for extracting meaningful engineering information from complex long-term records.

Chapter 2 Literature Review

2.1 Introduction

River embankments (levees) represent one of the most widely adopted structural measures for flood protection in fluvial environments. Their primary function is to confine river flow within a defined channel and prevent inundation of adjacent floodplains and inhabited areas. However, despite their widespread use, levees are inherently vulnerable structures, whose performance is governed by complex interactions between hydraulic loading, soil properties, and environmental conditions. In recent decades, numerous studies have highlighted that failures of river embankments are often associated with transient processes such as rapid river level fluctuations, prolonged high-water conditions, and rainfall infiltration, rather than purely static loading conditions (Gragnano et al., 2021).

Traditionally, the analysis and design of levees have been carried out under simplified assumptions, often neglecting the role of unsaturated soil mechanics and focusing primarily on saturated conditions. However, it is now well recognized that a significant portion of the embankment body remains in an unsaturated state under normal conditions, where matric suction contributes to the effective stress and shear strength of the soil. Variations in suction and water content, driven by hydraulic and climatic forcing, can therefore significantly influence the stability of levees over time (Rocchi et al., 2020). As a result, understanding the coupled behavior of hydraulic and geotechnical processes within partially saturated soils has become a key aspect of modern levee analysis.

In this context, the Soil-Water Retention Curve (WRC) plays a fundamental role, as it describes the relationship between suction and water content and governs both the hydraulic conductivity and mechanical behavior of unsaturated soils. Accurate characterization of the WRC is essential for modeling transient seepage processes and evaluating the impact of suction on shear strength. However, direct experimental determination of WRC is often time-consuming and resource-intensive, which has led to the development of predictive models based on basic geotechnical properties, such as the approach proposed by (Aubertin et al., 2003). These models provide practical alternatives for estimating WRC in the absence of detailed laboratory measurements.

In parallel with advances in theoretical and numerical modeling, significant progress has been made in the field of geotechnical monitoring. The implementation of in-situ monitoring systems, including sensors for measuring suction, water content, and pore-water pressure, has enabled the continuous observation of levee behavior under real environmental conditions. Such monitoring systems provide valuable data for understanding spatial and temporal variations within the embankment and for validating numerical models (Rocchi et al., 2020). Furthermore, the integration of field monitoring data with laboratory characterization and numerical simulations has been identified as a powerful approach for improving the reliability of levee stability assessments (Gragnano et al., 2021).

In addition to geotechnical and hydraulic considerations, the geomorphological context of river systems also plays a crucial role in influencing flood risk and levee performance. The Tagliamento River, located in northeastern Italy, represents a highly dynamic fluvial system characterized by braided morphology, significant sediment transport, and historical channel migration. Studies on the historical evolution of the Tagliamento River have demonstrated that flood-prone areas are often associated with former river channels and floodplain corridors, and that human interventions such as dike construction have significantly altered the natural behavior of the river, increasing flood risk in certain reaches (Spaliviero, 2003).

Based on these considerations, this chapter aims to provide a comprehensive review of the key concepts and methodologies relevant to the analysis of river embankments under transient conditions. The review focuses on unsaturated soil mechanics, soil-water retention behavior, field monitoring techniques, and integrated modeling approaches, with particular emphasis on their application to levee systems. The insights gained from the reviewed literature form the theoretical foundation for the analyses presented in the subsequent chapters, including the interpretation of monitoring data and the estimation of hydraulic and mechanical soil properties at the San Giorgio principal station.

2.2 River Embankments and Flood Risk

River embankments (levees) are engineered earth structures designed to protect floodplains and urban areas from river inundation by confining water within the channel. While they play a crucial role in flood risk mitigation, levees are complex systems whose behavior depends on the interaction between hydraulic loading, soil properties, and structural configuration. Unlike rigid hydraulic structures, embankments are typically composed of natural or compacted soils, often exhibiting significant spatial variability in material properties due to construction methods, aging, and historical modifications (Cola, n.d.).

The structural integrity of levees is influenced by both external and internal processes. External processes include river flow, overtopping, and surface erosion, while internal processes are primarily related to seepage and pore-water pressure evolution within the embankment body. Among these, seepage-induced mechanisms are considered one of the most critical factors affecting levee performance, as they directly influence effective stress and soil strength. Under transient hydraulic conditions, such as rapid river level rise or prolonged high-water stages, seepage gradients may increase significantly, leading to internal instability (Gragnano et al., 2021).

Levee failures are commonly classified into three main categories: external erosion, internal erosion, and slope instability. External erosion occurs when flowing water removes material from the surface of the embankment, typically during overtopping events. Internal erosion, on the other hand, develops within the soil mass and includes processes such as piping, suffusion, and contact erosion. These mechanisms are often triggered by seepage forces and can lead to progressive material removal and eventual structural collapse. Slope instability may occur when the shear strength of the soil is insufficient to resist driving forces, which can be exacerbated by increased pore-water pressure or reduction in suction during wet conditions (Cola, n.d.).

A key aspect of levee behavior is the inherent heterogeneity of the embankment structure. Many levees have been constructed or modified over long periods, resulting in layered configurations with varying grain size distributions, permeability, and mechanical properties. Interfaces between different soil layers or between original and repaired sections can act as preferential pathways for seepage, increasing the risk of internal erosion. Additionally, localized features such as animal burrows, cracks, or poorly compacted zones may further weaken the structure and promote the development of failure mechanisms (Cola, n.d.).

The response of levees to hydraulic loading is strongly influenced by transient conditions. Unlike steady-state analyses, which assume constant hydraulic gradients, real levee systems are subjected to time-dependent boundary conditions driven by river stage fluctuations and climatic inputs. These transient processes result in delayed and non-uniform changes in pore-water pressure within the embankment. For instance, rapid river level rise may not immediately affect deeper layers, whereas prolonged high-water conditions can gradually increase saturation and reduce suction, leading to a progressive decrease in soil strength (Gragnano et al., 2021).

In addition to hydraulic factors, flood risk associated with levees is also affected by geomorphological and environmental conditions. River systems such as the Tagliamento exhibit dynamic behavior characterized by channel migration, sediment transport, and evolving floodplain morphology. Historical analyses have shown that flood-prone areas often coincide with former river channels and zones of repeated inundation. The confinement of rivers through levee construction has altered natural flow patterns, often increasing flow velocities and concentrating hydraulic loads in specific reaches, thereby enhancing the potential for failure (Spaliviero, 2003).

Modern flood risk management recognizes that levees should not be considered as isolated structures but rather as components of a broader river system. Their performance depends not only on their design and material properties but also on the surrounding hydrological and geomorphological context. Consequently, effective assessment of levee safety requires an integrated understanding of hydraulic loading, soil behavior, and environmental conditions, particularly under transient scenarios where traditional assumptions may no longer be valid (Cola, n.d.).

2.3 Unsaturated Soil Mechanics in Embankments

The behavior of river embankments is strongly influenced by the hydraulic state of the soil, which is typically unsaturated under normal operating conditions. In unsaturated soils, the pore space is occupied by both water and air, leading to the development of matric suction, defined as the difference between pore air pressure and pore water pressure. This parameter plays a fundamental role in controlling both the hydraulic and mechanical behavior of soils and must be considered in the analysis of levee stability (Rocchi et al., 2020).

In contrast to saturated conditions, where effective stress depends solely on pore-water pressure, unsaturated soils exhibit an additional contribution to shear strength due to suction. This contribution is often referred to as apparent cohesion, which increases the overall resistance of the soil to deformation and failure. As a result, levees in unsaturated conditions may exhibit higher stability than predicted by classical saturated soil mechanics approaches. However, this additional strength is highly variable and can decrease rapidly when suction is reduced due to infiltration or rising water levels (Gragnano et al., 2021).

The relationship between suction and shear strength is commonly described using extended effective stress frameworks for unsaturated soils. These formulations account for the influence of suction on interparticle forces and highlight the importance of degree of saturation in controlling soil behavior. As suction decreases, the degree of saturation increases, leading to a reduction in effective stress and shear strength. This process is particularly critical during flood events or prolonged rainfall, when infiltration leads to progressive wetting of the embankment body (Gragnano et al., 2021).

In river embankments, the distribution of suction is neither uniform nor constant. Instead, it varies spatially and temporally in response to environmental conditions. Shallow layers are typically influenced by atmospheric processes such as rainfall, evaporation, and temperature fluctuations, resulting in rapid and cyclic changes in suction. In contrast, deeper layers are less affected by surface conditions and respond primarily to changes in river water level, often exhibiting delayed responses due to low permeability and longer drainage paths (Rocchi et al., 2020).

The transient nature of suction in levees is a key factor in understanding their stability. During periods of low river level and dry conditions, high suction values may develop, increasing soil strength and contributing to embankment stability. However, during flood events or sustained wet periods, suction is progressively reduced as water infiltrates the soil and raises pore-water pressure. This reduction in suction can significantly weaken the soil, particularly if it occurs over extended periods, leading to critical conditions that may not coincide with the peak river level (Gragnano et al., 2021).

An additional complexity in unsaturated soil behavior is the presence of hysteresis in the relationship between suction and water content. The hydraulic path followed during wetting differs from that during drying, resulting in different suction values for the same water content depending on the history of the soil. This phenomenon is particularly relevant in levees, where repeated wetting and drying cycles occur due to seasonal variations and fluctuating hydraulic conditions. As a result, accurate modeling of levee behavior requires consideration of both the current hydraulic state and the preceding hydrological history (Rocchi et al., 2020).

The importance of unsaturated soil mechanics in levee analysis has led to increased use of field monitoring systems capable of measuring suction and water content in situ. These measurements provide valuable insights into the temporal evolution of the hydraulic state within the embankment and enable more realistic assessment of stability under transient conditions. By integrating suction measurements with numerical modeling and laboratory data, it is possible to capture the complex interactions governing levee behavior and improve the reliability of engineering predictions (Gragnano et al., 2021).

Overall, the inclusion of unsaturated soil mechanics represents a significant advancement in the understanding of embankment performance. It allows for a more accurate representation of real conditions, particularly under transient hydraulic and climatic forcing, and provides a framework for linking field observations with theoretical and numerical analyses.

2.4 Soil-Water Retention Curve (WRC)

The Soil–Water Retention Curve (WRC), also referred to as the Soil–Water Characteristic Curve (SWCC), describes the relationship between soil suction and water content (or degree of saturation). It is one of the fundamental constitutive relationships in unsaturated soil mechanics, as it governs both the hydraulic and mechanical behavior of partially saturated soils. In the context of river embankments, the WRC plays a crucial role in understanding how water is retained within the soil and how suction evolves under changing environmental conditions (Rocchi et al., 2020).

Physically, the WRC reflects the distribution of pore sizes within the soil. Larger pores drain at low suction values, while smaller pores retain water at higher suction levels. As suction increases, water progressively drains from the soil, leading to a decrease in water content. This process is not linear and typically exhibits a characteristic S-shaped curve when plotted on a semi-logarithmic scale. The shape of the WRC is strongly influenced by soil type, grain size distribution, and porosity, with coarse-grained soils exhibiting steep curves and fine-grained soils showing more gradual transitions (Gragnano et al., 2021).

The WRC is essential for determining several key hydraulic properties, including unsaturated hydraulic conductivity and degree of saturation. These parameters are required for modeling transient seepage processes within levees, particularly under conditions of fluctuating river levels and variable climatic inputs. Moreover, the WRC is directly linked to the contribution of suction to shear strength, making it a critical component in stability analyses of embankments (Gragnano et al., 2021).

In practical applications, the WRC can be obtained through laboratory testing using techniques such as pressure plate apparatus, tensiometers, or filter paper methods. However, these tests are often time-consuming, require specialized equipment, and may not be feasible for large numbers of samples. As a result, alternative approaches based on field measurements or predictive models are frequently adopted, especially in large-scale studies or monitoring-based investigations (Aubertin et al., 2003).

Field monitoring provides an additional means of deriving WRC relationships by combining simultaneous measurements of suction and water content. This approach allows for the estimation of so-called “field WRC,” which reflects in-situ conditions and accounts for natural variability, soil structure, and environmental influences. Studies have shown that field-derived WRC may differ from laboratory results due to factors such as hysteresis, soil fabric, and boundary conditions, highlighting the importance of considering both approaches in engineering analyses (Rocchi et al., 2020).

A key feature of the WRC is the presence of hysteresis, which refers to the difference between drying and wetting paths. During drying, water is removed from the largest pores first, while during wetting, air may remain trapped within the pore space, leading to different water content values for the same suction. This phenomenon is particularly relevant in levees, where soils are subjected to repeated cycles of wetting and drying due to seasonal changes, rainfall, and river level fluctuations. Ignoring hysteresis may lead to inaccuracies in modeling and interpretation of soil behavior (Gragnano et al., 2021).

In addition to its physical interpretation, the WRC is widely used as an input function in numerical models for simulating unsaturated flow. Mathematical representations of the WRC enable the incorporation of suction-dependent hydraulic properties into transient seepage analyses. These models allow for the simulation of complex processes such as infiltration, evaporation, and pore-pressure evolution within the embankment, providing a more realistic representation of levee behavior under varying boundary conditions (Gragnano et al., 2021).

Overall, the Soil–Water Retention Curve represents a key link between hydraulic and mechanical processes in unsaturated soils. Its accurate characterization is essential for understanding the response of river embankments to environmental and hydraulic forcing, and for developing reliable models for predicting their performance under transient conditions.

2.5 WRC Models and Prediction Methods

The Soil–Water Retention Curve (WRC) is commonly represented using mathematical models that describe the relationship between suction and water content through a set of fitting or predictive parameters. These models are essential for incorporating unsaturated soil behavior into numerical analyses, as they allow continuous and differentiable representation of hydraulic properties. Among the various formulations proposed in the literature, the van Genuchten model and the semi-empirical model by (Aubertin et al., 2003) are widely used due to their flexibility and applicability to a range of soil types.

The van Genuchten model is one of the most extensively adopted formulations for describing the WRC. It expresses the relationship between suction and degree of saturation using a set of parameters that are typically obtained by fitting the model to experimental data. The model provides a smooth and continuous curve capable of accurately representing the characteristic S-shape of the WRC. Its parameters are directly related to soil properties, such as pore size distribution and air-entry value, making it suitable for both laboratory and field data interpretation (Gragnano et al., 2021).

One of the main advantages of the van Genuchten model is its compatibility with numerical seepage analyses. It is commonly implemented in geotechnical software to simulate unsaturated flow and transient hydraulic processes within soil structures. However, the model requires reliable experimental data for calibration, which may not always be available, particularly in large-scale field studies or in cases where laboratory testing is limited. In such situations, alternative predictive approaches are needed to estimate the WRC without direct measurements.

To address this limitation, (Aubertin et al., 2003)proposed a semi-empirical model that predicts the WRC based on basic geotechnical properties, such as grain size distribution, porosity, and void ratio. The model is based on the concept that pore size distribution governs the retention of water within the soil, with smaller pores retaining water at higher suction values. By linking measurable soil properties to hydraulic behavior, this approach provides a practical method for estimating the WRC when experimental data are unavailable or insufficient.

The Aubertin model offers several advantages, particularly in preliminary analyses and large-scale applications. It allows for rapid estimation of WRC using commonly available laboratory data, reducing the need for specialized testing. This makes it especially useful in studies where multiple soil layers must be characterized or where field conditions limit the feasibility of detailed laboratory investigations. However, as a predictive model, it relies on simplifying assumptions and may not fully capture site-specific factors such as soil structure, hysteresis, or environmental variability (Aubertin et al., 2003).

A comparison between the van Genuchten and Aubertin approaches highlights the trade-off between accuracy and practicality. The van Genuchten model provides high accuracy when calibrated with experimental data, making it suitable for detailed analyses and numerical modeling. In contrast, the Aubertin model offers greater flexibility and ease of application, particularly when only basic soil properties are available. In practice, the choice between these models depends on data availability, required level of accuracy, and the objectives of the analysis.

Recent studies have demonstrated the benefits of combining both approaches, where predictive models are used to generate initial estimates of the WRC, which are then refined using field or laboratory data. This hybrid strategy allows for efficient characterization of soil hydraulic behavior while maintaining a reasonable level of accuracy. In the context of river embankments, such approaches are particularly valuable, as they enable the integration of laboratory characterization, field monitoring, and numerical modeling within a unified framework (Gragnano et al., 2021)

Overall, the use of WRC models represents a fundamental component of modern geotechnical analysis. By providing a mathematical link between suction and water content, these models enable the simulation of unsaturated flow and the assessment of soil behavior under transient conditions. Their application is essential for understanding and predicting the performance of river embankments subjected to varying hydraulic and climatic forcing.

2.6 Field Monitoring of River Embankments

Field monitoring has become an essential component in the assessment of river embankment performance, as it provides direct insight into the in-situ hydraulic and mechanical behavior of soils under real environmental conditions. Unlike laboratory testing or purely numerical approaches, monitoring systems allow continuous observation of the temporal and spatial evolution of key variables such as water content, suction, pore-water pressure, and temperature. These measurements are particularly important for understanding transient processes in levees, which are governed by variable hydraulic loading and climatic influences (Rocchi et al., 2020).

Modern geotechnical monitoring systems typically consist of networks of sensors installed at different depths and locations within the embankment. Commonly used instruments include dielectric probes for measuring volumetric water content, tensiometers for direct measurement of suction such Tensiometer, and indirect suction sensors such as MPS-type devices. The combination of multiple sensor types enables a more comprehensive characterization of the soil state, as each sensor provides complementary information about hydraulic conditions (Rocchi et al., 2020).

The spatial distribution of sensors plays a critical role in capturing the heterogeneity of embankments. Sensors are often installed along vertical profiles to investigate depth-dependent behavior, as well as along horizontal alignments to assess lateral variability. Studies have shown that shallow zones typically exhibit rapid and pronounced changes in water content and suction due to atmospheric effects, while deeper zones respond more slowly and are primarily influenced by river level fluctuations. This layered response highlights the importance of multi-depth monitoring for accurate interpretation of levee behavior (Gragnano et al., 2021).

One of the main challenges associated with field monitoring is the reliability and accuracy of sensor measurements. Different sensor types may exhibit varying levels of precision, sensitivity, and susceptibility to environmental disturbances. For example, dielectric sensors used for water content measurement often require site-specific calibration to account for soil type and salinity effects. Similarly, indirect suction sensors may provide less accurate readings at low suction ranges compared to tensiometers, which are generally considered more reliable within their operational limits (Rocchi et al., 2020).

Sensor calibration is therefore a critical step in ensuring data quality. Calibration procedures typically involve laboratory testing under controlled conditions, where sensor readings are compared with reference measurements. In addition, field validation may be required to account for installation effects and long-term drift. Without proper calibration, monitoring data may contain systematic errors that can lead to incorrect interpretation of soil behavior (Rocchi et al., 2020).

Another important aspect of monitoring systems is data interpretation and quality control. Field data are often affected by anomalies such as spikes, signal drift, sensor malfunction, or abrupt shifts due to environmental or technical factors. Identifying and filtering such anomalies is essential for extracting meaningful information from the dataset. Recent studies emphasize the need for systematic quality control procedures to distinguish between real physical responses and measurement errors, particularly in long-term monitoring programs (Gragnano et al., 2021).

Field monitoring also enables the development of relationships between measured variables, such as suction and water content, which can be used to derive in-situ Soil–Water Retention Curves (WRC). This approach provides valuable information about soil behavior under natural conditions and allows comparison with laboratory-derived relationships. However, field-derived WRC may exhibit greater variability due to environmental influences, soil heterogeneity, and hysteresis effects, which must be considered in interpretation (Rocchi et al., 2020).

The integration of monitoring data with external forcing factors, such as rainfall and river water level, further enhances the understanding of levee behavior. By analyzing correlations between these variables, it is possible to identify the dominant drivers of hydraulic response and assess the timing and magnitude of soil reactions to external events. Such analyses are essential for evaluating the performance of embankments under real loading conditions and for identifying critical scenarios that may lead to instability.

Overall, field monitoring represents a powerful tool for bridging the gap between theoretical models and real-world behavior. It provides the empirical basis for validating numerical simulations, improving parameter estimation, and enhancing the reliability of stability assessments. In the context of river embankments, long-term monitoring is particularly valuable for capturing seasonal variations and extreme events, which are key factors in the evaluation of flood risk and structural performance.

2.7 Integrated Monitoring and Numerical Modeling

In recent years, the assessment of river embankment performance has increasingly benefited from the combined use of field monitoring, laboratory characterization, and numerical modeling. In the literature, this integrated approach is considered particularly valuable for studying transient hydraulic and climatic effects, because it allows researchers to compare observed field behaviour with simulated responses and to refine the interpretation of seepage and stability processes. While each method can provide useful information on its own, their combined use can improve the overall understanding of levee behaviour under complex environmental conditions (Gragnano et al., 2021).

Numerical modeling is widely used to simulate the hydraulic and mechanical response of embankments. In particular, transient seepage analyses are commonly adopted to represent the movement of water through partially saturated soils under changing boundary conditions such as rainfall and river-stage fluctuations. These models generally require hydraulic input parameters, including hydraulic conductivity functions and Soil–Water Retention Curves (WRC), which describe the relationship between suction and water content. When supported by reliable soil characterization and boundary-condition definition, such models can provide useful insight into the temporal evolution of pore-water conditions and degree of saturation within the embankment (Gragnano et al., 2021).

However, the reliability of numerical simulations depends strongly on the quality of the input information. In many practical cases, hydraulic parameters are estimated from laboratory tests, empirical correlations, or simplified assumptions, which may not fully represent field conditions. This is especially problematic in heterogeneous embankment systems, where local stratigraphic variability, environmental forcing, and non-uniform wetting and drying histories may lead to behaviour that is difficult to reproduce using generalized parameters alone. For this reason, several studies have emphasized the importance of field observations as a basis for improving the physical interpretation of embankment response (Rocchi et al., 2020).

Field monitoring provides time-dependent measurements of variables such as suction, water content, pore-water pressure, rainfall, and water level. These observations are highly valuable because they document the actual response of the embankment under real boundary conditions. In studies where numerical modeling is performed, such field measurements may be used for calibration, validation, or comparison with simulated results. In this way, monitoring can help constrain uncertain parameters and support a more realistic interpretation of transient processes (Gragnano et al., 2021).

At the same time, it is important to recognize that not all investigations need to perform numerical modeling directly in order to contribute meaningfully to the broader understanding of levee behaviour. A rigorous characterization of soil properties, monitoring-system performance, data reliability, and seasonal field response is itself a necessary step toward any future modeling effort. Before numerical simulation can be considered reliable, the physical meaning of the monitored signals and the quality of the available data must first be established with confidence.

For this reason, the present thesis does not develop or calibrate a numerical seepage or stability model. Instead, it focuses on the preliminary but essential stages that can support future reliable modeling: site-specific stratigraphic interpretation, laboratory-based soil characterization, quality control of monitoring data, and field-based analysis of tension and humidity response under environmental forcing. In this sense, the thesis should be viewed as providing the physical and interpretative basis upon which subsequent modeling work could be built, rather than as a modelling study in itself.

Therefore, within the context of the present work, the relevance of integrated monitoring and numerical modeling lies mainly in its value as a broader conceptual framework from the literature. The discussion in this section highlights why validated field observations, representative soil characterization, and careful interpretation of hydraulic response are indispensable prerequisites for future predictive analyses of embankment behaviour.

2.8 Influence of Hydraulic and Climatic Conditions

The behavior of river embankments is strongly controlled by external environmental forcing, primarily represented by hydraulic conditions (river water level fluctuations) and climatic factors such as rainfall, evaporation, and temperature. These factors govern the transient evolution of water content and suction within the embankment and play a critical role in determining its hydraulic response and mechanical stability over time (Rocchi et al., 2020).

River water level is one of the dominant drivers of embankment behavior. Variations in river stage induce changes in boundary conditions along the river-facing side of the levee, leading to the development of transient seepage within the soil mass. During periods of rising water level, hydraulic gradients increase, promoting infiltration into the embankment and reducing suction. Conversely, when the river level decreases, drainage processes occur, and suction may gradually recover. However, this response is not instantaneous, particularly in low-permeability soils, where delayed pore-pressure dissipation can result in lagged hydraulic behavior (Gragnano et al., 2021).

The influence of river level is typically more pronounced in deeper layers of the embankment, where the hydraulic response is governed by long-term and large-scale variations. In contrast, shallow layers are more sensitive to climatic conditions, especially rainfall and evaporation. Rainfall events contribute to infiltration at the surface, increasing water content and reducing suction, while evaporation and evapotranspiration processes lead to drying and an increase in suction. These processes often produce rapid and cyclic fluctuations in the upper portion of the embankment (Rocchi et al., 2020).

The combined effect of hydraulic and climatic forcing results in complex spatial and temporal patterns within the levee. Shallow zones tend to exhibit high variability and short response times, reflecting the influence of atmospheric conditions. Deeper zones, on the other hand, display smoother and delayed responses, controlled primarily by river water level changes. This depth-dependent behavior highlights the importance of considering both types of forcing in the interpretation of monitoring data and in the modeling of embankment performance (Gragnano et al., 2021).

An important aspect of environmental forcing is the time lag between external loading and internal response. For example, a rapid increase in river level may not immediately affect pore-water pressures at depth, due to the time required for seepage to propagate through the soil. Similarly, prolonged rainfall may lead to gradual wetting of the embankment, resulting in cumulative effects that are not evident from short-term observations. These delayed responses are critical for understanding the timing of potential instability, which may occur after the peak of a hydraulic event rather than during it (Gragnano et al., 2021).

Seasonal variations further contribute to the complexity of embankment behavior. During dry seasons, high suction values may develop due to evaporation, enhancing soil strength and stability. In contrast, wet seasons are characterized by reduced suction and increased water content, which may weaken the soil and increase the likelihood of failure. The repetition of wetting and drying cycles also contributes to hysteresis effects in the soil-water retention behavior, influencing the long-term evolution of hydraulic properties (Rocchi et al., 2020).

The interaction between river level fluctuations and climatic inputs can lead to particularly critical conditions. For instance, a flood event occurring after a period of heavy rainfall may result in an already saturated embankment, significantly reducing the available shear strength and increasing the risk of instability. Such combined scenarios highlight the importance of considering multiple forcing factors simultaneously in both monitoring and modeling studies (Gragnano et al., 2021).

The integration of environmental data, such as rainfall records and river stage measurements, with in-situ monitoring provides valuable insights into the governing processes within the embankment. By analyzing correlations between external forcing and internal responses, it is possible to identify dominant mechanisms and assess the sensitivity of the system to different types of loading. This approach is essential for improving predictive models and for developing effective flood risk management strategies.

Overall, hydraulic and climatic conditions represent key drivers of levee behavior, influencing both short-term responses and long-term performance. Their combined effects must be carefully considered in the analysis of embankments, particularly under transient conditions where traditional assumptions of steady-state behavior are no longer valid.

2.9 Geomorphological Context of the Tagliamento River

The Tagliamento River, located in northeastern Italy, is widely recognized as one of the most dynamic and morphologically complex fluvial systems in Europe. Its present configuration reflects a long history of geomorphological evolution, characterized by channel migration, intense sediment transport, floodplain reworking, and changes in planform along the river course. These characteristics make the Tagliamento an important case study for understanding the interaction between fluvial processes, flood risk, and embankment performance (Spaliviero, 2003).

The hydrological and geomorphological behavior of the Tagliamento is strongly influenced by its Alpine origin and by the large amount of sediment supplied from the upstream basin. In the upper and middle reaches, the river displays a braided morphology associated with high energy conditions, variable discharge, and active bedload transport. Downstream, the river progressively transitions toward a more confined and less laterally mobile pattern. This longitudinal variation in morphology is a key feature of the system and has important implications for flood propagation and sediment redistribution.

Historical analyses of the Tagliamento have shown that its floodplain has undergone repeated reorganization over time. Former channels, abandoned corridors, and zones of repeated inundation remain evident in the historical and geomorphological record, demonstrating that present flood-prone areas are often linked to earlier stages of river migration. This indicates that flood hazard cannot be understood solely from the current river position, but must also be interpreted in the context of long-term fluvial evolution (Spaliviero, 2003).

A particularly important aspect of the Tagliamento system is the transition from braided to more sinuous or meandering reaches in the lower plain. This transition is associated with a reduction in channel width and an increase in confinement, especially where anthropogenic structures such as dikes limit the natural mobility of the river. Such confinement alters the natural distribution of flow and sediment, often increasing hydraulic pressure on the embankment system and concentrating flood risk in downstream reaches.

Human intervention has played a significant role in modifying the natural dynamics of the Tagliamento River. The construction of levees and the confinement of the active channel have reduced the lateral space available for floodwaters and sediment deposition. While these measures were introduced to protect agricultural land and settlements, they have also altered the hydraulic behavior of the river, increasing the potential for concentrated flooding and changing the relationship between the river and its floodplain. As a result, modern flood risk in the Tagliamento basin is not only the product of natural geomorphological processes, but also of historical river engineering and land-use change (Spaliviero, 2003).

From a levee-analysis perspective, the geomorphological context of the Tagliamento is highly relevant because it provides the broader environmental framework within which the San Giorgio embankment system operates. The river's dynamic nature, combined with its history of channel migration and floodplain reoccupation, highlights the importance of considering both local geotechnical conditions and basin-scale fluvial processes when evaluating embankment behavior. This broader perspective is essential for interpreting monitoring data and understanding the significance of hydraulic forcing at the study site.

In addition, the Tagliamento context emphasizes that embankment safety should not be treated as an isolated geotechnical problem. Instead, levee performance must be viewed as part of a larger river–floodplain system, where hydraulic loading, sediment dynamics, channel confinement, and historical flood behavior all contribute to the current risk scenario. This systems-based understanding supports the need for integrated analysis approaches that combine local monitoring with geomorphological and hydraulic interpretation.

Overall, the Tagliamento River provides a particularly meaningful framework for this thesis, as it exemplifies the strong coupling between river dynamics and embankment performance. Its geomorphological history helps explain why flood risk remains spatially concentrated in certain zones and why levee assessment in this environment requires attention not only to soil behavior and seepage processes, but also to the broader evolution of the fluvial system.

2.10 Research Gaps and Motivation

Despite significant advances in the understanding of river embankment behaviour, several limitations remain in the current body of literature, particularly in relation to unsaturated soil response, long-term monitoring interpretation, and the characterization of field conditions under transient hydraulic and climatic forcing. While many studies have examined individual aspects of levee performance, such as seepage, soil classification, laboratory hydraulic characterization, or monitoring techniques, fewer contributions provide a sufficiently detailed field-based framework that links these elements in a consistent and site-specific way.

One of the main challenges identified in the literature concerns the characterization of unsaturated soil behaviour under real field conditions. Although the importance of suction and its contribution to shear strength are well established, the practical interpretation of suction-dependent behaviour in embankments remains difficult, especially where materials are heterogeneous and exposed to changing environmental forcing. In such cases, the hydraulic response is influenced not only by intrinsic soil properties, but also by stratigraphic variability, seasonal wetting–drying cycles, rainfall infiltration, and water-level fluctuations.

A second important gap concerns the determination and interpretation of the Soil–Water Retention Curve (WRC). Laboratory methods can provide detailed information on the relationship between suction and water content, but they are often time-consuming and may not fully represent in-situ conditions. As a result, many studies rely on predictive approaches or simplified assumptions. Although these approaches are useful, discrepancies often remain between predictive or laboratory-based WRC estimates and the behaviour observed in the field. This highlights the need for studies that critically compare different sources of hydraulic interpretation and clarify the limitations associated with each one.

Another major limitation in the literature relates to the use of long-term monitoring data. Field monitoring is widely recognized as one of the most effective tools for observing the real behaviour of embankments over time, but monitoring datasets frequently contain practical difficulties such as sensor drift, spikes, discontinuities, calibration uncertainty, missing data, or inconsistent records across depth and location. These issues can significantly affect interpretation if they are not addressed systematically. Consequently, there is a clear need for robust quality-control methodologies that can distinguish reliable signals from anomalous or misleading measurements before any physical conclusions are drawn.

In addition, although numerical modeling is often presented in the literature as a powerful tool for analysing transient seepage and embankment response, its reliability depends strongly on the quality of the supporting field and laboratory information. In many cases, the main limitation is not the availability of modelling tools themselves, but the uncertainty associated with the input parameters, boundary conditions, and interpretation of real monitoring data. This suggests that there is an important research need for studies that strengthen the field-based and interpretative foundation required before reliable predictive modeling can be attempted.

Another gap concerns the combined influence of hydraulic and climatic forcing on levee behaviour. While river-level fluctuations and rainfall are often studied separately, fewer works examine how their interaction shapes the time-dependent behaviour of embankment soils over seasonal timescales. Long-term datasets are especially valuable in this regard because they make it possible to identify delayed responses, repeated wetting–drying cycles, depth-dependent attenuation, and station-to-station variability. However, such datasets remain relatively limited, and when available, they are not always interpreted through a framework that combines data quality assessment, soil characterization, and environmental forcing.

In light of these gaps, the present thesis is motivated by the need to provide a rigorous field-based interpretation of the hydro-mechanical response of a monitored levee section under natural conditions. Rather than developing a numerical model directly, the thesis focuses on the steps that are necessary before such modelling can be considered reliable: characterization of the study area and local stratigraphy, laboratory interpretation of representative soils, quality control and classification of monitoring data, and analysis of the temporal behaviour of tension and humidity in relation to rainfall and hydrometric forcing.

The study focuses on the San Giorgio principal station along the Tagliamento River, where the available dataset includes site investigations, soil laboratory results, and long-term monitoring records. By integrating these elements, the thesis aims to improve the physical interpretation of field observations and to clarify how environmental forcing, soil heterogeneity, and sensor reliability affect the observed seasonal response of the embankment.

More specifically, the thesis contributes by: (i) evaluating the reliability and performance of monitoring sensors through systematic quality-control procedures, (ii) comparing representative water-retention relationships derived from field data and predictive approaches, and (iii) interpreting the temporal evolution of tension and humidity in relation to hydraulic and climatic forcing. In this sense, the work seeks to reduce the gap between theoretical understanding and real embankment behaviour, while also providing a sound basis for future modelling-oriented studies.

2.11 Chapter Summary

This chapter reviewed the main concepts and research developments relevant to the assessment of river embankments under transient hydraulic and climatic conditions. The literature showed that levee behaviour is governed by complex interactions among seepage processes, soil hydraulic properties, mechanical response, and external forcing such as river water-level fluctuations and rainfall. In this context, the role of unsaturated soil mechanics is particularly important, since suction contributes significantly to soil strength and influences the stability and hydraulic response of embankments over time (Gragnano et al., 2021; Rocchi et al., 2020).

Particular attention was given to the Soil–Water Retention Curve (WRC), which represents a key link between suction and water content and forms the basis for the characterization of unsaturated soil behaviour. Both experimental and predictive approaches were discussed, including the use of mathematical formulations such as the van Genuchten model and semi-empirical prediction methods such as the approach proposed by Aubertin et al. (2003). The reviewed literature highlighted the importance of accurate WRC characterization for seepage analysis, interpretation of monitoring data, and understanding of soil response under variable environmental conditions (Aubertin et al., 2003).

The chapter also emphasized the growing importance of field monitoring in levee studies. Modern sensor systems provide valuable time-series measurements of suction, water content, and pore-water pressure, allowing direct observation of embankment response under real conditions. However, the literature also pointed out the challenges associated with sensor calibration, data reliability, anomaly detection, and the interpretation of long-term datasets. These aspects confirm the need for systematic quality control and careful analysis of monitoring information before it is used for engineering interpretation (Rocchi et al., 2020).

In addition, the review showed that numerical modelling is an important tool within the broader field of levee assessment, particularly when supported by representative soil characterization and reliable field observations. At the same time, the reviewed studies made clear that the reliability of modelling results depends strongly on the quality of the input data, the definition of boundary conditions, and the physical interpretation of site behaviour under transient hydraulic and climatic forcing (Gragnano et al., 2021). For this reason, the present thesis does not directly perform numerical modelling, but instead focuses on the preliminary and essential steps that can support future modelling-oriented studies, namely site characterization, laboratory-based hydraulic interpretation, monitoring-data validation, and seasonal analysis of field response.

Finally, the geomorphological context of the Tagliamento River was discussed to place the present study within its broader environmental framework. The historical evolution of the river, its dynamic floodplain behaviour, and the influence of human-induced confinement highlight the importance of analysing embankments not as isolated structures, but as components of a larger river–floodplain system (Spaliviero, 2003). This perspective is particularly relevant for the San Giorgio site, where local embankment behaviour must be interpreted in relation to both hydraulic forcing and the geomorphological dynamics of the Tagliamento basin.

Overall, the reviewed literature provides the theoretical and methodological foundation for the subsequent chapters of this thesis. Building on these concepts, the following chapters focus on the characterization of the study area, laboratory interpretation of soil properties, quality control of monitoring data, and the analysis of the temporal and seasonal response of suction and water content at the San Giorgio principal station.

Chapter 3 Study Area, Monitoring Network, and Stratigraphic Framework (San Giorgio Principal)

This chapter presents the study area and monitoring network with a specific focus on the San Giorgio principal station (GP). It then develops the stratigraphic framework used in the thesis by combining the available site investigations (borehole SA1 and CPT soundings at CPTG1 and CPTE1) with the updated levee geometry. The resulting stratigraphic model provides the physical basis for the interpretation of monitoring data in the subsequent chapters

3.1 Study area and site context

The Tagliamento River is a large gravel-bed river system in northeastern Italy. The study area is located along the right-bank levee system near San Giorgio al Tagliamento. This levee protects the surrounding lowland area from river floods and is subject to seasonal hydrologic forcing through rainfall and river-stage fluctuations. In this thesis, the analysis is restricted to the San Giorgio principal monitoring station (GP), selected to represent the main monitored section for integrated interpretation of near-surface hydro-mechanical response.

In geomorphological terms, the Tagliamento is characterized by a wide active channel and a dynamic floodplain setting, with alternating bends and sediment bars typical of gravel-bed rivers. Short-term events (intense rainfall and flood pulses) and longer-term adjustments in sediment transport and channel morphology influence the local floodplain and the boundary conditions acting on the levee system. A detailed description of the Tagliamento River evolution and behavior is provided in Chapter 2.

The levee section investigated in this thesis is located in a lowland area close to the river corridor, where the ground surface is relatively flat outside the embankment and the local relief is mainly controlled by the levee body itself. The monitored cross section (San Giorgio principal station, GP) was selected because it represents the main reference section for the monitoring network and because it is supported by a concentrated set of site investigations, including borehole SA1 and nearby CPT soundings. These datasets allow the development of a site-specific stratigraphic framework that can be directly linked to the interpretation of the monitoring measurements.

Note on embankment materials. The San Giorgio levee is a man-made embankment; therefore, the shallow stratigraphy within the levee body reflects **construction fill** rather than purely natural sedimentation. While engineered levees are typically designed using selected borrow materials, historical river embankments were often constructed progressively over time using locally available sediments. In this thesis, the term *levee body* refers to this artificial fill, whereas deeper units are interpreted as **natural fluvial/alluvial deposits** forming the foundation.

From a geotechnical perspective, the site is expected to show granular to sandy–silty materials in the levee body and shallow foundation, with locally finer interlayers and progressively coarser fluvial deposits at depth. Such a context naturally leads to lateral variability across the levee section (e.g., differences between river-side and land-side positions) and vertical variability with depth. These stratigraphic features are particularly relevant for the hydro-mechanical response of unsaturated soils because they control permeability contrasts, water retention capacity, and the timing/magnitude of suction and moisture variations.

For these reasons, the study area provides an appropriate field-scale case study for investigating the relationships between environmental forcing (rainfall and river-stage fluctuations) and the observed sensor response at different locations and depths. The following sections describe the monitoring network and summarize the site investigations used to reconstruct the stratigraphic framework adopted in this thesis.

3.2 Overview of the monitoring system (six stations)

Figure 3.1 Regional and local location of the Tagliamento monitoring system.

To get a better sense of where the study is taking place, let's take a look at **Figure 3.1**. This figure gives us a clear idea of the geography of the area and helps us understand the location of the levee system along the Tagliamento River. The figure is shown in two different scales, so we can see the location from both a regional and a local perspective. If we look at the top part of the figure, we can see a wide view of the lower Tagliamento River corridor, which is in the Friuli-Venezia Giulia region. This view extends all the way to the coastal area and the Adriatic Sea. It's useful to see the bigger picture, as it shows us where the San Giorgio site is in relation to the rest of the river. We can see that the part of the river we're focusing on is in the lowland area, where the river is wider and the surrounding land is flat. This area is mostly used for farming and settlements. By looking at this figure, we can get a better understanding of the study area and how it fits into the larger geography of the region. The Tagliamento River plays a crucial role in the area, and understanding its course and surroundings is important for our study.

If we take a closer look at the area near the river, we can see exactly where the monitoring equipment is set up. This equipment is placed in two main areas: San Giorgio and Bevazzana. Each of these areas has a main monitoring station, and there are also smaller secondary stations nearby. We can see the layout of these stations on the map, which helps us understand how the whole monitoring system is organized. For this project, we're focusing on the San Giorgio main station, so the map is really useful for showing us where this station is in relation to the river and the surrounding area.

To make things clear and easy to understand, the picture has a few important details. It includes an arrow pointing north and a scale bar, which helps us figure out where things are and how far apart they are. The main goal of this picture is to show where our study area is and to help explain the rest of the chapter.

Hydrometric gauge (idrometer). The historical hydrometric station (idrometer) is located near the **San Giorgio South station (GS)**; GS is installed on the levee crest in correspondence with the lower part/base of the historical hydrometer, as reported in the installation documentation.

Piezometric/groundwater monitoring (piezometer). At the San Giorgio principal station (GP), piezometric conditions are monitored through the I1-B1 piezometer (level sensor installed inside the piezometric well near the levee toe on the river side). The level logger records pressure/head that can be used to track relative fluctuations of groundwater/pore-water conditions during hydrologic events. In the available dataset, the absolute values may be affected by a sensor zero-offset (shift of the reference level) and occasional anomalous spikes; therefore, the signal is mainly used to discuss **relative changes** rather than absolute piezometric head.

3.3 Monitoring network at San Giorgio: focus on the principal station (GP)

The San Giorgio site includes multiple instrumented sections; however, the thesis focuses only on the principal station (GP). The GP section is the reference cross section used for the analysis of suction/tension and moisture indicators in later chapters. The monitoring network is organized in sensor “groups” placed at different positions along the levee cross section and at multiple depths, so that both lateral variability across the embankment and vertical variability with depth can be investigated.

At the principal section, the monitoring system includes: (i) rainfall forcing (rain gauge), (ii) piezometric/water-level measurements in the near-river area (where available), and (iii) in-soil sensors (tensiometers and hygrometers) deployed at different depths. This configuration supports later analysis of seasonal dynamics and forcing-response relationships by linking subsurface conditions to external hydrologic drivers.

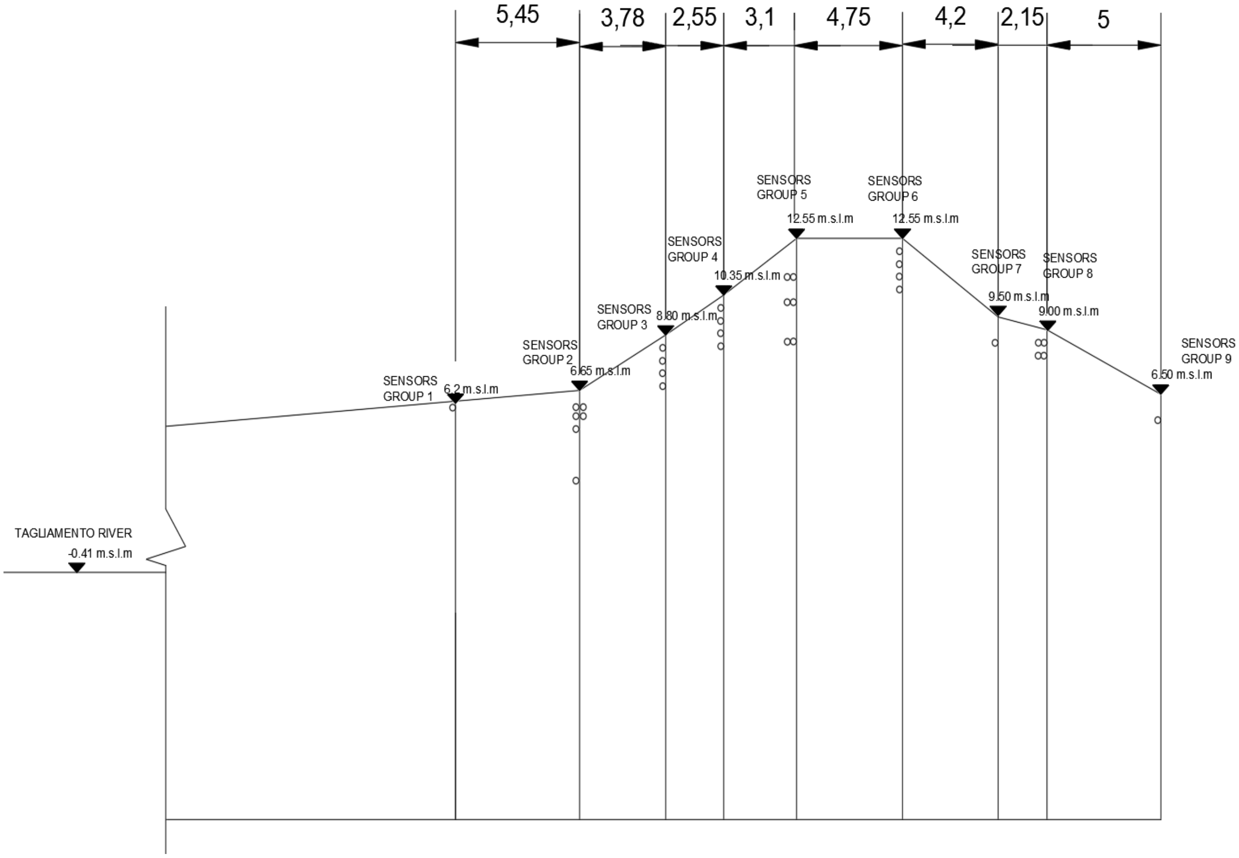

Figure 3.2 San Giorgio principal station (GP): monitored levee cross-section geometry and sensor-group layout.

“Circle markers indicate the nominal sensor installation depths (see Appendix 3.A for full sensor codes and depths).”

Schematic cross section of the GP levee showing the surveyed embankment profile and the horizontal spacing across the section. Vertical lines indicate the positions of sensor groups (Groups 1–9) installed at different locations along the levee to capture lateral variability in the monitored response.

3.4 Available site investigations and datasets used for Chapter 3

The stratigraphic interpretation of the San Giorgio principal section is based on a combination of historical information and targeted investigations conducted for the project. The key datasets used in this chapter are:

- Borehole SA1 (stratigraphic log and sampling) providing lithological descriptions and the deepest reference for coarse deposits.
- CPT soundings at CPTG1 and CPTE1 (cone penetration test profiles) providing continuous soil-behavior indicators with depth.
- Updated surveyed levee geometry for the GP cross section used as the base profile on which stratigraphic boundaries are plotted.
- Laboratory classification results (grain-size distribution and Atterberg limits) used as supporting evidence for the stratigraphic interpretation; detailed presentation is provided in Chapter 4.

Project documentation indicates that the levee body and shallow foundation at San Giorgio are dominated by sandy to sandy–silty materials, with local interbedded finer layers, while deeper deposits become coarser and may include gravelly horizons. This provides a reasonable conceptual expectation for lateral variability across the levee section, especially between river-side and land-side positions.

To clarify the spatial relationship between the monitoring network and the site investigations used for the stratigraphic interpretation, Figure 3.3 presents both a detailed map of the principal monitored area and an overview of the three San Giorgio monitoring sections.

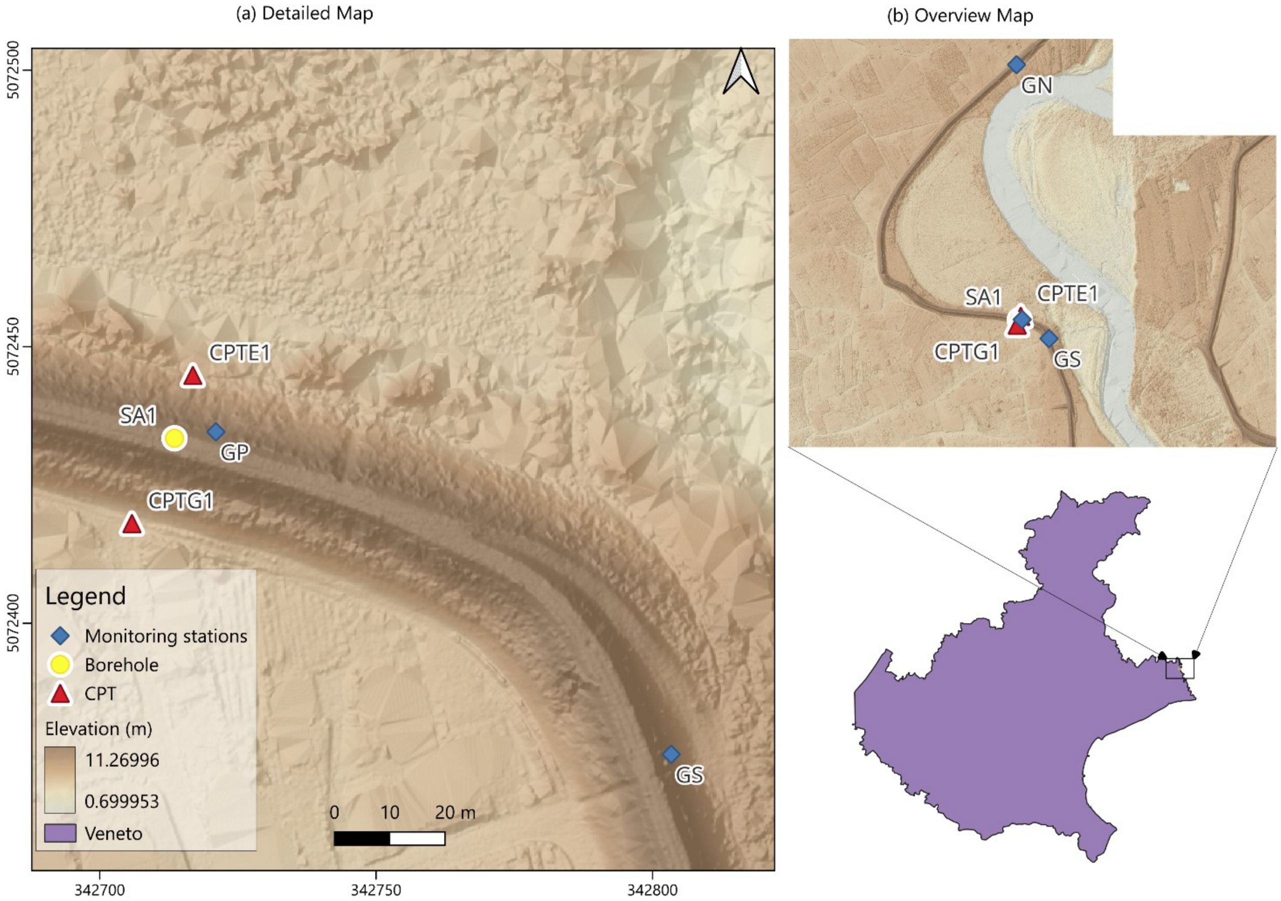

Figure 3.3 Plan-view maps of the San Giorgio monitoring sections and nearby in-situ investigations used for the local stratigraphic interpretation: (a) detailed map of the principal monitored area showing GP, GS, SA1, CPTG1, and CPTE1 over the DTM-derived topographic background; (b) overview map showing the three monitoring sections (GN, GP, GS) relative to the investigation points and their broader local context.

Figure 3.3 illustrates the spatial relationship between the San Giorgio monitoring sections and the principal in-situ investigations used in Chapter 3. The detailed map focuses on the principal monitored area and the nearby investigation points SA1, CPTG1, and CPTE1, which provide the main geotechnical reference points for the local stratigraphic interpretation. The overview panel places the three monitored sections GN, GP, and GS within the broader local setting, thereby clarifying the organization of the monitoring network and the relative position of the investigation points with respect to the levee system and surrounding topography. The DTM-derived background was included to provide a direct representation of the local elevation setting and to support the geomorphological reading of the monitored sector.

3.5 Borehole SA1 stratigraphy (reference lithology)

Borehole SA1 provides the most direct stratigraphic reference for the principal section, including lithological descriptions and sampling intervals. The SA1 log indicates a thin topsoil cover followed by a predominantly silty-sand sequence, with a local finer interval described as sandy slightly clayey silt, and a deeper transition to coarse deposits (fine gravel in sandy matrix). The main SA1 intervals are summarized below:

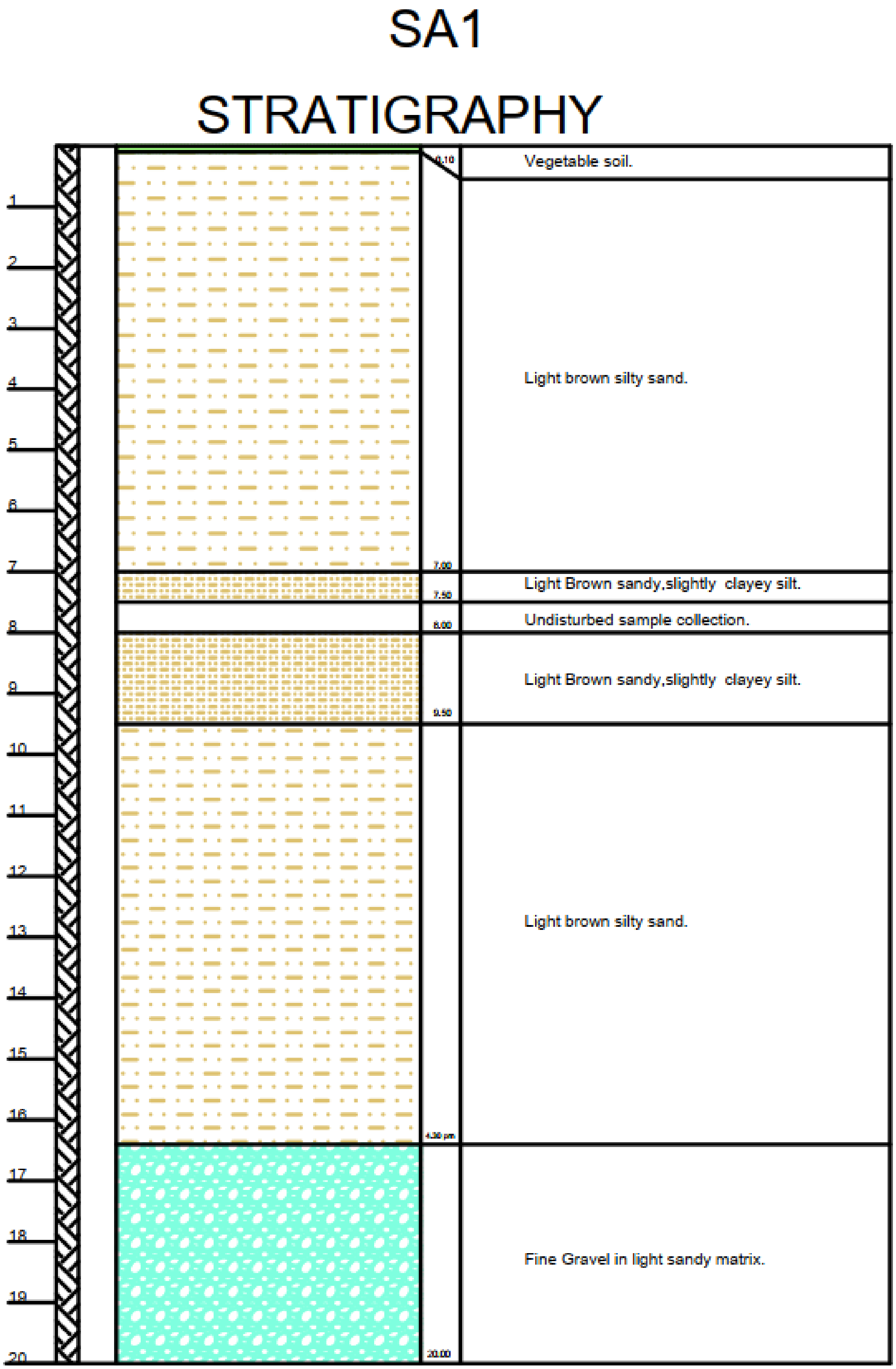

Figure 3.4 Borehole SA1 stratigraphic log (lithological description and sampling intervals) at the San Giorgio principal station (GP).

Table 3.1 Borehole SA1 stratigraphy summary (reference lithology).

Depth interval (m)	Lithological description	Interpretive note
0.00–0.10	Vegetable soil / topsoil	Very thin surface cover
0.10–7.00	Light brown silty sand	Dominant levee/foundation material
7.00–7.50	Light brown sandy, slightly clayey silt	Finer interlayer (upper part)
7.50–8.00	Undisturbed sample collection	Sampling interval (no lithology change implied)
8.00–9.50	Light brown sandy, slightly clayey silt	Finer interlayer (lower part)
9.50–16.30	Light brown silty sand	Return to silty sand
16.30–20.00	Fine gravel in light sandy matrix	Coarse basal deposits

The SA1 stratigraphy is used as the primary "ground truth" to anchor the CPT-based soil behavior interpretation and to constrain the presence and depth of the coarse basal unit.

3.6 CPT-based soil behavior interpretation at CPTG1 and CPTE1

Cone penetration tests provide continuous profiles with depth and support the identification of major stratigraphic changes and lateral variability across the levee. CPT interpretation in this thesis follows standard CPT soil-behavior classification logic (e.g., Robertson-type SBT), using parameters such as cone tip resistance (qc), sleeve friction (fs), friction ratio, and the soil behavior index (Ic). In general, lower Ic values indicate more sand-like behavior, while higher Ic values indicate more fine-grained (silt/clay-like) behavior.

3.6.1 CPTG1 – interpretation summary

Figure 3.5 summarizes the main CPTG1 trends by combining three complementary indicators: qc, Rf and Ic (soil behavior index). Near the ground surface, qc is relatively high while Rf remains generally low and Ic stays in the sand-to-silty sand range, indicating a predominantly granular behavior in the shallow portion of the profile. This supports the interpretation of an upper sandy/silty-sandy unit within the levee body and shallow foundation.

With increasing depth, the profile becomes more heterogeneous. Within the shallow-to-intermediate depths (consistent with the intervals later simplified in Table 3.2), qc shows a progressive reduction and local fluctuations, while Ic increases compared to the shallow part. This combination indicates a transition toward mixed behavior, where sandy layers are still present but the contribution of silt (and locally finer fractions) becomes more important. In the same depth range, Rf locally increases and becomes more variable, which is consistent with lenses or thin horizons where the material is less clean sand and more "mixed" (silty sand / sandy silt).

Below the main transition band, the deeper part of CPTG1 is characterized by lower qc and higher Ic on average, together with relatively low-to-moderate Rf. This pattern is typical of a profile moving toward finer soil behavior (silt/clayey-silt tendency), with lower hydraulic conductivity expected compared to the shallow granular unit. For cross-section purposes, these trends are not interpreted as many thin layers, but rather as a few major depth intervals capturing the dominant change from granular behavior near the surface to more mixed/finer behavior at depth, which is then correlated laterally with SA1 and CPTE1.

To support the interpretation of soil-behavior changes with depth, the Ic profile is shown together with qc and Rf. On the Ic panel, vertical dashed reference lines at Ic = 2.05, 2.60, and 2.95 are added following Robertson's boundaries to highlight transitions from sand-like to mixed and finer-grained behavior.

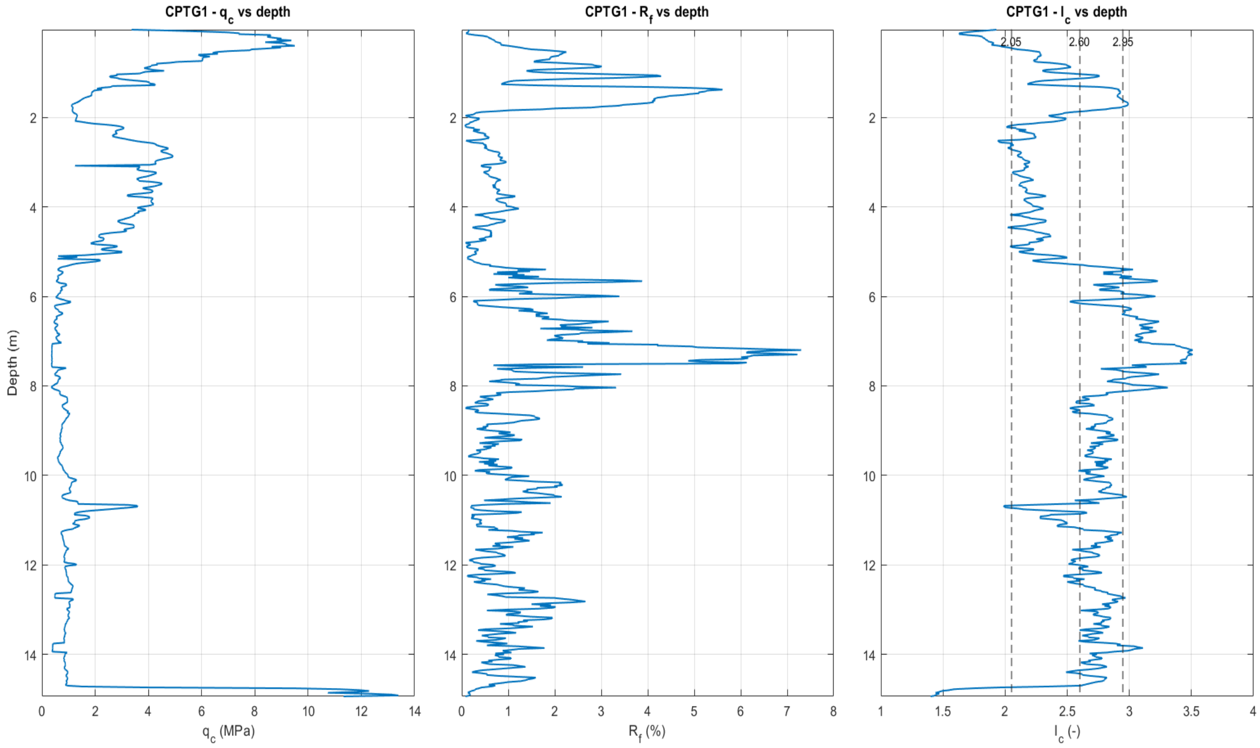

Figure 3.5 Composite CPTG1 profiles versus depth: cone tip resistance (qc), friction ratio (Rf), and soil behavior index (Ic)

The CPTG1 profile indicates a shallow sand-like unit and a transition to more fine-grained behavior with depth. For the purpose of cross-section correlation, the CPTG1 profile was simplified into major depth intervals that capture the dominant soil-behavior trends while avoiding over-fitting small fluctuations. The main CPTG1 interpretation adopted for the cross section is:

Table 3.2 CPTG1 interpretation summary used for cross-section correlation.

Depth interval (m)	Dominant soil behavior (simplified)	Use in cross-section
0.0–1.0	Sand / sand mixtures	Upper granular unit (shallow)
1.0–2.0	Transitional mixed behavior	Transition band
2.0–4.5	Sand & silty sand	Upper foundation unit
4.5–5.5	Transition to finer behavior	Boundary to fine unit
5.5–(profile base)	Predominantly finer behavior (clay-like tendency) within the available depth window	Lower mixed-to-fine unit; correlated cautiously due to lateral variability

Table 3.3 CPTG1 derived properties by unit (φ' and k ranges + qc/Rf/Ic means)

Unit (CPTG1)	**Depth (m)**	**qc mean (MPa)**	**Rf mean (%)**	**Ic mean (-)**	**φ′ mean (deg)**	**Indicative k (m/s)**	**k class (from Ic mean)**
Unit G1-1 (0–1 m)	0–1	6.33	1.20	1.63	37.3	[10^{-5} – 10^{-3}]	Sand to silty sand (permeable)
Unit G1-2 (1–2 m)	1–2	5.18	2.11	2.25	34.3	[10^{-8} – 10^{-5}]	Silt mixtures (moderate–low k)
Unit G1-3 (2–4.5 m)	2–4.5	3.35	1.48	1.90	33.0	[10^{-5} – 10^{-3}]	Sand to silty sand (permeable)
Unit G1-4 (4.5–5.5 m)	4.5–5.5	1.79	0.92	2.19	—	[10^{-8} – 10^{-5}]	Silt mixtures (moderate–low k)
Unit G1-5 (≥ 5.5 m)	5.5–15	1.22	0.88	2.89	—	[10^{-10} – 10^{-8}]	Clayey silt / clay (low k)

3.6.2 CPTE1 – interpretation summary

CPTE1 is located on the river-side portion of the San Giorgio monitored section and provides a continuous CPT profile to support the stratigraphic correlation across the levee. The interpretation is based on the main CPT measurements (cone tip resistance qc and sleeve friction fs) and derived indices such as friction ratio Rf and soil behavior index Ic. In addition, indicative material properties were estimated from standard CPT correlations, including an effective friction angle φ′ (representative of granular behavior) and an indicative permeability range k. These plots are used to identify the main vertical changes in soil behavior and to justify the subdivision into major depth units adopted in the cross-section correlation.

To support the interpretation of soil-behavior changes with depth, the Ic profile is shown together with qc and Rf. On the Ic panel, vertical dashed reference lines at Ic = 2.05, 2.60, and 2.95 are added following Robertson's boundaries to highlight transitions from sand-like to mixed and finer-grained behavior.

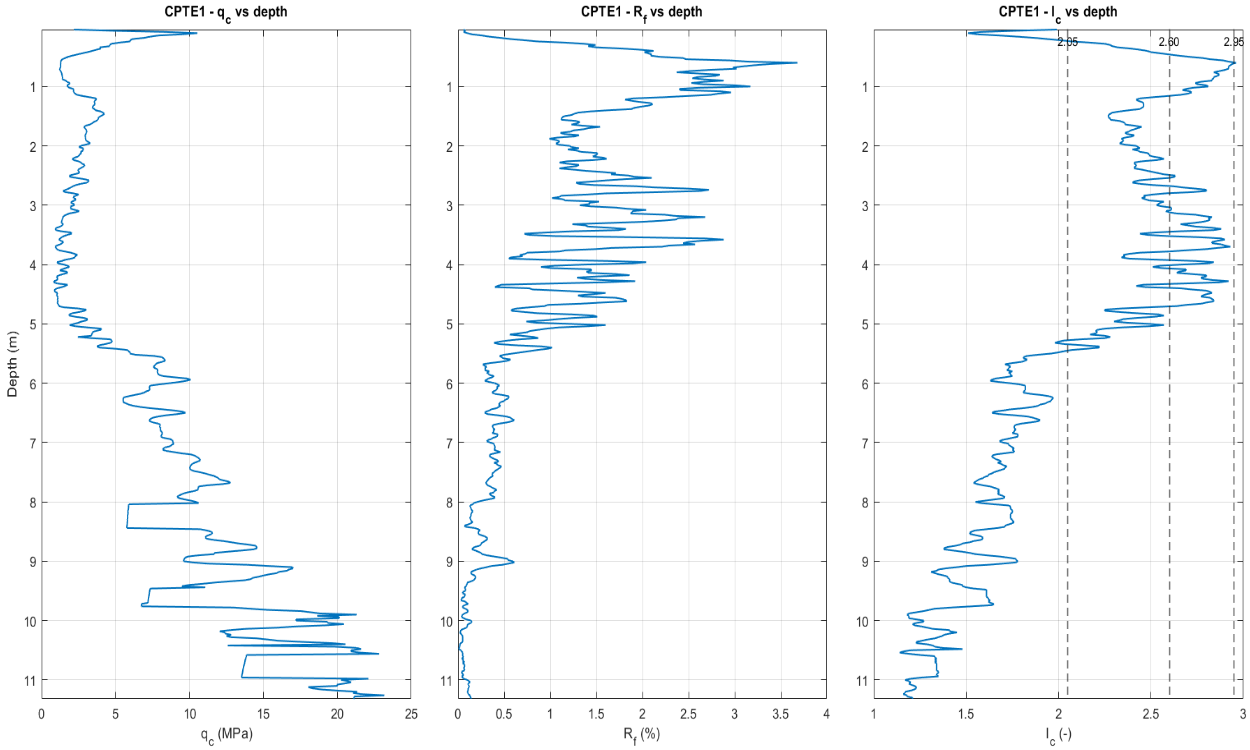

Figure 3.6 Composite CPTE1 profiles versus depth: cone tip resistance (qc), friction ratio (Rf), and soil behavior index (Ic)

Figure 3.6 provides the key CPT evidence for CPTE1 by showing qc, Rf, and Ic together. The shallow part of the profile is dominated by relatively low-to-moderate qc values and moderate Ic, with Rf locally elevated compared to deeper intervals. This suggests that the very shallow layers include mixed sandy–silty behavior, rather than clean sand only, which is consistent with near-surface variability at the river-side toe/levee margin.

From the intermediate depths downward, CPTE1 shows a clear shift toward more granular behavior. This is indicated by an overall increase in qc (including pronounced higher-resistance zones) together with generally low Rf and Ic values that remain mostly within the sand to silty-sand domain. The combination of high qc and low Ic/Rf is typical of dense granular deposits and supports the interpretation that the river-side portion includes a significant granular foundation package.

At the deepest part of the CPTE1 record, qc becomes distinctly higher and more sustained, while Rf remains very low and Ic decreases further. This is consistent with a dense sand unit at the base of the investigated depth range. In practical terms, this basal granular unit is important for the stratigraphic model because it implies higher permeability and a different hydraulic regime at depth compared with any finer interlayers identified closer to the crest in the principal section. For the cross-section correlation, these trends are simplified into a limited number of major intervals, ensuring the stratigraphy remains supported by the CPT signals without over-interpreting small-scale fluctuations.

The CPT profile at the river-side investigation point (CPTE1) shows an overall more granular behavior at intermediate-to-deep levels, including a dense sand unit at the base of the CPT record. The interpretation was simplified into major units for correlation as follows:

Table 3.4 CPTE1 interpretation summary used for cross-section correlation.

Depth interval (m)	Dominant soil behavior (simplified)	Use in cross-section
0.04–0.22	Sand / sand & silty sand	Very shallow granular cover
0.24–1.40	Silty sand & sandy silt	Mixed unit (upper)
1.42–1.96	Sand & silty sand	Granular lens
1.98–5.12	Silty sand & sandy silt	Mixed unit (middle)
5.14–9.76	Sand & silty sand	Granular foundation unit
9.78–11.32	Dense sand	Coarse basal unit (compatible with SA1 deep coarse deposits)

Table 3.5 CPTE1 CPT-derived parameters and indicative material properties by depth unit.

Unit (depth interval)	z from (m)	z to (m)	qc mean (MPa)	Rf mean (%)	Ic mean (-)	φ' mean (°)	Indicative k range (m/s)
Unit E1-1 (0.04–0.22 m)	0.04	0.22	7.09	0.23	1.19	37.7	$1 \times 10^{-5} – 1 \times 10^{-2}$ m/s
Unit E1-2 (0.24–1.40 m)	0.24	1.40	2.50	2.38	2.09	34.0	$1 \times 10^{-8} – 1 \times 10^{-3}$ m/s
Unit E1-3 (1.42–1.96 m)	1.42	1.96	3.36	1.23	1.96	34.4	$1 \times 10^{-8} – 1 \times 10^{-3}$ m/s
Unit E1-4 (1.98–5.12 m)	1.98	5.12	1.90	1.45	2.31	33.1	$1 \times 10^{-10} – 1 \times 10^{-3}$ m/s
Unit E1-5 (5.14–9.76 m)	5.14	9.76	8.89	0.35	1.64	38.8	$1 \times 10^{-8} – 1 \times 10^{-2}$ m/s
Unit E1-6 (9.78–11.32 m)	9.78	11.32	17.05	0.07	1.27	42.1	$1 \times 10^{-5} – 1 \times 10^{-2}$ m/s

3.7 Stratigraphic correlation along the San Giorgio principal cross section

Because SA1, CPTG1, and CPTE1 are located at different positions across the levee cross section, the stratigraphy cannot be assumed laterally uniform. The final section is therefore constructed as an interpreted correlation of local vertical profiles, anchored by SA1 lithology and supported by CPT soil-behavior profiles on the land-side and river-side.

To produce a consistent cross section, depth-based boundaries at each investigation point were converted to a common vertical reference (Z datum) using the local ground elevation at each point. Layer boundaries were then correlated across the section by connecting only major units supported by multiple sources and by allowing units to thicken, thin, or pinch out laterally where the CPT profiles suggest differences in soil behavior.

3.7.1 Final correlated unit model (used for the thesis cross-section figure)

The final correlated stratigraphic model used in the thesis figure includes five units, summarized below. Units are described in practical lithological terms consistent with SA1, while CPT-derived behavior is used to guide lateral continuity and variability.

Table 3.6 Final correlated stratigraphic unit model for the San Giorgio principal cross section.

Unit	Name (legend)	Interpretation
1	Topsoil / vegetated cover (local, very thin)	Thin surficial cover; not a controlling unit for deeper response
2	Upper silty sand / sand mixtures (levee fill + upper foundation)	Dominant sandy–silty material forming the embankment and shallow foundation; relatively permeable with moderate water retention
3	Finer lens: sandy, slightly clayey silt (local interlayer)	Local finer interlayer centered near the crest (confirmed in SA1); may influence vertical percolation and transient suction response
4	Lower silty sand / mixed sandy deposits (foundation unit)	Mixed sandy deposits beneath the finer lens; laterally variable thickness across the section
5	Coarse foundation: dense sand to fine gravel (fluvial deposits)	Coarser basal deposits consistent with fluvial foundation materials; likely higher permeability and distinct hydraulic behavior

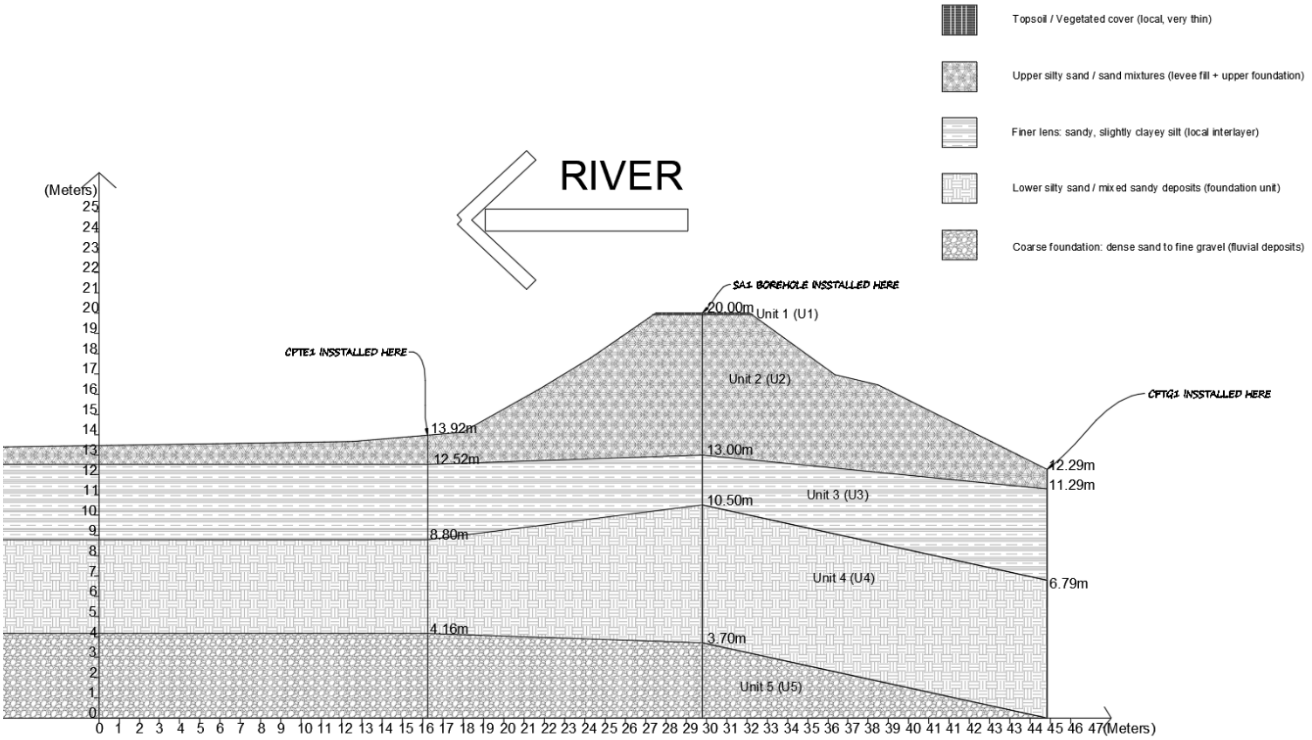

Figure 3.7 Interpreted stratigraphic cross section at the San Giorgio principal station (GP).

Figure 3.7 presents the interpreted stratigraphic framework across the San Giorgio principal levee section, constrained by borehole SA1 at the crest and by CPT soundings at CPTG1 (land-side) and CPTE1 (river-side). The stratigraphy is expressed in a common vertical datum (Z), allowing the depth-based boundaries at each investigation point to be correlated across the levee geometry while acknowledging lateral variability

Unit 1 – Topsoil / vegetated cover (local, very thin)

A very thin surficial cover is present at the ground surface. Its thickness is negligible compared with the underlying units and it is not expected to control deeper hydro-mechanical response. It mainly represents the superficial organic/vegetated layer recorded in SA1.

Unit 2 – Upper silty sand / sand mixtures (levee fill + upper foundation)

The upper part of the section is dominated by sandy–silty materials forming the levee body and the shallow foundation. In SA1, this unit is described as light brown silty sand over a large thickness, and it is consistent with the generally sand-like to silty-sand CPT behavior observed at shallow depths in both CPTG1 and CPTE1. The geometry of Unit 2 follows the embankment shape, indicating that a significant portion of the levee mass is composed of relatively permeable granular material with moderate fines content. This unit provides the primary pathway for rainfall infiltration and rapid near-surface moisture variations.

Unit 3 – Finer lens: sandy, slightly clayey silt (local interlayer)

A key feature of the section is the presence of a finer interlayer centered beneath the crest area. In SA1 this interval is described as sandy slightly clayey silt (between the surrounding silty sand units). In the cross section, this unit forms a lens-like geometry that is thickest near SA1 and becomes thinner laterally toward CPTG1 and CPTE1. This geometry is consistent with natural heterogeneity in embankment/foundation materials and/or localized depositional variability. From a hydro-mechanical perspective, the finer lens is expected to have lower permeability and higher water retention compared with the surrounding silty sand, potentially creating local contrasts in infiltration rate, drainage, and suction evolution. This unit therefore represents a plausible stratigraphic control on delayed or amplified responses observed in monitoring data at certain depths/locations.

Unit 4 – Lower silty sand / mixed sandy deposits (foundation unit)

Below the finer lens, the section transitions back to mixed sandy deposits consistent with silty sand behavior. In SA1, silty sand dominates again beneath the finer interval, and both CPTG1 and CPTE1 indicate mixed granular behavior at intermediate depths. The base of Unit 4 varies laterally, suggesting changes in the depth to the coarse foundation unit across the levee. This unit likely forms the main intermediate foundation package and may provide hydraulic connectivity between the levee body and deeper deposits, depending on local grain-size distribution and saturation conditions.

Unit 5 – Coarse foundation: dense sand to fine gravel (fluvial deposits)

The deepest unit represents the coarse basal deposits interpreted as fluvial foundation material. SA1 records a transition to fine gravel in a light sandy matrix at depth, confirming the presence of a coarse layer beneath the sandy–silty sequence. On the river-side (CPTE1), the CPT profile shows a strongly granular response at depth (including a dense sand interval), which is consistent with the expected behavior of coarse fluvial deposits even if the CPT does not explicitly label “gravel.” The cross section suggests that this coarse unit is relatively continuous but varies in elevation across the section, rising toward the river-side compared with the central crest zone. This geometry is important because it implies a distinct hydraulic regime at depth, with higher permeability and potentially different boundary conditions for deeper sensors and for river-stage influence.

Lateral variability and interpretation confidence

Differences between CPTG1, SA1, and CPTE1 reflect real lateral heterogeneity across the levee section as well as the difference between direct lithological description (borehole) and CPT soil-behavior classification. For this reason, the section correlation emphasizes major units and avoids over-fitting small-scale CPT fluctuations. The resulting model should be interpreted as a defensible stratigraphic hypothesis constrained by available evidence, suitable for supporting the monitoring interpretation in subsequent chapters.

3.8 Implications for monitoring interpretation

The stratigraphic framework provides the physical basis for interpreting spatial and depth-dependent patterns in the monitoring data. The prevalence of silty sand and sand mixtures in the levee body suggests relatively fast hydraulic communication for rainfall-driven events, while the presence of a finer interlayer In the interpreted cross section (**Error! Reference source not found.**), the finer interlayer corresponds to **Unit 3 (U3)**, a lens of **sandy, slightly clayey silt** located beneath the crest area (around **z ≈ 10.5–13 m**, thickest near **SA1**) and thinning laterally toward CPTG1 and CPTE1 may promote localized retention, delayed drainage, and stronger suction variability. At depth, the transition to coarse deposits implies a change in hydraulic regime and potentially different boundary conditions for deep sensors, especially near the river-side portion of the section. These considerations guide the interpretation of seasonal trends and forcing-response relationships presented in Chapters 5–7.

3.9 Chapter summary

This chapter introduced the study area and the monitoring network with focus on the San Giorgio principal station. A stratigraphic framework was developed by combining the SA1 borehole lithology, CPT soil-behavior interpretations at CPTG1 and CPTE1, and the updated levee geometry. The resulting five-unit model captures the main vertical stratification and lateral variability across the levee and provides the foundation for the monitoring quality control, performance evaluation, and seasonal interpretation in the subsequent chapters.

Chapter 4 Laboratory Investigations, Soil Classification, and Hydraulic Characterization

4.1 Introduction

This chapter presents the laboratory investigations carried out to define the main physical and index properties of the soils within the San Giorgio monitoring area. The laboratory dataset consists of **61 samples** collected from the **N, P, and S stations**. For each sample, the particle-size distribution was determined through sieve and hydrometer analyses, allowing the coarse and fine fractions to be evaluated within a unified granulometric framework. In addition, Atterberg limits were determined for the subset of samples exhibiting plastic behavior, while the remaining materials were classified as non-plastic according to the adopted interpretation workflow.

The main objective of this chapter is to provide a material-based characterization of the monitored soils before discussing the quality control, sensor performance, and seasonal response analyses developed in the following chapters. The laboratory results are used to quantify grain-size variability, distinguish between plastic and non-plastic materials, and classify the tested soils according to the Unified Soil Classification System (USCS). In addition, the chapter introduces a first hydraulic interpretation of representative soils through soil-water retention behaviour discussed in relation to laboratory and basic geotechnical properties. In this way, Chapter 4 provides the link between the stratigraphic framework presented in Chapter 3 and the broader hydro-mechanical interpretation developed later in the thesis.

4.2 Laboratory methods

This section describes the laboratory methods used to characterize the soil samples collected from the San Giorgio monitoring area. The main purpose of the laboratory work was to define the particle-size distribution of the investigated soils and, where necessary, evaluate their plasticity behavior. To do this, three types of laboratory tests were considered: **sieve analysis**, **hydrometer analysis**, and **Atterberg limits tests using the Casagrande method**. The sieve and hydrometer analyses were carried out on all **61 samples**, while the Atterberg limits tests were performed only on the samples that showed plastic behavior.

The combination of these tests made it possible to describe the soils in a consistent way, from both a granulometric and a geotechnical point of view. The grain-size distribution obtained from sieve and hydrometer analyses was used to define the relative proportion of coarse and fine fractions in each sample, while the Atterberg limits provided additional information on the consistency of the fine-grained materials. Taken together, these results formed the basis for both the descriptive soil classification and the final classification according to the **Unified Soil Classification System (USCS)**.

4.2.1 Sieve analysis

Sieve analysis was performed in order to characterize the coarser fraction of each soil sample. The test made it possible to evaluate the distribution of particles within the sand range and, where present, the coarsest fraction of the material. In practical terms, the method is based on passing the soil through a series of sieves with decreasing opening size and measuring the amount of material retained on each one. From this, the percentage passing can be determined and the coarser part of the grain-size distribution can be reconstructed.

In this study, sieve analysis provided the first general indication of whether a sample was mainly sandy or whether the coarse fraction was relatively limited compared with the fine material. However, because many of the San Giorgio samples contained a significant fine-grained component, sieve analysis alone was not enough to describe the soil completely. For this reason, the sieve results were always interpreted together with the hydrometer results in order to obtain the full particle-size distribution.

4.2.2 Hydrometer analysis

Hydrometer analysis was carried out on all samples to describe the finer fraction of the soil, especially the silt- and clay-sized particles that cannot be properly characterized by sieve analysis alone. The method is based on the sedimentation behavior of particles in suspension, where finer particles settle more slowly than coarser ones. By monitoring this process, it is possible to estimate the distribution of the fine-grained fraction.

In the present work, hydrometer analysis was particularly important because many of the tested samples showed a clear fine-grained component. The hydrometer results therefore complemented the sieve analysis and made it possible to extend the particle-size distribution into the finer range. Once combined, the sieve and hydrometer results provided a continuous grain-size distribution curve for each sample, which was then used to support the descriptive interpretation of the soil composition.

4.2.3 Atterberg limits tests (Casagrande method)

Atterberg limits tests were performed only on the samples that showed plastic behavior during the classification process. In total, **11 samples** were tested using the **Casagrande method** to determine the **liquid limit (LL)** and **plastic limit (PL)**. The **plasticity index (PI)** was then calculated as the difference between these two values.

These parameters are useful for evaluating the consistency behavior of fine-grained soils and for distinguishing between materials that are non-plastic and those that exhibit measurable plasticity. Since most of the samples analyzed in this study were non-plastic, Atterberg limits were not determined for the entire dataset. Instead, they were limited to the smaller subset of soils for which plastic behavior was observed. For these samples, the Atterberg limits were used together with the grain-size distribution results to support the final USCS classification.

Overall, the Atterberg limits results showed that the plastic samples identified in the dataset are generally associated with **low-plasticity fine-grained soils**, which is consistent with the final predominance of **ML** within the plastic subset.

4.2.4 Integration of laboratory results for soil classification

The laboratory results were interpreted through a combined workflow rather than as separate independent outputs. First, sieve and hydrometer analyses were used together to reconstruct the complete grain-size distribution of each sample. On this basis, a descriptive soil name was assigned according to the relative proportions of the main fractions, such as silt, fine sand, and medium sand. In the cases where plastic behavior was observed, the Atterberg limits results were then used to refine the classification and define the final USCS class.

This combined approach made it possible to classify each soil sample using both its particle-size characteristics and its consistency behavior. As a result, the final laboratory dataset is not limited to raw test results, but provides an integrated interpretation of the soils encountered at the San Giorgio monitoring stations. This dataset forms the basis for the results and discussion presented in the following sections.

4.3 Sampling program and dataset

The laboratory dataset considered in this study consists of **61 soil samples** collected from the San Giorgio area, including samples from the **N, P, and S monitoring stations**. The samples were taken from different depths in order to provide a representative characterization of the soils forming both the levee body and the underlying foundation materials. The main purpose of the laboratory program was to define the particle-size distribution of the investigated soils, evaluate their plasticity behavior where relevant, and support their geotechnical classification within the general framework of the thesis.

For each of the 61 samples, both a **sieve analysis** and a **hydrometer analysis** were performed in order to reconstruct the complete grain-size distribution over the full range of particle sizes, from the coarsest fractions to the fine-grained portion. The results of these analyses were first organized in a main Excel results file containing the grain-size distribution data for each sample. In parallel, an individual grain-size distribution curve was prepared for every sample, and each curve was interpreted descriptively by assigning a soil name based on the relative proportions of silt, fine sand, medium sand, and other relevant fractions. These descriptive soil classifications were originally assigned in Italian and were subsequently translated into English to ensure consistency throughout the thesis.

A further classification step was then carried out by evaluating the plasticity behavior of the samples. **Atterberg limits tests using the Casagrande method** were performed only on the subset of soils that showed plastic behavior. In total, **11 samples** were subjected to Atterberg limits testing, while the remaining samples were classified as **non-plastic (NP)**. For the plastic subset, the **liquid limit (LL)**, **plastic limit (PL)**, and **plasticity index (PI)** were determined and then used together with the grain-size distribution results to define the final soil class according to the **Unified Soil Classification System (USCS)**.

The final Chapter 4 dataset was organized into a master summary file including, for each sample, the **sample ID, station, depth, descriptive soil classification, plastic or non-plastic behavior, liquid limit, plastic limit, plasticity index, and final USCS class**. The complete sample-by-sample master table is reported in **Appendix 4.A** and forms the basis for the grain-size, plasticity, and classification results discussed in the following sections.

4.4 Construction of grain-size distribution curves

Following the laboratory testing phase, the results of the sieve and hydrometer analyses were combined in order to construct a complete grain-size distribution curve for each sample. Since sieve analysis describes the coarser fraction of the soil and hydrometer analysis characterizes the finer fraction, the combination of the two methods made it possible to represent the full particle-size distribution in a single continuous curve. This procedure was applied to all **61 samples** considered in the Chapter 4 dataset.

For each sample, the grain-size distribution curve was plotted with **particle diameter on the horizontal axis** and **percentage passing on the vertical axis**. In this way, the curve provides a synthetic representation of the relative proportion of coarse and fine particles within the soil. The general shape and position of the curve were then used to support the interpretation of the material as predominantly silty, sandy-silty, or characterized by mixed fractions.

These curves played an important role in the classification workflow adopted in this study. First, they allowed a direct visual comparison among samples from different stations and depths. Second, they provided the basis for assigning a descriptive soil name to each sample according to the relative proportion of silt, fine sand, medium sand, and other relevant fractions. Finally, for the subset of soils showing plastic behavior, the grain-size interpretation was combined with the Atterberg limits results in order to define the final USCS classification.

Given the large number of tested samples, the grain-size distribution curves are discussed comparatively in the following section in order to highlight their overall similarity, variability, and grouping tendencies. The complete set of grain-size distribution curves for all samples is reported in **Appendix 4.B**.

4.5 Particle-size distribution results

4.5.1 General overview of the tested soils

The grain-size distribution results show that the soils investigated in the San Giorgio dataset are characterized mainly by mixtures of silt and fine sand, with some variation from one station and depth to another. In general, the curves indicate that the tested materials do not correspond to a single uniform soil type, but rather to a heterogeneous succession of predominantly silty soils, silty sands, and fine sand–silt mixtures. This variability is consistent with the depositional complexity already highlighted in the site stratigraphy and confirms that the monitored embankment and foundation materials cannot be described by a single granulometric pattern.

A significant number of samples are dominated by a fine-grained fraction and were descriptively classified as silt with fine sand, silt with traces of fine sand, or silt with fine sand and traces of medium sand. At the same time, other samples show a more pronounced sandy component and were classified descriptively as fine sand with silt or fine sand with silt and traces of medium sand. This confirms that the dataset includes both predominantly silty materials and soils with a stronger sandy contribution.

The grain-size curves also provided the first basis for distinguishing between non-plastic and plastic materials. In most cases, the interpreted granulometric composition was associated with non-plastic behavior, while the smaller subset of plastic samples was later refined through Atterberg limits testing and classified within the ML group. For this reason, the particle-size distribution curves represent the first and most important step in the overall classification workflow adopted in Chapter 4.

4.5.2 Comparative interpretation of the grain-size distribution curves

To evaluate the overall granulometric behavior of the tested materials, the grain-size distribution curves were considered together in a comparative form rather than as isolated individual examples. This approach makes it possible to assess whether the investigated soils follow a common trend or whether distinct granulometric families can be recognized within the dataset.

Error! Reference source not found. shows the complete set of grain-size distribution curves for the t ested samples. Although some dispersion is visible, the curves occupy a relatively consistent range and confirm that the San Giorgio soils are mainly composed of silty to sandy-silty materials. Most of the curves lie within a similar granulometric envelope, indicating that the investigated materials share a broadly comparable fine-dominated structure, while still exhibiting local differences in the relative contribution of fine sand and silt.

At the same time, the combined plot also highlights that the dataset is not fully uniform. Some curves are shifted slightly toward the coarser side, reflecting samples with a more evident sandy component, whereas others remain more clearly concentrated in the finer range and are consistent with predominantly silty soils. Therefore, the comparative representation confirms both the general similarity of the tested materials and the presence of secondary variability within the soil profile.

This type of presentation is particularly useful because it allows the main tendencies of the dataset to be seen immediately without overemphasizing isolated samples. In this way, the grain-size distribution results can be interpreted at the scale of the whole laboratory program, which is more consistent with the objective of defining the general granulometric character of the San Giorgio levee and foundation materials.

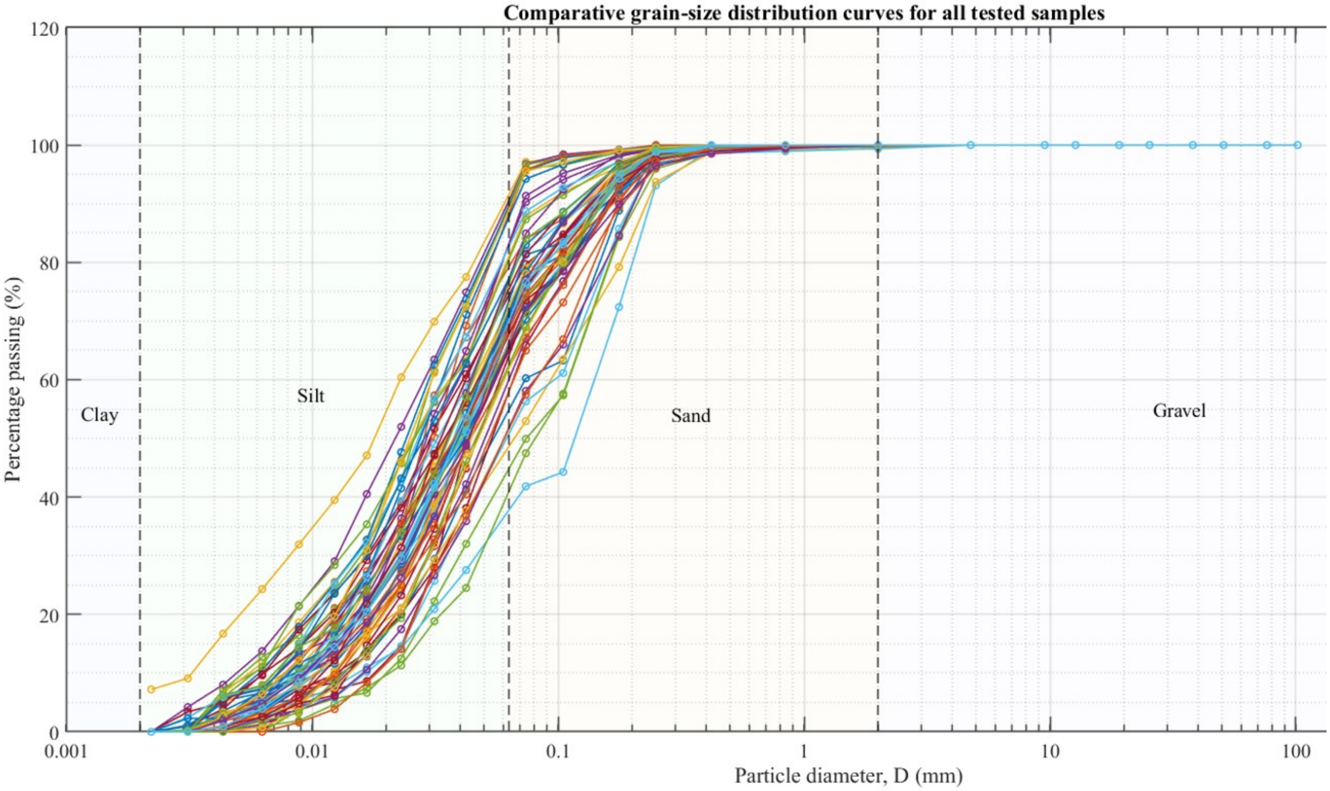

Figure 4.1 Comparative grain-size distribution curves for all tested samples in the San Giorgio laboratory dataset.

The comparative plot confirms that the tested materials are predominantly fine-dominated and occupy a relatively consistent granulometric range, with most curves clustering within the silty to sandy-silty field. At the same time, the spread among the curves indicates that the dataset is not fully uniform, but includes local variations in the relative proportion of silt and fine sand. This combined representation therefore supports the interpretation of the San Giorgio soils as heterogeneous materials sharing a broadly similar granulometric character.

4.5.3 Spatial and depth-related variability

From a spatial point of view, the grain-size distribution curves indicate that the **N, P, and S stations** share a generally similar tendency toward silty and sandy-silty materials, but with local variations in the relative proportion of the fine and sandy fractions. Some samples from the N and S stations appear more clearly dominated by silt with limited sand contribution, whereas several samples from the P station show a more evident presence of fine sand. This does not imply a strict station-based separation of soil types, but it does highlight the lateral variability of the investigated material.

Depth also plays an important role in the interpretation of the dataset. In some cases, shallow samples show a stronger sandy component, while deeper samples tend to be more clearly silty. In other cases, the opposite trend is observed locally, confirming that the vertical evolution of the soil profile is not uniform across the monitored area. This variability with depth further supports the need to interpret the San Giorgio stratigraphy as a heterogeneous system composed of interlayered materials rather than as a sequence of laterally continuous uniform soils.

Taken together, the particle-size distribution results provide a consistent picture of the geotechnical nature of the tested soils and form the basis for the Atterberg limits assessment and final soil classification discussed in the following sections.

4.6 Atterberg limits and plasticity assessment

4.6.1 Plastic subset of samples

As discussed in the previous sections, the grain-size distribution analysis provided the first basis for the descriptive classification of all tested soils. However, for the subset of samples that exhibited plastic behavior, a further level of characterization was required. For this reason, **Atterberg limits tests using the Casagrande method** were carried out on the samples identified as plastic during the classification process.

In total, **11 samples** were subjected to Atterberg limits testing. These samples represent the plastic subset within the overall laboratory dataset of 61 tested soils. The remaining samples did not show measurable plastic behavior and were therefore classified as **non-plastic (NP)**. The plastic samples are distributed across the **N, P, and S stations**, indicating that plastic behavior is not limited to a single part of the monitored area. At the same time, the number of plastic samples remains relatively small compared with the full dataset, confirming that the San Giorgio soils are predominantly non-plastic or only weakly plastic in nature.

4.6.2 Atterberg limits results

For the 11 plastic samples, the **liquid limit (LL)** and **plastic limit (PL)** were determined using the Casagrande method, and the **plasticity index (PI)** was calculated as the difference between the two values. These parameters provide a quantitative description of the consistency behavior of the fine-grained fraction and make it possible to distinguish between different levels of plasticity.

The results obtained in this study show generally **low values of plasticity index**, indicating that the tested plastic samples do not correspond to highly plastic fine soils. In the analyzed subset, the LL values are low to moderate, and the PI values remain limited, which is consistent with soils of relatively modest plasticity.

Table 4.1 summarizes the Atterberg limits results obtained for the plastic subset of the San Giorgio laboratory dataset. For each of the 11 tested samples, the table reports the station, sampling depth, liquid limit (LL), plastic limit (PL), plasticity index (PI), and final USCS classification.

Table 4.1 Atterberg limits results for the plastic subset of samples tested in Chapter 4.

Sample ID	Station	Depth (m)	LL (%)	PL (%)	PI (%)	Final USCS class
GN2V2.0	N	2.00	16	13	3	ML
GN3V0.5	N	0.50	24	21	3	ML
GN3V1.0	N	1.00	21	19	2	ML
GP4V1.5	P	1.50	24	22	2	ML
GP5H2.5	P	2.50	24	21	3	ML
GP5H4.0	P	4.00	25	24	1	ML
GP7H1.0	P	1.00	28	23	5	ML
GP8 1.0	P	1.00	23	21	2	ML
GS5V0.5	S	0.50	13	11	2	ML
GS5V1.0	S	1.00	15	14	1	ML
GS6T4.0	S	4.00	19	15	4	ML

4.6.3 Casagrande plasticity chart

In addition to the tabulated LL and PI values, the Atterberg limits results were represented in the **Casagrande plasticity chart** in order to visualize the position of all tested points within the standard plasticity classification framework. The chart provides a synthetic interpretation of the consistency behavior of the fine-grained soils and makes it possible to evaluate whether the tested samples fall within a low-, medium-, or high-plasticity range.

As shown in **Figure 4.2**, the 11 tested samples cluster within the **low-plasticity field**, confirming that the fine-grained soils identified in the dataset are characterized by limited plasticity. The overall position of the points is consistent with the laboratory evidence obtained from both the grain-size distribution and Atterberg limits testing, and supports the interpretation of the plastic subset as composed of **low-plasticity silty materials**.

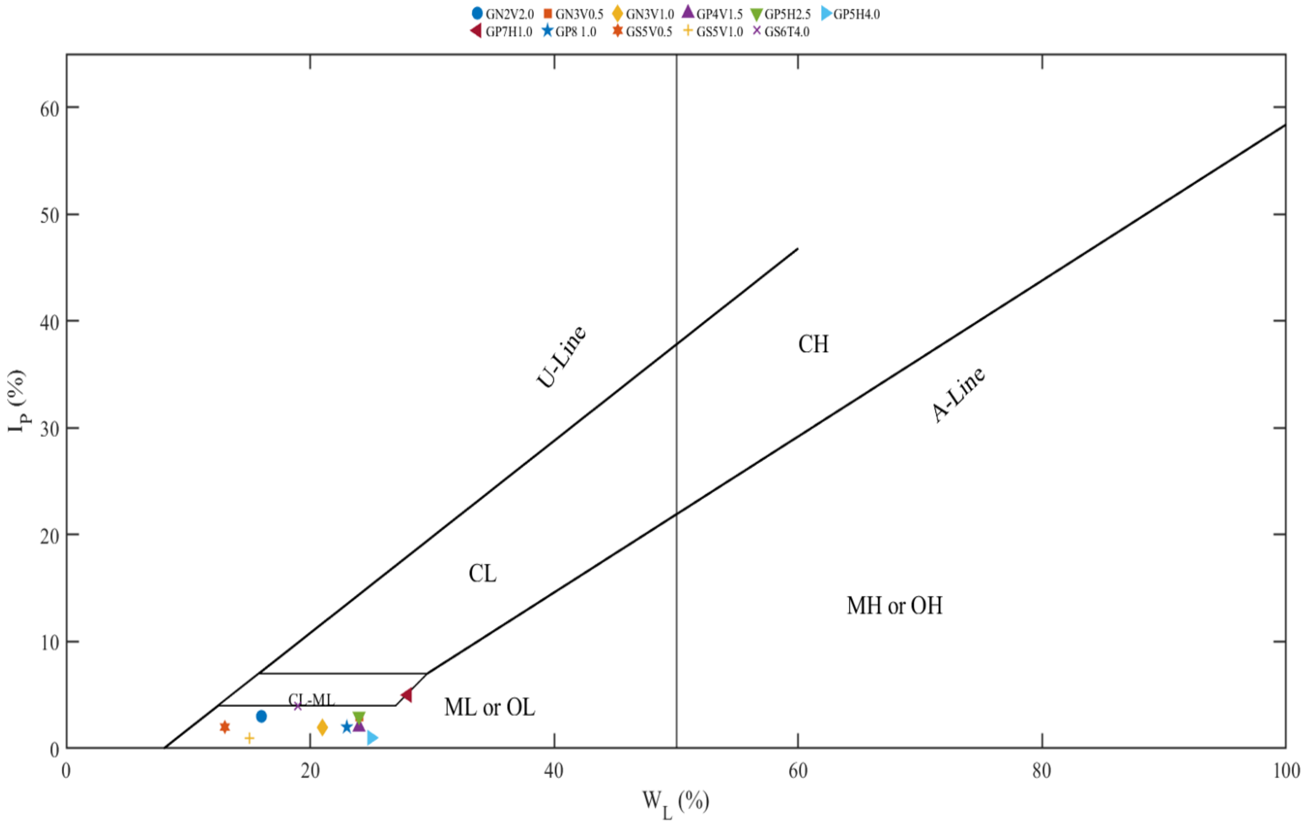

Figure 4.2 Casagrande plasticity chart for the 11 samples tested by Atterberg limits in the San Giorgio laboratory dataset.

The Casagrande chart confirms that the tested points are grouped within the low-plasticity domain, in agreement with the low PI values reported in Table 4.2. This result supports the interpretation that the plastic subset of the San Giorgio soils is composed mainly of low-plasticity silty materials rather than highly plastic fine-grained soils.

4.6.4 Interpretation of plasticity behavior

The Atterberg limits results confirm that plasticity is present only in a restricted subset of the San Giorgio samples and that, even within this subset, the degree of plasticity is generally low. This is an important result because it helps clarify the geotechnical nature of the investigated soils. The laboratory dataset is dominated by silty and sandy-silty materials, while the finer soils that do show plastic behavior still remain within a **low-plasticity range**.

This behavior is consistent with the grain-size distribution results discussed in Section 4.5. Although several of the plastic samples are dominated by fine fractions, they still contain an appreciable contribution from fine sand. As a result, the soils do not behave as highly plastic clays, but rather as silty materials with limited plasticity.

From a classification point of view, the Atterberg limits tests provided the additional information required to refine the interpretation of those samples that could not be fully characterized on the basis of grain-size distribution alone. In this sense, the plasticity assessment acted as a complementary step to the granulometric analysis, allowing the final USCS class to be assigned with greater confidence. Overall, the results suggest that the soils encountered in the San Giorgio monitoring area are mainly characterized by a fine-grained to mixed silty-sandy composition, with plastic behavior occurring locally and at relatively low intensity. This interpretation is consistent with the predominance of **ML** within the plastic subset and supports the broader view of the levee materials as heterogeneous but generally low-plasticity soils.

4.7 Estimation of soil-water retention behaviour from laboratory/basic geotechnical properties

4.7.1 Aubertin-based estimation approach

In addition to the grain-size and plasticity characterization presented in the previous sections, a first estimate of the hydraulic behaviour of representative soils was developed using the predictive framework proposed by **(Aubertin et al., 2003)**. In this approach, the soil-water retention curve (SWRC) is estimated from basic geotechnical properties rather than from direct suction-controlled laboratory measurements. This makes the method suitable for preliminary hydraulic interpretation when complete laboratory SWRC data are not available.

The Aubertin model relates the retention behaviour of a soil to parameters such as grain-size characteristics, liquid limit, porosity or void ratio, and material type. In the present study, this approach was adopted to obtain a first material-based estimate of the retention response of representative San Giorgio soils. Since direct laboratory SWRC tests were not available for the investigated samples, the estimated curves should be interpreted as predictive hydraulic trends rather than as direct measurements.

4.7.2 Input parameters and assumptions

Three representative samples were selected in order to cover the main soil types identified in the Chapter 4 dataset: a predominantly silty non-plastic sample (**GN2V0.5**), a sandy-silty non-plastic sample (**GP3V0.5**), and a low-plasticity silty sample classified as **ML** (**GN2V2.0**). For the non-plastic samples, the predictive estimation was based primarily on the grain-size parameters **D10** and **CU**, while for the ML sample the **liquid limit** was used as the principal index parameter in accordance with the fine-grained formulation proposed by Aubertin et al. (2003).

The value of **D10** was determined from the grain-size distribution curves by interpolation at 10% passing, while **CU** was obtained as the ratio between **D60** and **D10**. For the selected samples, the estimated values are: **GN2V0.5: D10 ≈ 0.0139 mm, CU ≈ 4.54; GP3V0.5: D10 ≈ 0.00635 mm, CU ≈ 7.45; GN2V2.0: D10 ≈ 0.0103 mm, CU ≈ 5.16**. For **GN2V2.0**, the Atterberg limits results gave **LL = 16%, PL = 13%, and PI = 3%**, confirming its low-plasticity silty character.

Because the **void ratio** was not directly measured for the selected samples, a sensitivity analysis was performed using three assumed representative values: **e = 0.6, 0.8, and 1.0**. These values were selected to explore the influence of porosity on the estimated retention behaviour and to assess how strongly the predicted curves depend on this missing parameter.

4.7.3 Sensitivity of estimated WRC to void ratio

The sensitivity analysis was carried out by recalculating the estimated WRC for each representative soil under the three assumed void ratio values. In this way, the effect of a denser material state (**lower e**) and a looser material state (**higher e**) could be compared directly. This step is particularly important because the Aubertin framework explicitly includes the influence of void ratio, and the lack of direct measured values would otherwise introduce uncertainty that is difficult to quantify.

The sensitivity analysis shows that the assumed void ratio has a clear effect on the predicted retention behaviour. In general, for the same soil type, lower void ratio values produce lower estimated water contents, whereas higher void ratio values shift the predicted curves upward. As a result, the sensitivity analysis does not provide a single unique SWRC for each sample, but rather a plausible range of estimated hydraulic responses consistent with the available geotechnical information.

4.7.4 Estimated WRCs for representative soils

The estimated WRCs for the representative samples are shown in the following figures. The two non-plastic samples (**GN2V0.5** and **GP3V0.5**) were selected to illustrate the difference between a more clearly silty material and a sandy-silty mixture, while the ML sample (**GN2V2.0**) was used to represent the low-plasticity fine-grained subset identified through Atterberg limits testing.

The estimated curves suggest that the selected soils share a generally fine-dominated hydraulic response, but with noticeable differences in retention behaviour. The silty non-plastic sample and the ML sample tend to retain more water over a wider suction range than the sample with a stronger sandy component. At the same time, the void-ratio sensitivity confirms that uncertainty in porosity can significantly affect the absolute position of the predicted curve. For this reason, the figures are best interpreted comparatively rather than as exact material calibration curves.

The estimated soil-water retention curves obtained for the representative samples are presented below. The two non-plastic soils, GN2V0.5 and GP3V0.5, were selected to illustrate the variation in predicted hydraulic behaviour within the silty to sandy-silty subset, while GN2V2.0 was used to represent the low-plasticity ML materials identified through Atterberg limits testing. For each sample, the curves were calculated using the Aubertin-based predictive approach with three assumed void-ratio values ($e = 0.6$, 0.8, and 1.0), in order to evaluate the sensitivity of the estimated retention behaviour to porosity assumptions.

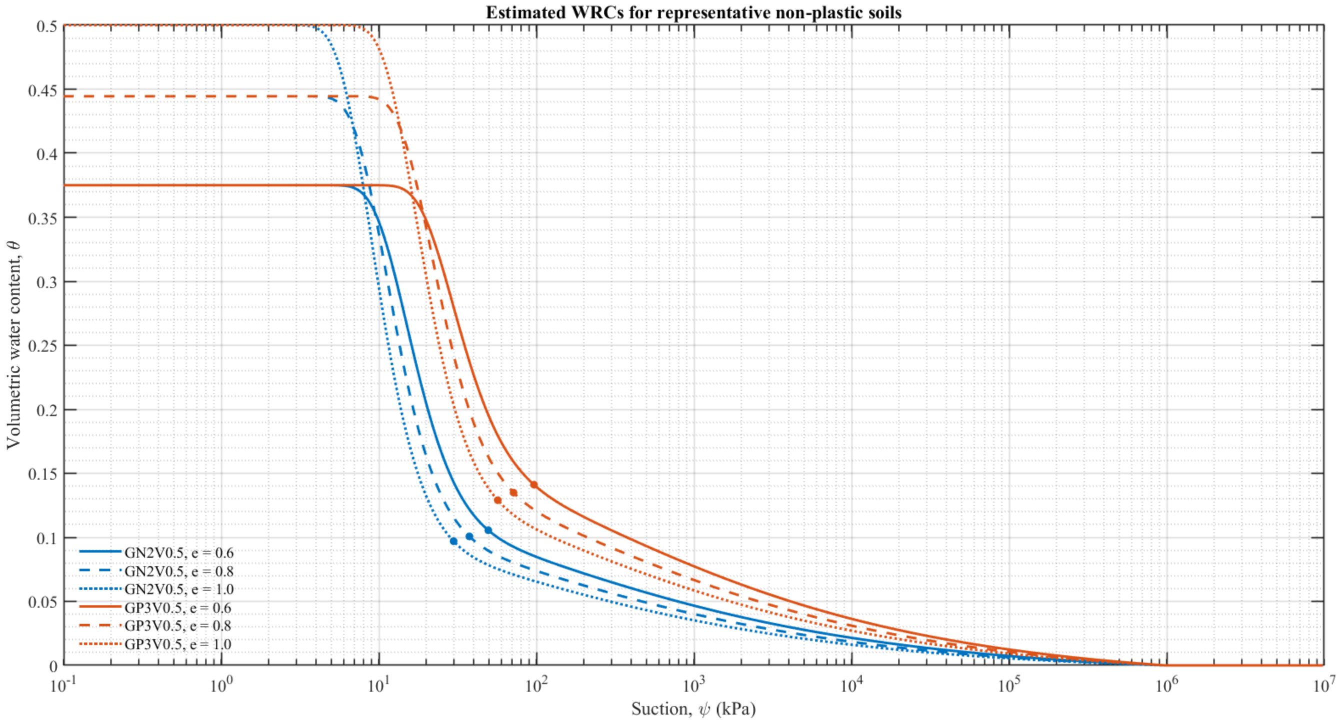

Figure 4.3 Estimated WRCs (θ–ψ) for representative non-plastic soils (GN2V0.5 and GP3V0.5) using the Aubertin-based approach, for e = 0.6, 0.8, and 1.0.

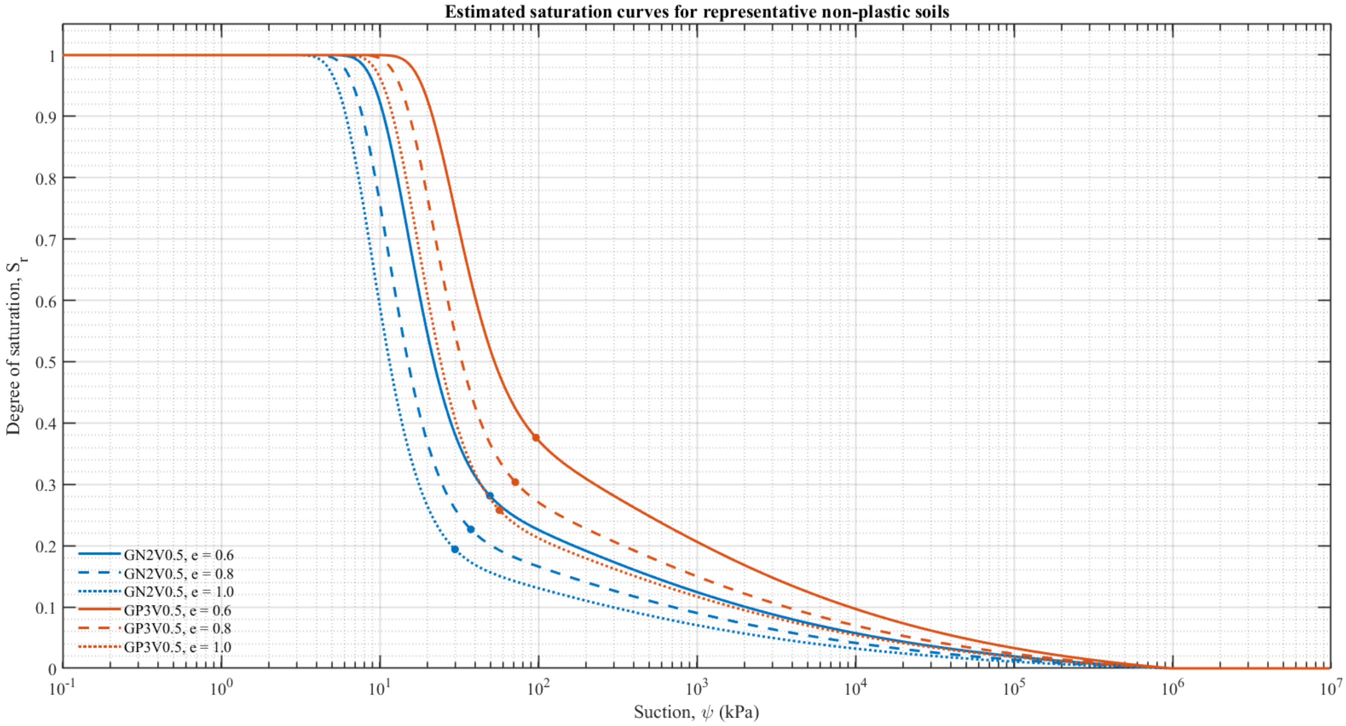

Figure 4.4 Estimated saturation curves (Sr–ψ) for representative non-plastic soils (GN2V0.5 and GP3V0.5) using the Aubertin-based approach, for e = 0.6, 0.8, and 1.0.

Figure 4.3 compares the estimated soil-water retention behaviour of the two representative non-plastic soils, GN2V0.5 and GP3V0.5, for three assumed void-ratio values. The estimated curves indicate a clear difference between the two materials, with GP3V0.5 consistently showing higher volumetric water contents than GN2V0.5 at the same suction levels. Within the adopted predictive framework, this suggests that GP3V0.5 exhibits a stronger retention behaviour, whereas GN2V0.5 undergoes a relatively faster desaturation response. The sensitivity analysis also shows that the assumed void ratio has a systematic influence on the position of the curves. In the present implementation, higher void-ratio values produce lower estimated volumetric water contents for a given suction. This trend reflects the behaviour of the adopted Aubertin-based formulation and should therefore be interpreted within the context of the model assumptions rather than as a general physical rule.

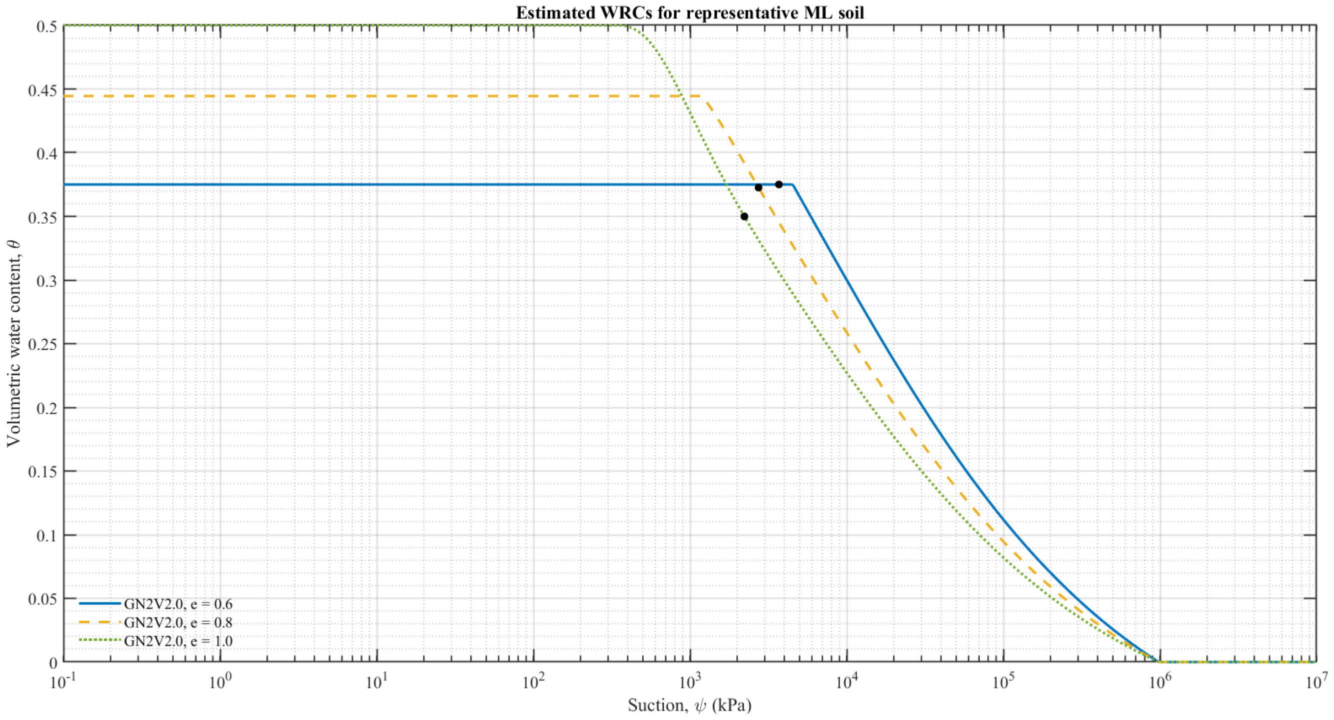

Figure 4.5 Estimated WRC (θ–ψ) for the representative ML soil (GN2V2.0) using the Aubertin-based approach, for e = 0.6, 0.8, and 1.0.

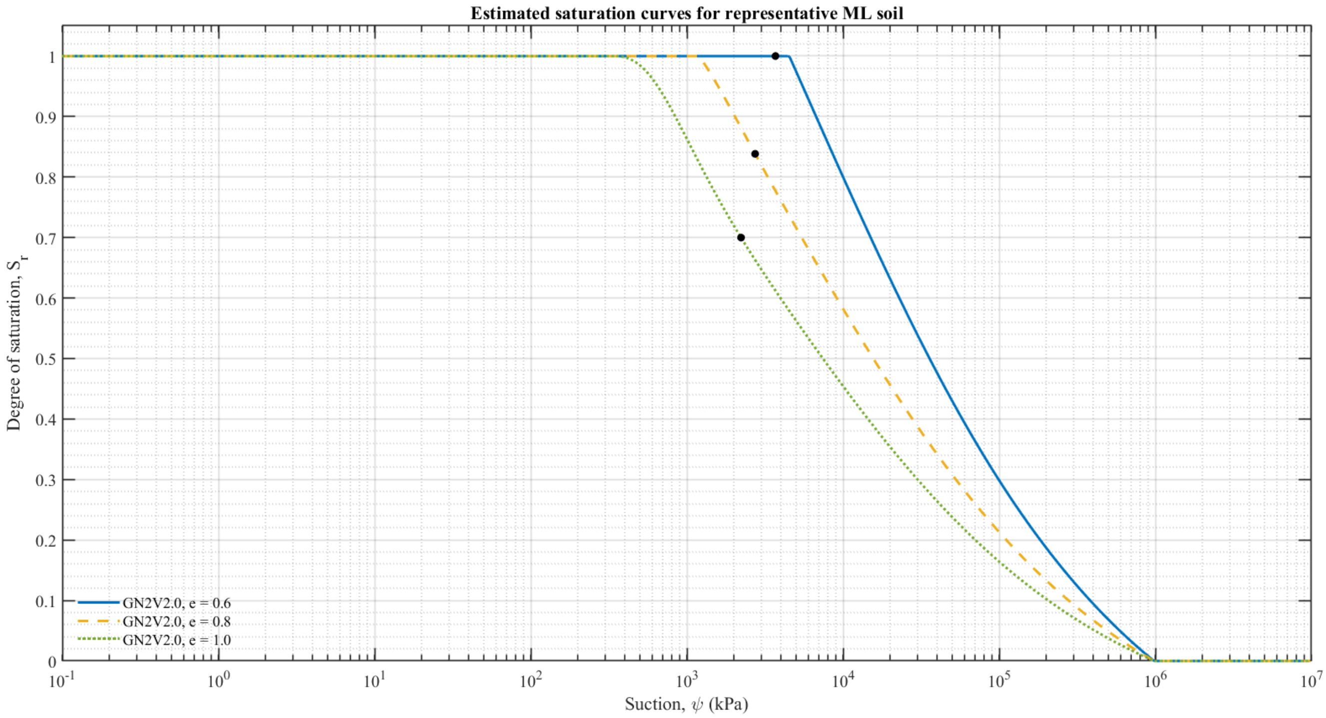

Figure 4.6 Estimated saturation curves (Sr–ψ) for the representative ML soil (GN2V2.0) using the Aubertin-based approach, for e = 0.6, 0.8, and 1.0.

The results for the representative ML soil (GN2V2.0) highlight a markedly different retention behaviour compared to the non-plastic soils. As shown in Figure 4.5 and 4.6, the curves remain close to full saturation over a wide suction range, indicating a delayed desaturation process. This behaviour is typical of fine-grained soils, where smaller pore sizes generate higher capillary forces, allowing the soil to retain water at significantly higher suction levels. Once the air-entry suction is reached, a relatively sharp decrease in both volumetric water content and degree of saturation is observed, followed by a gradual transition toward the residual state at higher suction values. The influence of the assumed void ratio is also evident, with higher void ratios leading to lower water retention and earlier desaturation. However, despite this sensitivity, the overall shape of the curves remains consistent, confirming that the ML soil exhibits stronger retention capacity and a more pronounced delayed desaturation compared to the coarser, non-plastic samples.

4.7.5 Interpretation and limitations

The estimated WRCs provide a first hydraulic interpretation of the representative San Giorgio soils and complement the grain-size and plasticity characterization developed in Sections 4.4–4.6. In particular, they support the general interpretation that the investigated materials behave as silty to sandy-silty soils with relatively limited plasticity and a retention response consistent with this material type (Aubertin et al., 2003).

At the same time, several limitations must be stated clearly. First, the curves presented here were **not obtained from direct laboratory suction-controlled tests**, but from a predictive framework based on basic geotechnical properties. Second, the **void ratio had to be assumed**, and the sensitivity analysis was therefore necessary to define a plausible range of responses. Third, some model-shape parameters were fixed using literature-based representative values and should be regarded as preliminary assumptions. For these reasons, the curves should be interpreted as **estimated hydraulic trends** suitable for Chapter 4 material characterization, while the direct field-based retention behaviour derived from monitoring data is more appropriately discussed in a later chapter.

Reference note. The theoretical background for soil-water characteristic curves follows the framework presented in Fredlund, Rahardjo, and Fredlund, Unsaturated Soil Mechanics in Engineering Practice, Chapter 5. The qualitative comparison with retention behaviour predicted from basic geotechnical properties refers to Aubertin et al. (2003), A model to predict the water retention curve from basic geotechnical properties.

Chapter 5 Sensor data and QC methodology

This chapter describes the monitoring dataset and the quality-control (QC) workflow adopted to evaluate sensor reliability before any seasonal analysis or physical interpretation. The QC procedure is designed to: (i) identify non-physical measurements and instrumental artifacts, (ii) document anomalies in a traceable way, and (iii) produce cleaned time series suitable for statistical aggregation and interpretation.

5.1 Dataset description and preprocessing

The monitoring dataset consists of time series acquired at the San Giorgio levee station and includes measurements of (i) soil suction/tension recorded by tensiometers and (ii) volumetric water content recorded by FDR humidity sensors. The analyses presented in this thesis focus on the period April 2024 to May 2025, during which the monitoring network provides sufficient coverage to evaluate sensor behaviour and seasonal variability.

Sensors are installed at multiple depths (0.5, 1.0, 1.5, 2.5 and 4.0 m), allowing comparison of temporal response as a function of depth. The dataset includes both continuous segments and intervals with missing or abnormal values due to instrumental disturbances or sensor malfunction. Therefore, a structured QC procedure was applied prior to any seasonal aggregation or interpretation.

5.1.1 Monitoring network and sensor identification

Sensor IDs encode the station (e.g., GP2, GP5, GP8), the measured variable (T for tension/suction, H for horizontal humidity probe, V for vertical humidity probe), and the installation depth (e.g., 0.5, 1.0, 1.5, 2.5, 4.0 m). Throughout this thesis, sensors are referenced using this convention (e.g., GP8T0.5, GP5H4.0). This standardized naming allows direct comparison among depths and locations and supports the final performance summary table.

5.1.2 Data acquisition, time resolution, and completeness

Time series were acquired automatically by the monitoring system and stored as timestamped records. Prior to QC screening, the raw files were checked for duplicated timestamps, inconsistent time formats, and missing intervals. Data completeness was quantified for each sensor as the percentage of valid records within the selected monitoring period. This metric is used in Chapter 6 to distinguish sensors with short valid coverage from those with continuous and reliable behaviour.

5.2 Variables, units, and sign convention

Tensiometer measurements are expressed in kPa, while humidity sensors are expressed in % volumetric water content. Because tensiometer outputs may include offsets and may be recorded with different sign conventions depending on calibration and logger configuration, tension values are reported here exactly as recorded in the monitoring dataset. In later chapters, emphasis is placed on relative temporal changes, coherence with humidity sensors at the same depth/location, and consistency across the monitoring network, rather than on the absolute sign of individual readings.

To prevent non-physical values from influencing statistics, plausibility filters were applied. Humidity values were constrained to the range 0–100%. Tension values were constrained to a physically meaningful range (−50 to 500 kPa) consistent with sensor limitations and the monitored soil conditions.

5.2.1 Measured variables and physical meaning

Tension (T) is used as a proxy for soil water suction and reflects wetting and drying processes in the unsaturated zone. Humidity sensors (H and V) provide volumetric water content. Coherence between T and humidity at the same location/depth (e.g., wetter periods corresponding to lower suction or lower tension magnitude) is used as a consistency check during QC.

5.2.2 Plausibility ranges used for automated screening

Table 5.1 Plausibility bounds used during QC screening (values outside these bounds are flagged as invalid).

Variable	Accepted range	Rationale
Humidity (H, V)	0–100 %	Physical bounds for volumetric water content expressed in percent.
Tension (T)	-50 to 500 kPa	Range adopted to exclude clearly non-physical values and logger artifacts.

5.3 QC objectives and anomaly classification

5.3.1 Sign convention and treatment of offsets

In practice, tensiometer signals may exhibit offsets or sign changes depending on calibration and data logger configuration. For transparency and reproducibility, the thesis reports tension values as recorded. Interpretation therefore focuses on temporal patterns (seasonal cycles, event responses) and cross-sensor coherence, rather than on the absolute sign of a single series. When needed, the sign convention is clarified locally in figure captions.

The objective of the QC procedure is to evaluate the reliability of each sensor time series and to distinguish between (i) plausible physical variations of the soil–water system and (ii) instrumental artifacts or failures. QC screening combines visual inspection of the time series with rule-based identification of abnormal patterns.

- Spikes / isolated outliers: abrupt single-point peaks or drops not consistent with adjacent measurements.

- Step changes / resets: sudden jumps to a different level followed by immediate stabilization.
- Flatlines / stuck values: long intervals with nearly constant readings, especially when a response is expected during wetting/drying phases.
- Unrealistic or out-of-range behaviour: values inconsistent with the expected sensor operating range or with physically plausible soil behaviour.

Figure 5.1 provides representative examples of these anomaly types used as a reference for QC classification.

Figure 5.3 – Representative anomaly types used for QC classification

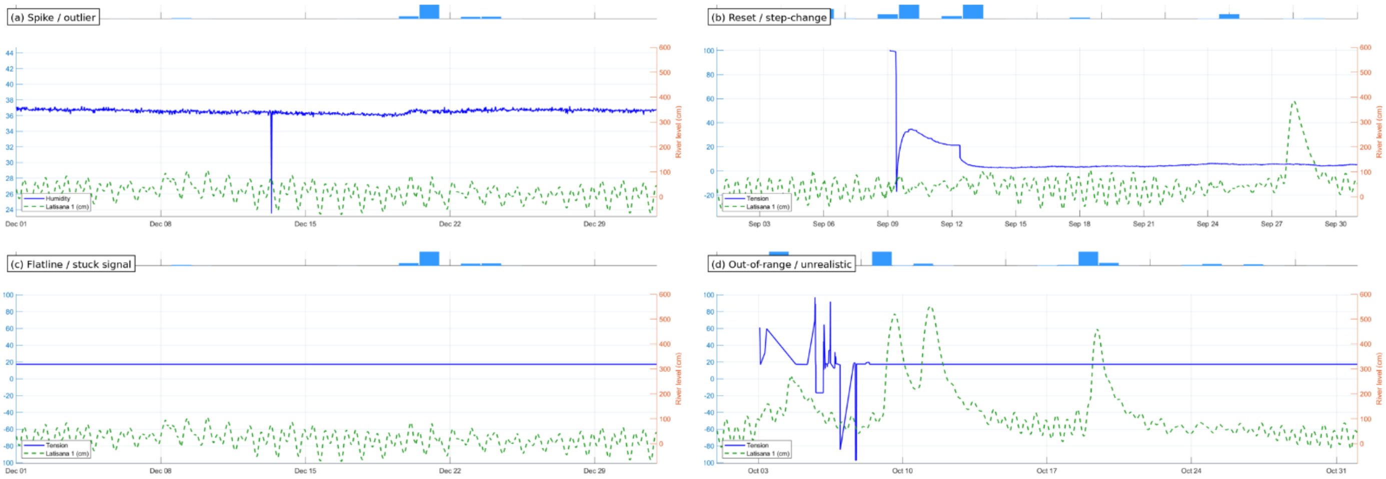

Figure 5.1 Representative anomaly types used for QC classification: (a) isolated spike/outlier, (b) reset/step-change discontinuity, (c) flatline/stuck signal (loss of response), and (d) out-of-range/unrealistic values.

Figure 5.1– Representative anomaly types used for QC classification: (a) isolated spike/outlier (GP2, 1.0 m, Humidity, Dec 2024), (b) reset/step-change discontinuity (GP8, 0.5 m, Tension, Sep 2024), (c) flatline/stuck signal indicating loss of responsiveness (GP5, 2.5 m, Tension, Dec 2024), and (d) out-of-range/unrealistic values (GP5, 2.5 m, Tension, Oct 2024; values below the adopted plausibility bound of −50 kPa). These examples were used as references for anomaly identification and subsequent exclusion (replacement with “non” / NaN) in the cleaned dataset prior to seasonal analysis.

QC decision rules. Instrumental failure is assumed when the signal becomes stuck/flat at unrealistic values and shows no response during clear hydrological forcing. In contrast, isolated spikes and short reset-like discontinuities are treated as outliers when the signal returns rapidly to a realistic range; in these cases, only the affected interval is excluded while the remaining record is retained.

5.3.2 Rule-based screening criteria

Automated screening was applied to support systematic detection across the full network. The screening criteria include: (i) out-of-range checks using the plausibility bounds in Table 5.1; (ii) detection of abrupt steps (resets) using large first differences between consecutive records; (iii) detection of spikes as isolated points that deviate strongly from local neighbourhood statistics; and (iv) identification of flatlines by evaluating the variance of a moving window over time.

5.3.3 Summary of anomaly patterns and QC actions

Table 5.2 Anomaly patterns used for QC classification and the adopted treatment.

Anomaly type	Typical signature	QC action
Spike/outlier	Single-point peak/drop; immediate return to baseline	Flag point(s) and exclude from statistics
Reset/step change	Abrupt jump to a new level; stable afterwards	Exclude affected interval; keep remaining record if coherent
Flatline/stuck	Near-constant values over long duration; no response to seasons/events	Classify as malfunction; exclude interval (often end of record)
Out-of-range	Values beyond physical sensor limits (e.g., humidity <0% or >100%)	Flag as invalid; exclude from analysis

5.4 Anomaly documentation and treatment of invalid data

5.4.1 QC workflow and reproducibility

Figure 5.2 summarizes the QC workflow adopted in this thesis. The workflow follows a traceable sequence: raw import and time alignment, plausibility checks, anomaly detection, anomaly logging, replacement of invalid values, and computation of summary statistics on cleaned series. This structure ensures that all subsequent analyses (seasonal trends and physical interpretation) are based on validated data.

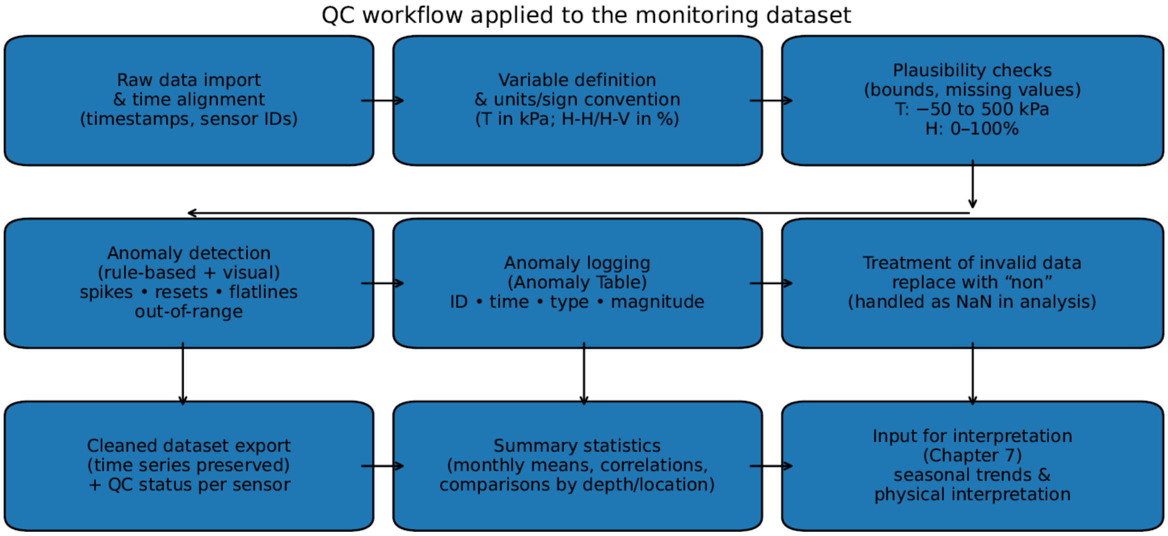

Figure 5.2 QC workflow applied to the monitoring dataset (from raw data to cleaned series and summary statistics).

To ensure traceability, all detected anomalies were recorded in a dedicated Anomaly Table including sensor ID, depth, timestamp, anomaly type (spike/reset/flatline/unrealistic) and magnitude. Key anomaly examples were additionally summarized and used as QC case studies in Chapter 6.

Anomalous values were excluded from quantitative analyses (e.g., correlation, monthly averages, curve fitting). In the corrected dataset, anomalous observations were replaced with a missing-value label (e.g., "non") to preserve time alignment while preventing biased statistics. For statistical processing, these invalid entries were treated as missing values (NaN) so that aggregated metrics were computed by averaging valid records only (i.e., omitting NaNs).

After QC screening and filtering, seasonal statistics were computed using the cleaned time series. Monthly mean series were calculated for each sensor by averaging available values only; this workflow ensures that seasonal interpretation reflects hydrologic behaviour rather than instrumental artifacts.

5.4.2 Handling of missing data and replacement strategy

Missing records (gaps) are distinguished from invalid records (anomalies). Gaps arise from data acquisition interruptions and are kept as missing values. Invalid records are identified by QC screening and replaced with a missing-value label ("non") in the corrected file to preserve the original time axis. For all computations (e.g., monthly means), both gaps and replaced anomalies are treated as NaN so that aggregated statistics are computed from valid observations only.

5.4.3 Software environment and implementation notes

QC processing was implemented using scripted routines to ensure repeatability. The workflow includes automated parsing of raw files, generation of time-series plots for visual checks, creation of the anomaly table, and export of corrected datasets. All processing steps are designed so that updates (e.g., new data releases or revised thresholds) can be incorporated by re-running the scripts.

5.5 Sensor evaluation criteria (classification)

Based on the QC screening outcomes, each sensor was assigned to one of the following categories:

- Reliable (normal sensor): consistent time series with expected wetting–drying patterns and limited anomalies.
- Partially reliable: generally coherent behaviour but recurrent spikes, gaps, or short flatline episodes that reduce continuity.
- Unreliable: dominated by persistent spikes, stuck values, or unrealistic readings; only an initial valid period may be retained, and field inspection/replacement is recommended.

This classification supports the network-wide summary table presented in Chapter 6, which reports the QC status and usable periods for all sensors (T, H-H and H-V) across the monitoring network.

5.5.1 Practical criteria used to assign QC status

In addition to qualitative assessment, the classification considers: (i) length of continuous valid coverage within the study period, (ii) frequency and persistence of anomalies, and (iii) coherence with neighbouring sensors at similar depth. A sensor is considered reliable when it shows stable seasonal behaviour with limited anomalies; partially reliable when valid behaviour is present but interrupted by recurrent artifacts; and unreliable when the record is dominated by malfunctions (e.g., persistent flatline or pervasive out-of-range values).

5.6 Limitations and link to subsequent chapters

This chapter defines the QC framework and the criteria used to evaluate sensor performance. Chapter 6 applies these criteria to all sensors and presents the final network-wide performance summary table. Chapter 7 uses only the cleaned and validated time series to analyse seasonal trends and to develop a physical interpretation supported by sensor location and stratigraphy information.

Chapter 6 Sensor Performance Evaluation Results

This chapter presents the outcomes of the quality control (QC) procedure described in Chapter 5, with the goal of assessing the reliability of each monitoring sensor and defining the time windows that can be safely used for seasonal analysis and physical interpretation in Chapter 7. The evaluation is based primarily on the occurrence of anomalous patterns (isolated spikes/outliers, step-change discontinuities/resets, flatline/stuck signals, and out-of-range/unrealistic values), supported by expert visual inspection and cross-sensor coherence checks.

6.1 Overview of QC outcomes

Across the monitoring period (April 2024 to May 2025), sensor records exhibit a combination of physically plausible seasonal variability and non-physical artifacts attributable to instrumental issues. The most recurrent QC issues observed in the dataset can be grouped into the four anomaly classes introduced in Chapter 5 (see Figure 5.3). In practice, spikes typically affect short time windows, while step-change events and flatlines may define longer invalid intervals requiring segmentation or exclusion.

- Spikes/outliers: isolated peaks or drops, removed locally while retaining the remaining coherent record.
- Resets/step changes: discontinuities treated by excluding a transition window and, when appropriate, analysing pre- and post-reset segments separately.
- Flatlines/stuck signals: prolonged loss of response treated as invalid for the affected interval (often leading to partial usability).
- Out-of-range values: records outside the adopted plausibility bounds (Chapter 5), excluded from analysis.

6.2 QC evidence and representative examples

To support the network-wide classification, a limited set of representative time-series excerpts is reported in this chapter. The purpose of these figures is to illustrate typical behaviours corresponding to the three QC classes (Reliable, Partially reliable, Unreliable).

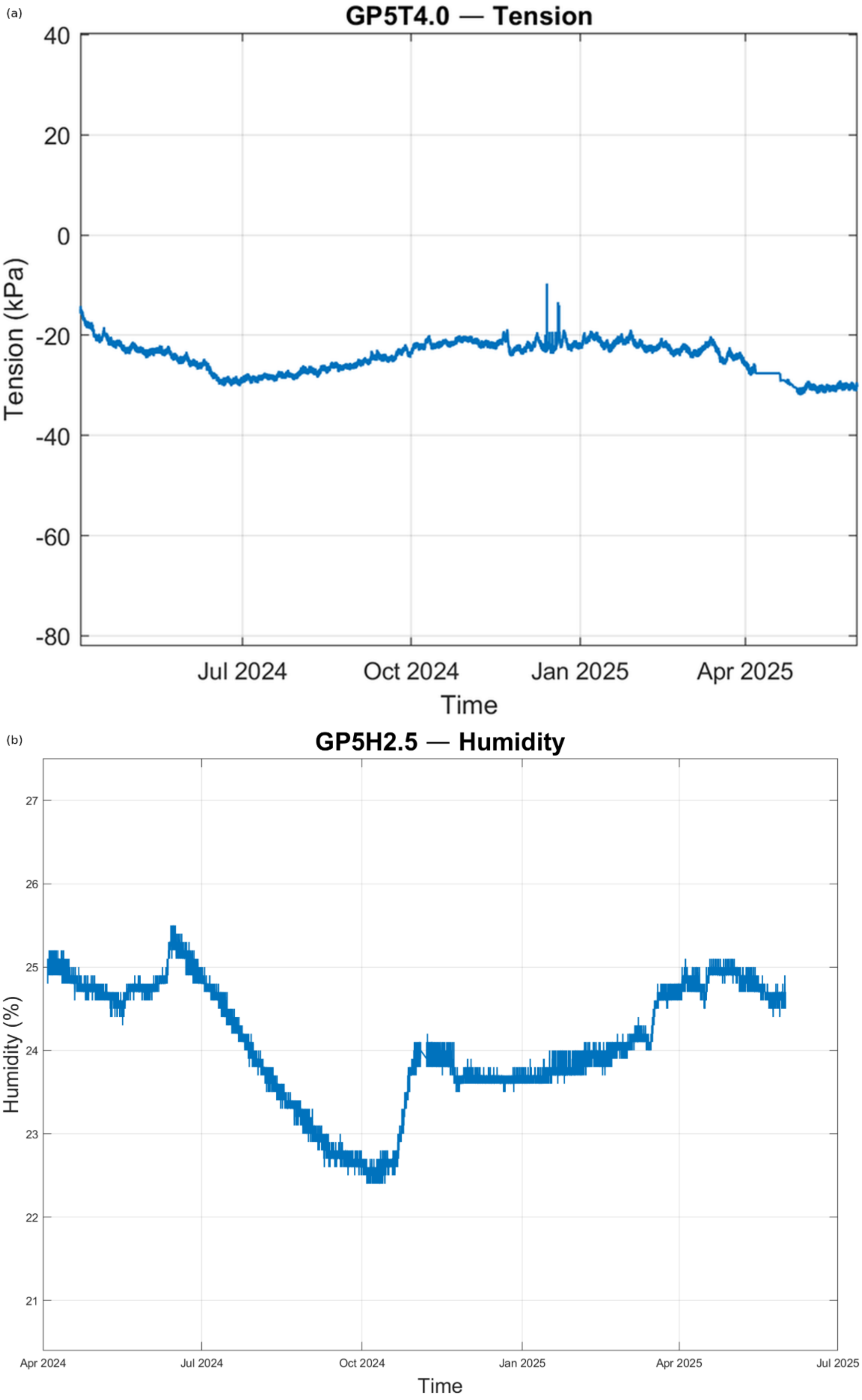

Figure 6.1 Example of a Reliable sensor record after QC screening.

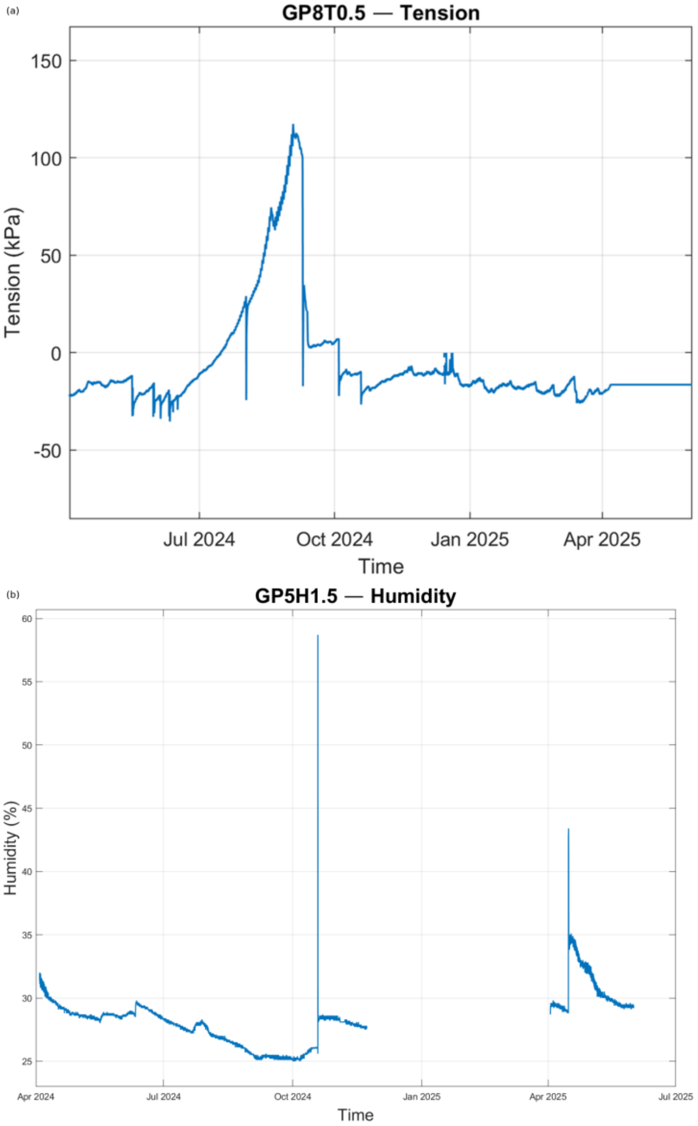

Figure 6.2 Example of a Partially reliable sensor record showing QC-treated.

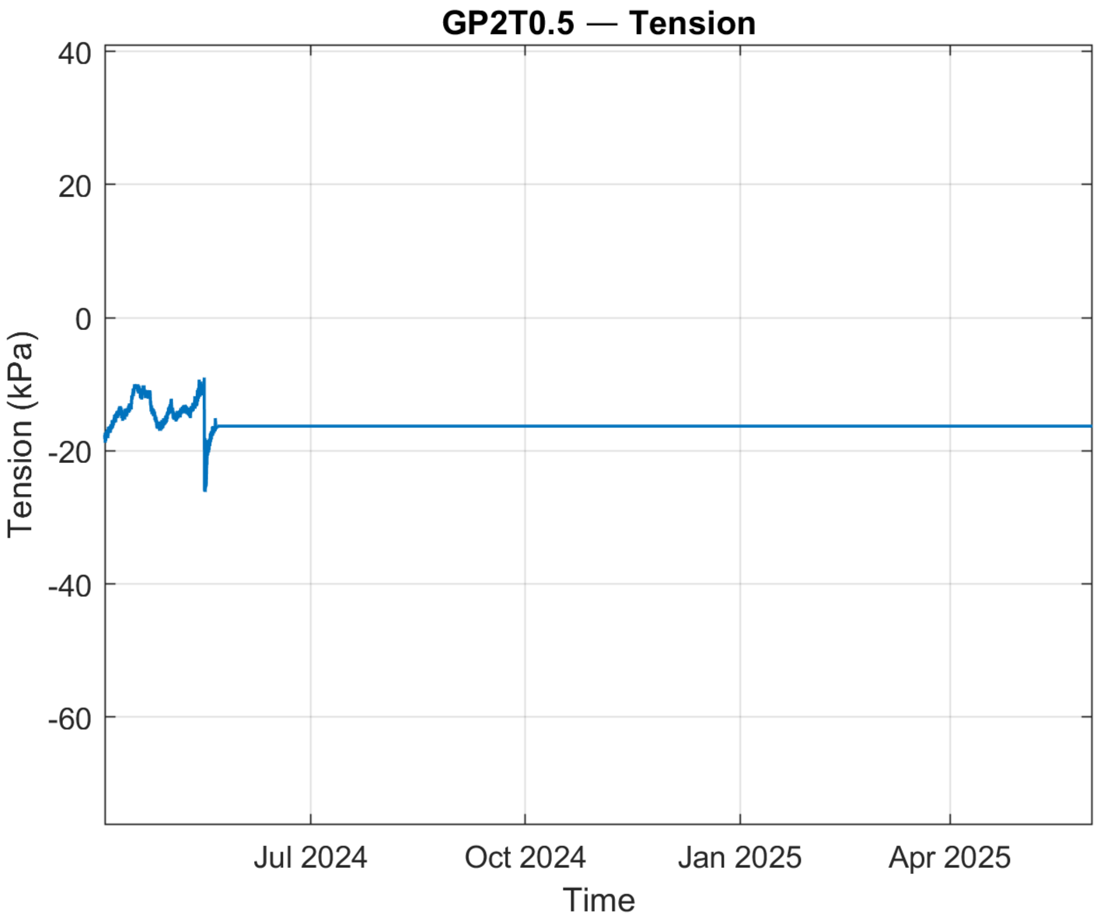

Figure 6.3 Example of an Unreliable sensor record dominated by non-physical behaviour.

6.3 Sensor-by-sensor performance assessment

Sensor performance was assessed for each variable type (Tension, Humidity-H, Humidity-V) and for each depth/location. For every sensor, the following information was documented: (i) dominant anomaly patterns, (ii) usable time windows, (iii) coherence with co-located sensors at the same depth, and (iv) the resulting QC class. When step-changes or long gaps were present, the record was divided into segments, and only stable segments were retained for seasonal statistics.

6.3.1 Tension sensors (T)

Tension time series were evaluated with particular attention to (i) out-of-range excursions relative to the adopted plausibility bounds (−50 to 500 kPa), (ii) prolonged flatlines indicating loss of responsiveness, and (iii) reset-like discontinuities. Where possible, tension behaviour was cross-checked against co-located humidity sensors to verify seasonal coherence.

6.3.2 Humidity sensors – horizontal configuration (H-H)

Humidity-H sensors were screened for spikes, step-change discontinuities, and discontinuous segments separated by long gaps. Because humidity is constrained to 0–100%, out-of-range values were rare; instead, the main limitation was the presence of resets/offsets that require segment-wise analysis.

6.3.3 Humidity sensors – vertical configuration (H-V)

Humidity-V sensors generally provide stable seasonal patterns, but some shallow sensors exhibit frequent spikes and step-like offsets. QC decisions followed the same rules as Chapter 5: isolated spikes were removed locally, while step-like offsets were handled by segmentation.

6.4 Final summary table of sensor performance

Table 6.1 summarises the QC classification for all monitoring sensors considered in this thesis, including the dominant issues and the recommended usable periods. Completeness metrics (schedule-based and grid-based) can be appended as supporting information if needed; however, the QC class reported here is assigned primarily based on anomaly patterns and expert inspection, consistent with the methodology in Chapter 5.

Table 6.1 Summary of QC performance evaluation for the monitoring sensors (T, Humidity-H, Humidity-V).

Sensor ID	**Type**	**Depth (m)**	**QC status**	**Main issues**	**Usable period (after QC)**	**Notes / action**
GP2T0.5	T	0.5	Unreliable	Persistent flatline for months (no response).	Excluded (no reliable period identified).	Recommend field check / replacement.
GP2T1.0	T	1.0	Partially reliable	Large spike/outlier episodes.	Usable excluding spike windows.	Keep; remove spikes before seasonal stats.
GP2T1.5	T	1.5	Partially reliable	Reset/step-change discontinuity.	Usable as separate segments; exclude reset window.	Segment time series around reset.
GP5T1.5	T	1.5	Partially reliable	Extreme spikes and reset-like shift.	Usable excluding spike window; segment around shift.	Cross-check with co-located humidity.
GP5T2.5	T	2.5	Partially reliable	Extreme spikes followed by long flatline.	Mainly usable before onset of flatline; exclude	Valid window is limited; treat later

					spike/flatline periods.	period as invalid.
GP5T4.0	T	4.0	Reliable	Overall stable physical trend.	Usable for full period after QC screening.	Reference sensor for deeper response.
GP8T0.5	T	0.5	Partially reliable	Reset event and later flatline.	Usable until flatline; segment around reset.	Exclude flatline interval from analysis.
GP8T1.0	T	1.0	Partially reliable	Reset and spike/outlier episodes.	Usable excluding spikes; segment around reset.	Remove spikes; keep coherent segments.
GP2H1.0	H-H	1.0	Reliable	Isolated spike/outlier.	Usable excluding spike window.	Keep; remove local outlier.
GP2H2.0	H-H	2.0	Partially reliable	Step-change/reset.	Usable as separate segments; exclude reset window.	Segment around step-change.
GP2H3.5	H-H	3.5	Reliable	Overall stable; minor reset not limiting.	Usable for full period after QC screening.	
GP5H1.5	H-H	1.5	Partially reliable	Major spikes and long data gap.	Usable segment-by-segment; exclude spike windows.	Treat each continuous segment separately.
GP5H2.5	H-H	2.5	Reliable	Stable record.	Usable for full period after QC screening.	
GP5H4.0	H-H	4.0	Partially reliable	Two segments separated by long gap/offset.	Usable as two separate segments (not continuous).	Avoid treating as continuous trend.
GP7H1.0	H-H	1.0	Reliable	Stable record.	Usable for full period after QC screening.	
GP8H0.5	H-H	0.5	Partially reliable	Multiple resets/breaks.	Usable only in stable segments.	Select stable segments for seasonal stats.
GP8H1.0	H-H	1.0	Partially reliable	Repeated reset-like events.	Usable only in limited stable segments.	Use cautiously; document segments.
GP9H1.0	H-H	1.0	Partially reliable	Repeated reset/spikes.	Usable only in limited stable segments.	Remove spikes; segment analysis.

GP3V0.5	H-V	0.5	Partially reliable	Frequent spikes/outliers.	Usable after removing spikes.	Apply outlier filtering before averaging.
GP3V1.0	H-V	1.0	Partially reliable	Few spikes and a step-like change.	Usable excluding spikes; segment around step.	
GP3V1.5	H-V	1.5	Reliable	Stable trend.	Usable for full period after QC screening.	
GP3V2.0	H-V	2.0	Reliable	Stable; minor events.	Usable for full period after QC screening.	
GP4V0.5	H-V	0.5	Partially reliable	Spikes and step-like change.	Usable segment-by-segment; clean spikes.	
GP4V1.0	H-V	1.0	Reliable	Overall stable; isolated spikes.	Usable excluding spike windows.	
GP4V1.5	H-V	1.5	Reliable	Stable record.	Usable for full period after QC screening.	
GP4V2.0	H-V	2.0	Reliable	Stable record.	Usable for full period after QC screening.	
GP6V0.5	H-V	0.5	Partially reliable	Many spikes/outliers.	Usable after cleaning spikes.	
GP6V1.0	H-V	1.0	Reliable	Sufficiently stable; minor events.	Usable for full period after QC screening.	
GP6V1.5	H-V	1.5	Reliable	Stable record.	Usable for full period after QC screening.	
GP6V2.0	H-V	2.0	Reliable	Stable record.	Usable for full period after QC screening.	

Note: “Usable period” is expressed qualitatively in this draft. When finalising the thesis, these windows should be replaced with explicit date ranges consistent with the study period and the anomaly log (e.g., “Apr 2024–Sep 2024 usable; Oct 2024–May 2025 excluded due to flatline”).

6.5 Implications for seasonal analysis and limitations

The QC classification presented in this chapter defines the sensor subset and time windows used for seasonal aggregation and interpretation in Chapter 7. Reliable sensors and stable segments of partially reliable sensors are used to compute monthly means and to compare depth-dependent responses. Conversely, intervals affected by resets, flatlines, or out-of-range behaviour are excluded to prevent instrumental artifacts from biasing seasonal metrics.

At the current stage, the performance evaluation is primarily time-series based. The physical interpretation of observed seasonal patterns will be strengthened by integrating precise sensor positions and stratigraphic information.

Chapter 7 Seasonal trends and physical interpretation

This chapter analyses the seasonal evolution of the monitored variables (tension and volumetric water content) at the San Giorgio levee station over the study period (Apr 2024–May 2025), using only the validated portions of the dataset obtained after the quality-control (QC) workflow (Chapter 5) and the sensor performance screening and classification (Chapter 6). The objective is to (i) extract robust seasonal signatures (drying/rewetting cycles), (ii) compare responses across depths and locations, and (iii) provide a first physical interpretation consistent with unsaturated-zone processes in levee materials. A second objective is to exploit co-located sensor pairs (tension and humidity at the same depth and location) to evaluate coherence and to explore an empirical water-retention relationship using the van Genuchten model, supporting the interpretation of suction–moisture coupling.

7.1 Chapter objectives and workflow

The workflow adopted in this chapter follows three consecutive steps:

- Selection of sensors and time windows based on the QC status (Reliable sensors and stable segments of Partially reliable sensors).
- Seasonal aggregation of the cleaned time series into monthly statistics to highlight long-term behaviour and suppress high-frequency noise.

Interpretation of seasonal patterns considering depth-dependent damping, local boundary conditions, and consistency between variables.

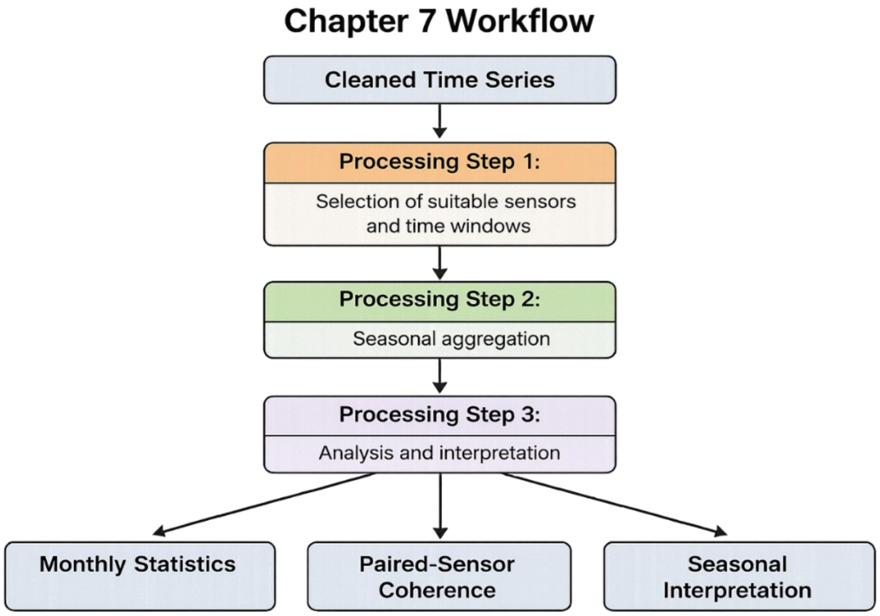

Figure 7.1 summarises the Chapter 7 analysis workflow.

7.2 Input data and sensor subset used for seasonal analysis

The monitoring network includes tensiometers (T) and FDR humidity probes installed in both horizontal configuration (Humidity-H) and vertical arrays (Humidity-V) at multiple locations (e.g., GP2, GP5, GP8) and depths (0.5–4.0 m). As documented in Chapter 5, tension values are reported using the sign convention provided by the logger; therefore, interpretation emphasises relative temporal changes and cross-sensor coherence rather than absolute sign. In this chapter, records affected by spikes, resets, flatlines, or out-of-range behaviour were excluded by treating flagged values as missing and computing statistics on valid observations only (omit NaN).

The final sensor subset used here is defined as:

- Reliable sensors: used over their full monitoring period after QC screening.
- Partially reliable sensors: used only within stable segments; segmentation windows are reported and respected in aggregation.
- Unreliable sensors: excluded from seasonal statistics and interpretation (unless a short clearly valid initial window exists and is explicitly stated).

Table 7.1 Sensor pairs used in Chapter 7 and adopted usable time windows.

Location	**Depth (m)**	**Tension sensor**	**Humidity sensor**	**QC class (Ch.6)**	**Adopted usable time window**
GP2	1.0	GP2T1.0	GP2H1.0	T: Partially reliable (spike) / H: Reliable (isolated spike)	Use full record except exclude identified spike/outlier windows; segment if needed.
GP5	1.5	GP5T1.5	GP5H1.5	T: Partially reliable (spikes + reset-like shift) / H: Partially reliable (spikes + gap)	Use stable segments only; exclude spike windows; treat pre/post gap separately.
GP5	2.5	GP5T2.5	GP5H2.5	T: Partially reliable (extreme spikes + long flatline) / H: Reliable	Prefer the pre-event segment before long flatline; exclude spike window; use H full record.
GP5	4.0	GP5T4.0	GP5H4.0	T: Reliable / H: Partially reliable (two segments with gap/offset)	Use T full record; use H segment-by-segment (treat offset/gap as discontinuity).
GP8	0.5	GP8T0.5	GP8H0.5	T: Partially reliable (reset + later flatline) / H: Partially reliable (multiple resets)	Use up to onset of flatline; exclude reset/spike windows; use stable segments only.
GP8	1.0	GP8T1.0	GP8H1.0	T: Partially reliable (reset + spike) / H: Partially reliable (repeated reset-like events)	Exclude spikes; segment around reset-like events; retain only stable periods.

7.2.1 Environmental forcing variables for seasonal interpretation

The seasonal interpretation of the sensor responses was supported by two environmental forcing variables: **rainfall** measured at the San Giorgio monitoring site and **hydrometric level** of the Tagliamento River retrieved from public records (Latisana 1 station). These variables were included to interpret whether observed changes in tension and volumetric water content were consistent with site-scale hydro-climatic conditions.

Rainfall data were obtained from the local monitoring logger at San Giorgio (same monitoring system used for the sensor network), while river stage data were obtained from the publicly available hydrometric record for **Tagliamento – Latisana 1**. For consistency with the monthly sensor statistics adopted in this chapter, the forcing variables were aggregated at the **monthly scale** over the study period (**Apr 2024–May 2025**): (i) **monthly cumulative rainfall** (mm/month), and (ii) **monthly hydrometric level statistics** (monthly mean and monthly maximum, cm).

This monthly aggregation provides a common temporal scale for comparing environmental forcing with the QC-cleaned sensor responses. In particular, rainfall supports the interpretation of seasonal wetting/drying, while hydrometric level provides additional information on boundary conditions related to river stage fluctuations and event-driven hydraulic forcing.

The forcing time series indicate a **drier summer phase (lower rainfall and generally lower river level conditions)**, followed by a **transition in autumn 2024** characterized by increased rainfall and higher river-stage activity, and then a **wetter/cool-season period** with recurrent rainfall and intermittent hydrometric peaks. These patterns are used in the following sections to interpret the timing, amplitude, and depth-dependent damping observed in the sensor data.

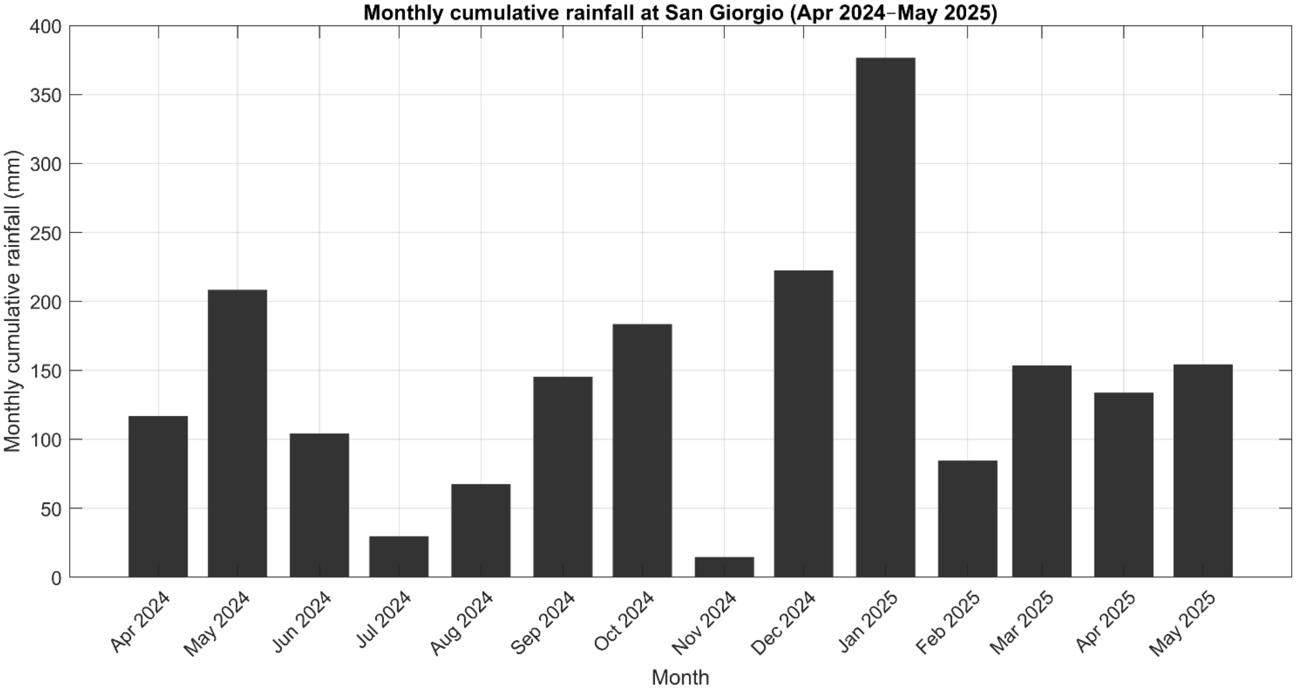

Figure 7.2 Monthly cumulative rainfall at San Giorgio for the study period (Apr 2024–May 2025).

The monthly rainfall series (**Figure 7.2**) shows clear temporal variability over the study period, with relatively drier summer conditions (especially July–August 2024), followed by a wetter and more variable cool-season period from autumn 2024 onward, including major rainfall peaks in December 2024 and January 2025. This pattern is consistent with the expected transition from seasonal drying to autumn–winter rewetting.

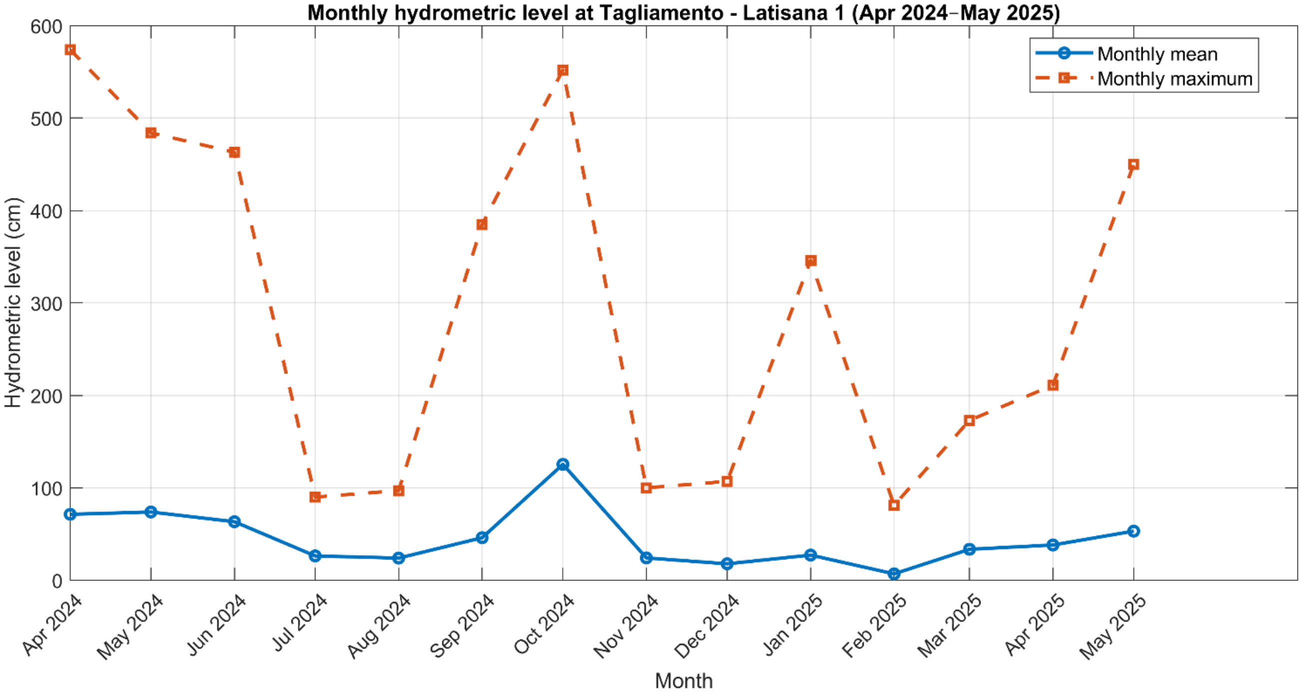

Figure 7.3 Monthly hydrometric level at Tagliamento–Latisana 1 (mean and maximum) for the study period (Apr 2024–May 2025).

The monthly hydrometric series at Latisana 1 (**Figure 7.3**) provides an additional boundary-condition indicator for interpreting levee response. The comparison between monthly mean and monthly maximum levels highlights marked intra-month river-stage variability, including short-duration peak events that may affect near-river hydraulic conditions even when monthly average stage remains moderate. These forcing trends are used in the following sections to interpret the timing, magnitude, and depth-dependent damping of the observed tension and humidity responses.

7.3 Seasonal aggregation and statistical metrics

To extract seasonal behaviour and allow comparison among sensors, the cleaned time series were aggregated into monthly statistics. Monthly mean values were computed for each sensor by averaging only valid records within each calendar month (invalid/anomalous values replaced by "non"/NaN are omitted). This approach reduces the influence of high-frequency fluctuations, facilitates depth/location comparisons, and highlights sensor-specific deviations such as drift or offset changes.

The following metrics are recommended (and can be reported in tables/figures as needed):

- Monthly mean and monthly median (robust central tendency).
- Monthly standard deviation and interquartile range (variability).
- Valid data coverage per month (% valid records) to document the reliability of each monthly estimate.
- Seasonal amplitude (max–min of monthly means) as a simple measure of depth-dependent damping.

When a sensor is segmented due to resets or discontinuities, monthly statistics are computed separately for each stable segment, and continuity across segments is not assumed.

7.4 Network-wide seasonal patterns

The network-wide seasonal evolution observed after QC cleaning is consistent with the environmental forcing data (monthly rainfall and Tagliamento hydrometric level). A drier phase is observed during late spring–summer 2024 (lower rainfall and lower river-stage conditions), followed by a rewetting transition from autumn 2024 onward, when rainfall increases and hydrometric activity becomes more pronounced. The monthly aggregation enables direct comparison between forcing and sensor responses while reducing high-frequency noise.

7.4.1 Tension sensors (T): monthly mean evolution

Monthly mean tension values show clear seasonal behavior across the selected tensiometers (Fig. 7.4 to Fig 7.6). A pronounced summer–early autumn excursion is visible for several shallow sensors, followed by a regime change around October 2024, consistent with the transition from dry to wetter conditions. Because the absolute sign of tension can be affected by sensor convention and installation offset, the interpretation here focuses on **relative changes over time** (increase/decrease) and on coherence with co-located humidity sensors.

The timing of the main regime shift around **Sep–Oct 2024** is consistent with the increase in monthly rainfall and the corresponding rise in river-stage variability, supporting a physical interpretation (rewetting and reduced suction) rather than purely sensor-specific drift.

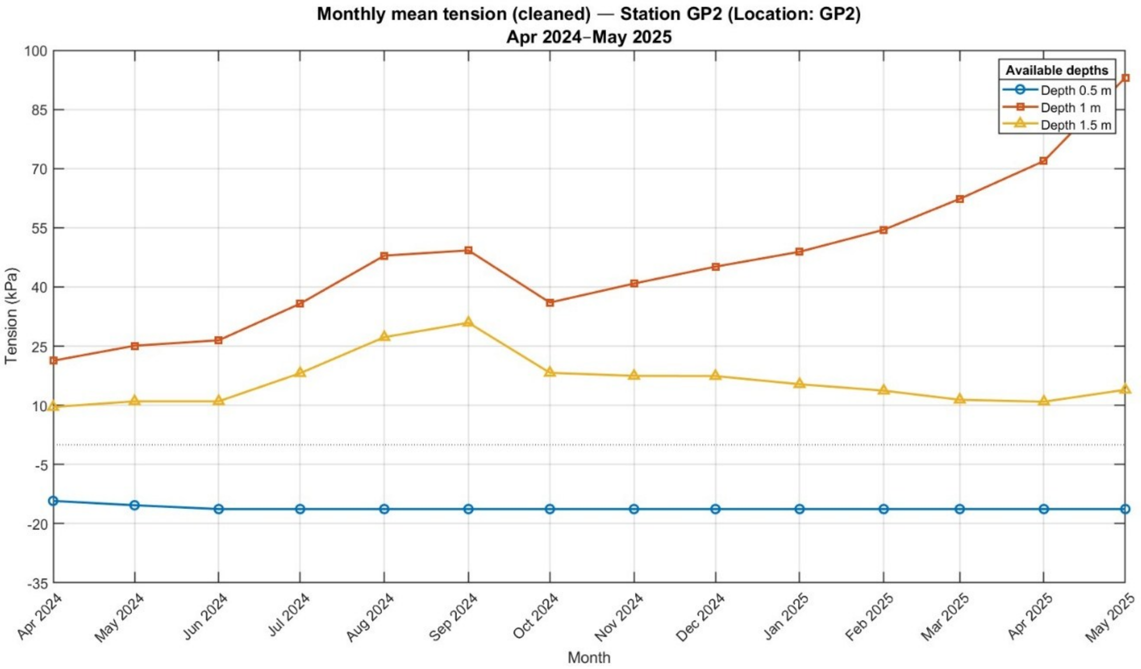

Figure 7.4 Monthly mean tension at GP2 (cleaned data) by depth for Apr 2024–May 2025

At **GP2**, the monthly mean tension shows a clear seasonal drying–rewetting signal, with the strongest response at **1.0 m depth** (GP2T1.0), which increases progressively from spring to late summer and reaches its highest values by spring 2025. This pattern is consistent with the forcing series in **Figure 7.2** and **Figure 7.3:** lower rainfall and generally lower river levels during late spring–summer 2024 correspond to increasing suction (drying), while wetter autumn–winter conditions lead to a temporary reduction/stabilisation in tension before a renewed increase. The **1.5 m sensor** (GP2T1.5) follows the same seasonal tendency but with lower amplitude, indicating depth damping. In contrast, the **0.5 m sensor** remains nearly constant and negative, which is not consistent with the stronger seasonal variation observed at the co-located deeper sensors and with the rainfall/river forcing; this likely reflects that this sensor is un reliable at all as indicated at Ch.6 , so interpretation at GP2 should rely mainly on the 1.0 m and 1.5 m signals.

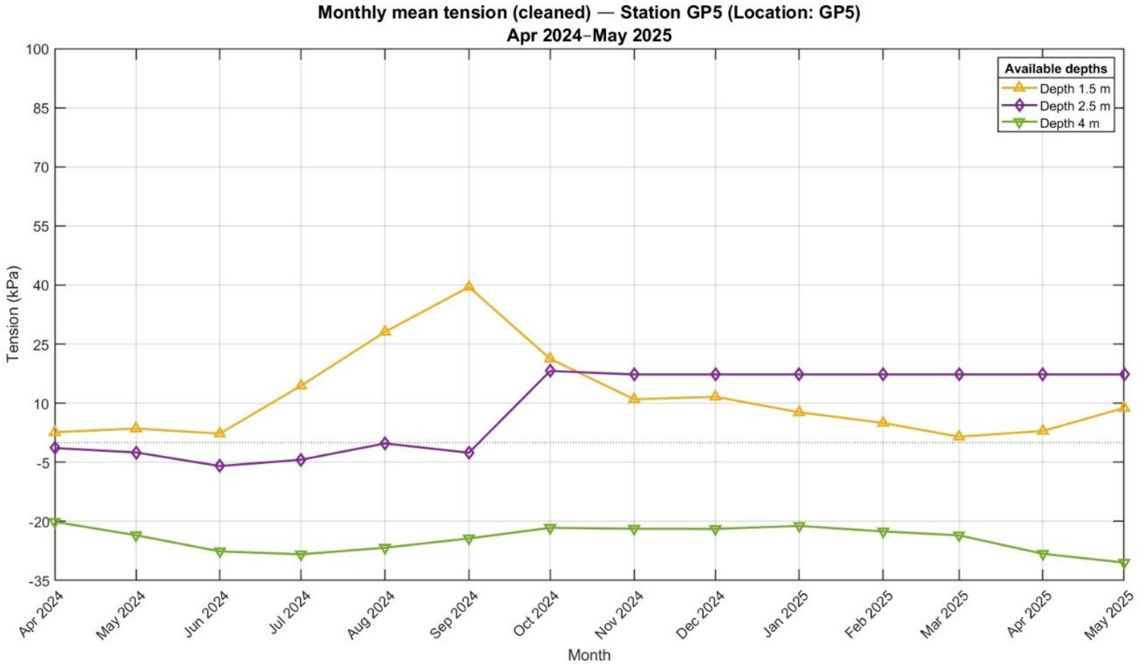

Figure 7.5 Monthly mean tension at GP5 (cleaned data) by depth for Apr 2024–May 2025.

At **GP5**, the three depths show a more heterogeneous response, but the overall evolution still reflects seasonal hydro-climatic forcing. The **1.5 m sensor** (GP5T1.5) shows a marked increase in tension from spring to late summer 2024 (drying phase), followed by a decrease during autumn–winter, which is consistent with the increase in monthly rainfall (**Figure 7.2**) and the occurrence of river-level peaks (**Figure 7.3**). The **4.0 m sensor** (GP5T4.0) remains persistently negative with relatively small seasonal variation, suggesting a deeper layer with weaker atmospheric influence and stronger damping. The **2.5 m sensor** (GP5T2.5) exhibits an abrupt upward shift around early autumn and then becomes nearly flat, which does not match the smoother seasonal pattern expected from rainfall and river forcing; this behaviour is more consistent with a reset/offset or sensor artefact identified during QC rather than a purely physical change. Therefore, at GP5 the physically meaningful seasonal interpretation is best supported by GP5T1.5 (and partially GP5T4.0), while GP5T2.5 should be treated cautiously.

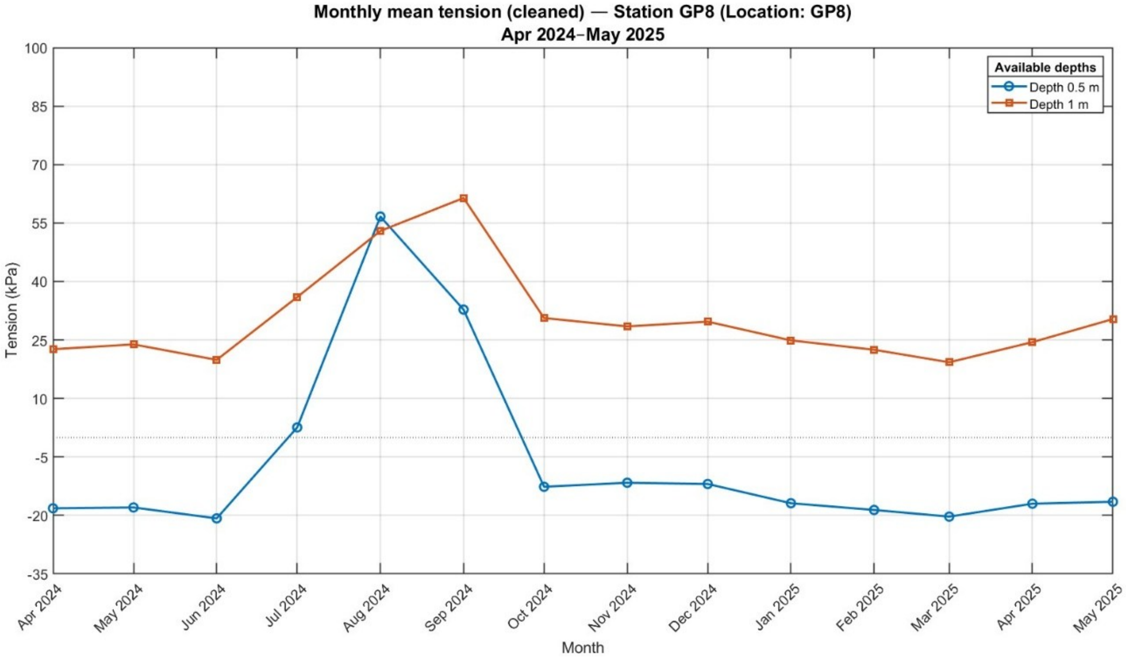

Figure 7.6 Monthly mean tension at GP8 (cleaned data) by depth for Apr 2024–May 2025.

At **GP8**, the **1.0 m sensor** (GP8T1.0) shows a coherent seasonal pattern, with increasing tension from spring to late summer 2024 (drying under lower rainfall), followed by lower or stabilised values during autumn–winter as rainfall increases and river-stage peaks become more frequent (**Figures 7.2–7.3**). This behaviour is physically consistent with suction–moisture coupling in the unsaturated zone. The **0.5 m sensor** (GP8T0.5), however, displays a pronounced summer peak and a sharp drop between September and October, after which it stabilises at lower values; the timing partly overlaps with the transition to wetter conditions, but the abruptness of the change suggests a combination of real shallow-layer response and sensor discontinuity/reset (as already highlighted in the QC stage). Overall, GP8 confirms the expected seasonal evolution (summer drying, autumn–winter rewetting), with the 1.0 m sensor providing the most robust interpretation and the 0.5 m sensor requiring segmented interpretation due to likely instrumental effects.

To complement the station-based seasonal trend interpretation, descriptive statistics and a comparative boxplot were prepared for the cleaned tension sensors used in Chapter 7. These summaries help quantify central tendency, variability, and dispersion, and support cross-comparison among stations and depths.

Table 7.2 Descriptive statistics of cleaned tension sensors used for seasonal analysis in Chapter 7 (mean, standard deviation, minimum, maximum, and data completeness).

Sensor	**Mean (kPa)**	**Std (kPa)**	**Min (kPa)**	**Max (kPa)**	**Valid count**	**Total count**	**Missing (%)**
GP2T0.5	-16.08	1.03	-26.20	-9.00	95003	95006	0.003
GP2T1.0	48.45	19.29	4.00	230.00	94980	95006	0.027
GP2T1.5	15.88	6.03	4.40	35.70	95004	95006	0.002
GP5T4.0	-24.26	3.34	-32.00	-9.68	94951	95006	0.058
GP5T2.5	10.11	11.18	-16.70	497.00	92486	95006	2.652
GP5T1.5	10.85	10.94	-3.50	227.00	94994	95006	0.013
GP8T1.0	29.76	11.85	7.30	98.40	94992	95006	0.015
GP8T0.5	-8.13	24.13	-35.40	117.00	94867	95006	0.146

The descriptive statistics of the cleaned tension sensors (**Table 7.2**) support the seasonal patterns observed in the station-specific monthly plots. Clear depth-dependent differences are visible: deeper sensors such as **GP5T4.0** show persistently negative tension values with relatively low variability, indicating a more buffered and stable response, while shallower/intermediate sensors (e.g., **GP2T1.0**, **GP8T1.0**) show higher mean tension and larger variability, consistent with stronger sensitivity to atmospheric forcing and seasonal drying–rewetting cycles. The very low missing percentages for most sensors confirm good data coverage after QC, whereas **GP5T2.5** shows reduced completeness and an inflated maximum value, consistent with the known anomaly/spike behavior identified in the QC assessment. Therefore, the statistical indicators are interpreted together with the QC-based segmentation and the monthly trend figures, with greater emphasis on stable periods and physically coherent responses rather than isolated extreme values.

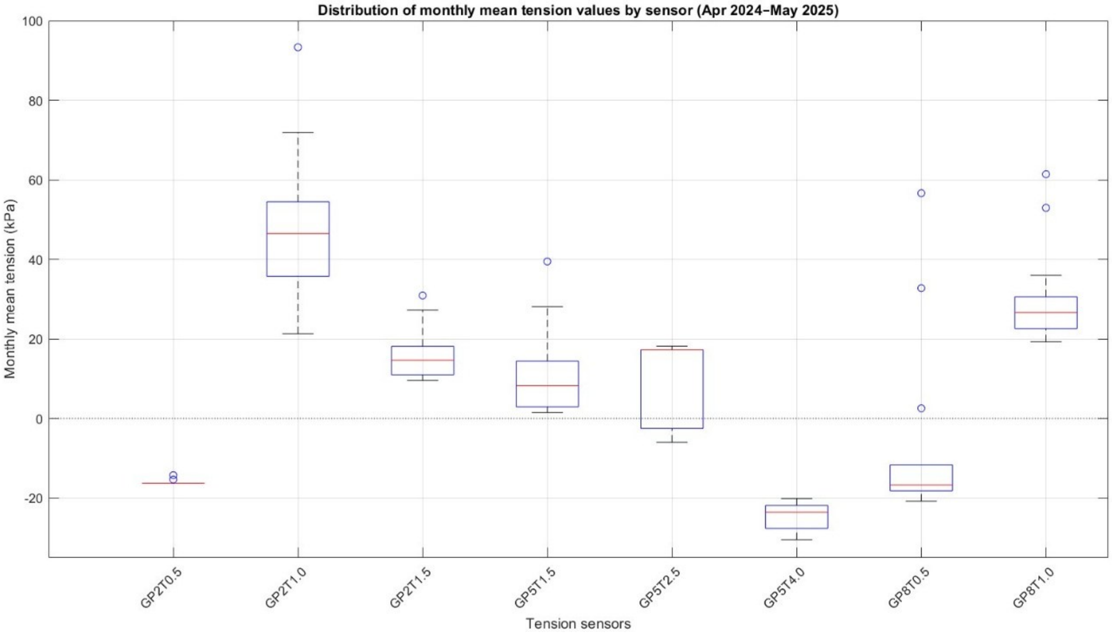

Figure 7.7 Boxplot of monthly mean tension values for the selected sensors (cleaned dataset) over the study period (Apr 2024–May 2025). The boxplots summarize the median, interquartile range, whiskers, and outlier months for each sensor.

Figure 7.7 summarizes the distribution of monthly mean tension values for the selected sensors over Apr 2024–May 2025 using boxplots. The boxplots provide a compact comparison of central tendency (median), spread (interquartile range), and extreme months (outliers) across sensors. Clear differences are observed among locations and depths: GP2T1.0 shows the highest median tension and the widest spread, indicating strong seasonal variability, while GP5T4.0 and GP2T0.5 exhibit more stable behavior with consistently negative values and relatively narrow distributions. Sensors such as GP8T0.5 and GP8T1.0 show several outlier months, reflecting episodic responses and/or segmented behavior already identified in the QC assessment. Overall, the boxplot confirms the station-based time-series interpretations and supports the influence of seasonal forcing (rainfall and river level; Figures 7.2–7.3) on the magnitude and variability of tension responses.

7.4.1.1 Seasonal depth profiles of tension

The monthly mean time-series plots presented in Figures 7.4–7.6 describe how tension evolved over time at each station. To complement that view, seasonal depth-profile plots were prepared using the signed monthly mean tension values, T, so that negative values are retained and can be interpreted explicitly. The representative periods correspond to the averages of Jul–Sep 2024, Oct–Nov 2024, and Jan–Mar 2025. These profiles provide a direct visualization of how the depth distribution of tension changes between dry, transition, and wet conditions. Because some sensors were previously classified as partially reliable or segmented in Chapter 6, the resulting profile shapes must be interpreted together with the QC assessment and with the local hydraulic context, rather than as a strict monotonic suction-with-depth trend.

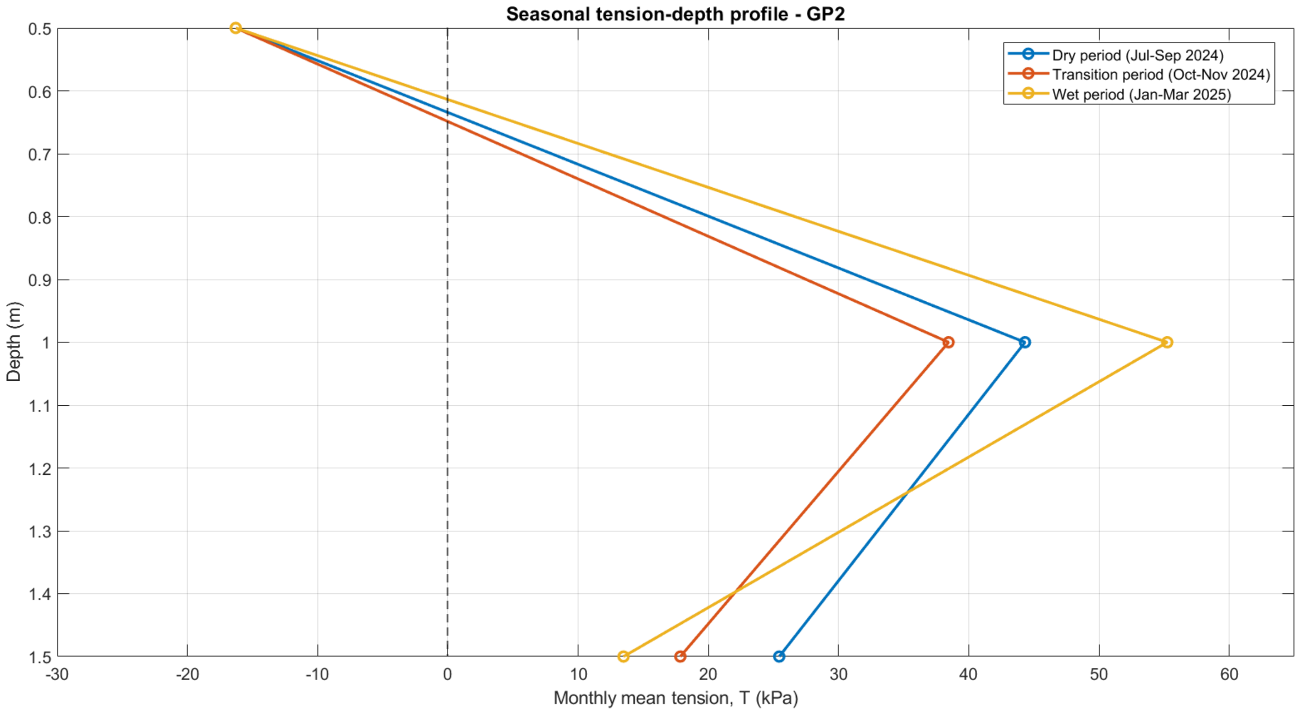

Figure 7.8 Seasonal depth profile of signed monthly mean tension, T, at station GP2 for the representative periods Jul–Sep 2024 (dry period), Oct–Nov 2024 (transition period), and Jan–Mar 2025 (wet period).

Figure 7.8 shows the seasonal depth profile of signed monthly mean tension at station GP2, where the representative periods were computed as the averages of July–September 2024 (dry period), October–November 2024 (transition period), and January–March 2025 (wet period). The profile indicates that the shallow sensor at 0.5 m remains negative in all three periods (approximately −16 kPa), which suggests persistently wetter conditions or possible proximity to near-saturated conditions in the upper shallow layer. In contrast, the strongest positive tension values occur at 1.0 m, where the seasonal mean is about 44 kPa in the dry period, decreases to about 39 kPa in the transition period, and increases further to about 55 kPa in the wet period. At 1.5 m, the seasonal mean remains positive but lower than at 1.0 m, at approximately 25 kPa in the dry period, 18 kPa in the transition period, and 13 kPa in the wet period.

This pattern does not show a simple monotonic increase of suction with depth. Instead, the maximum seasonal mean tension occurs at the intermediate depth of 1.0 m, while both the shallower sensor (0.5 m) and the deeper sensor (1.5 m) show lower values, with the shallowest sensor even remaining negative. Therefore, it suggests a non-monotonic local response, in which the 1.0 m level is the most hydraulically responsive layer at GP2.

From a physical point of view, this behavior may reflect the combined effects of local stratigraphic contrasts, infiltration redistribution, and sensor-specific response, rather than a simple depth-controlled suction gradient. The negative values at 0.5 m indicate that this shallow level behaves differently from the intermediate and deeper sensors, possibly because it is more directly influenced by transient wetting or locally wetter conditions. At the same time, the lower values at

1.5 m suggest a more buffered response than at 1.0 m. The fact that the wet-period mean at 1.0 m is even higher than the dry-period mean also indicates that seasonal averaging may be capturing not only direct climatic forcing, but also lagged subsurface redistribution and the influence of the specific months included in each representative period.

For this reason, the GP2 profile is best interpreted as a station where the seasonal tension response is strongest at intermediate depth, while the shallowest sensor remains close to or below zero and the deeper sensor shows a damped response. This interpretation is more consistent with the signed data and avoids the misleading impression, created by plotting absolute values, that suction simply increased downward throughout the profile.

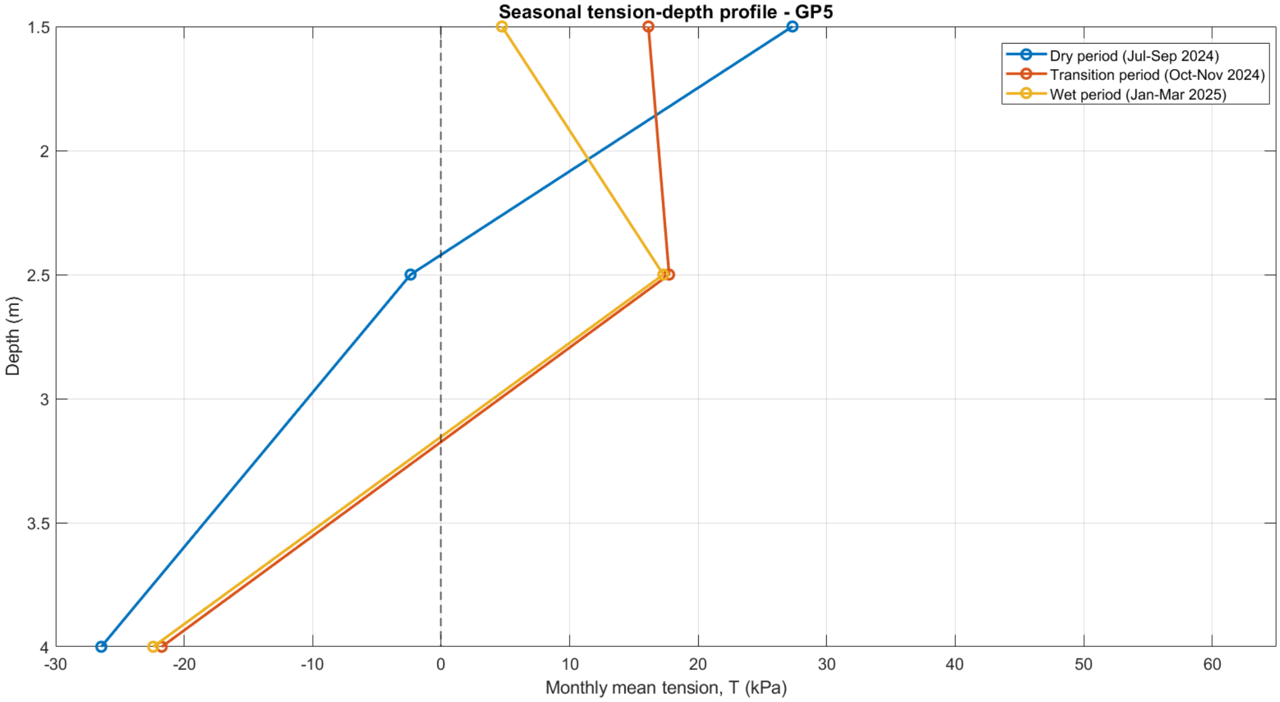

Figure 7.9 Seasonal depth profile of signed monthly mean tension, T, at station GP5 for the representative periods Jul–Sep 2024 (dry period), Oct–Nov 2024 (transition period), and Jan–Mar 2025 (wet period).

Figure 7.9 shows the seasonal depth profile of signed monthly mean tension at station GP5, where the representative periods were computed as the averages of July–September 2024 (dry period), October–November 2024 (transition period), and January–March 2025 (wet period). The profile includes the sensors at 1.5 m, 2.5 m, and 4.0 m depth. At 1.5 m, the seasonal mean tension is positive in all periods, with values of about 27 kPa in the dry period, 16 kPa in the transition period, and 5 kPa in the wet period. At 2.5 m, the values are lower and cluster around −2 kPa in the dry period and about 18 kPa in both the transition and wet periods. At 4.0 m, the dry-period mean is strongly negative at about −27 kPa, while the transition and wet means are also negative and close to −22 kPa.

Unlike a simple monotonic profile, the GP5 seasonal distribution shows a mixed depth behaviour. The upper sensor at 1.5 m has the highest positive tension in the dry period and then progressively decreases toward the wet period, which is physically consistent with seasonal wetting. However, the deeper levels do not follow a simple increase or decrease with depth. In particular, the 4.0 m sensor remains negative in all three representative periods, while the 2.5 m sensor lies near zero in the dry period and becomes positive in the transition and wet periods. Therefore, the GP5 profile should not be interpreted as evidence that suction systematically increases with depth. Instead, the results indicate that each monitored depth responds differently, likely reflecting local hydraulic and stratigraphic controls.

From a physical perspective, the profile suggests that the 1.5 m level behaves as the most seasonally sensitive layer at GP5, with the clearest reduction in tension from dry to wet conditions. In contrast, the 4.0 m sensor appears to remain under persistently wetter or near-saturated conditions, as indicated by the consistently negative values. The 2.5 m response is intermediate and does not behave monotonically with the 1.5 m and 4.0 m levels. This non-uniform pattern may reflect the influence of layered soil conditions, different hydraulic connectivity at depth, and delayed redistribution processes, rather than a simple vertical suction gradient.

The GP5 profile must also be interpreted in light of the QC assessment presented in Chapter 6. The GP5T1.5 sensor was classified as partially reliable because of extreme spikes and reset-like behaviour, while GP5T2.5 was considered partially reliable due to extreme spikes followed by long flatline behaviour, and GP5T4.0 was the most reliable within this group. Therefore, the broad seasonal pattern at GP5 is still informative, but the profile should be used mainly to identify the contrast between the responsive upper level (1.5 m), the transitional intermediate level (2.5 m), and the persistently wet deeper level (4.0 m), rather than to infer a strictly ordered depth trend.

Overall, the signed seasonal profile at GP5 supports a more cautious interpretation than the earlier absolute-value plot. It shows that the station does not exhibit a simple “greater depth = greater suction” relationship. Instead, the upper part of the profile shows the clearest seasonal drying-wetting signal, while the deepest sensor remains negative and therefore likely records a hydraulically different zone.

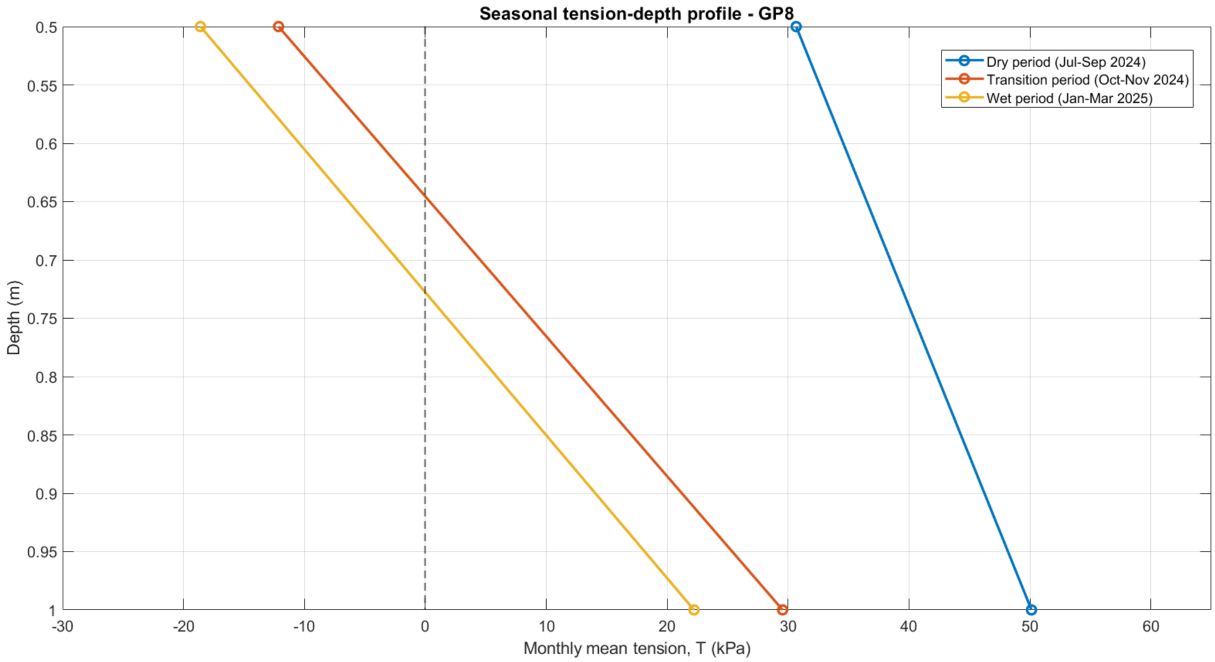

Figure 7.10 Seasonal depth profile of signed monthly mean tension, T, at station GP8 for the representative periods Jul–Sep 2024 (dry period), Oct–Nov 2024 (transition period), and Jan–Mar 2025 (wet period).

Figure 7.10 shows the seasonal depth profile of signed monthly mean tension at station GP8, where the representative periods were computed as the averages of July–September 2024 (dry period), October–November 2024 (transition period), and January–March 2025 (wet period). The profile includes two monitored depths, 0.5 m and 1.0 m. At 0.5 m, the seasonal mean tension decreases markedly from about 31 kPa in the dry period to about −12 kPa in the transition period and −19 kPa in the wet period. At 1.0 m, the seasonal mean is about 50 kPa in the dry period, decreases to about 30 kPa in the transition period, and further decreases to about 22 kPa in the wet period.

Compared with GP2 and GP5, the GP8 profile shows the clearest and most physically coherent seasonal shift from drier to wetter conditions. In both monitored depths, the tension values decrease progressively from the dry period to the transition period and again to the wet period. This is consistent with the expected reduction in soil suction under wetter seasonal conditions. At the same time, the two depths do not respond in the same way: the 1.0 m sensor remains positive in all three representative periods, whereas the 0.5 m sensor becomes negative during both the transition and wet periods. Therefore, the profile does not indicate that suction simply increases with depth in a uniform manner; rather, it shows that the deeper of the two monitored levels maintains a drier or more buffered condition, while the shallower level responds more strongly to seasonal wetting.

This contrast between 0.5 m and 1.0 m is physically plausible. The shallower sensor is more exposed to direct infiltration and rapid changes in near-surface moisture conditions, which explains why its seasonal mean crosses into negative values outside the dry period. In contrast, the 1.0 m sensor appears to be less directly affected by short-term surface wetting and retains positive tension throughout the year, although with a clear decline from summer to winter. The GP8 profile therefore suggests a depth-dependent buffering effect, in which the shallowest level responds rapidly and strongly to wetting, while the deeper level preserves a more stable unsaturated condition.

However, the profile should still be interpreted together with the QC assessment from Chapter 6. Both GP8T0.5 and GP8T1.0 were classified as partially reliable, with reset-like behaviour and later flatlining or spikes identified in the record. Therefore, although the overall seasonal pattern is consistent and physically interpretable, the profile should be used primarily to describe the broad seasonal contrast between the shallow and slightly deeper levels, rather than as a precise quantitative representation of the full vertical suction distribution.

Overall, the signed seasonal profile at GP8 is more informative than the previous absolute-value representation because it preserves the fact that the shallowest sensor becomes negative during wetter conditions. This directly addresses the physical meaning of the sign and shows that the station does not exhibit a simple monotonic increase of suction with depth, but rather a contrast between a highly responsive shallow layer and a deeper level that remains unsaturated throughout the representative periods.

7.4.2 Humidity (H-V) sensors: monthly mean evolution

Monthly mean Humidity-H exhibits a clear seasonal evolution over Apr 2024–May 2025, with coherent changes across several sensors and additional sensor-specific deviations. A general drying phase is observed during summer–early autumn 2024, followed by a transition around Sep–Oct 2024 and a relatively more stable/wetter regime during late 2024–spring 2025. This timing is consistent with the regime change also detected in the tension monthly means, supporting a seasonal control rather than purely instrumental noise.

Across stations and depths, the magnitude of monthly variability differs, indicating depth-dependent damping and/or local boundary effects. Some sensors show smooth seasonal trends (progressive decrease during summer, recovery after autumn) whereas others display abrupt steps or strong excursions that should be interpreted cautiously and cross-checked with the colocated tension sensors and the QC segmentation defined in Chapter 6.

The late-summer minimum (Aug–Sep 2024) and subsequent increase from autumn onward are consistent with the forcing data, namely reduced summer rainfall followed by wetter autumn conditions and increased hydrometric activity, which collectively promote moisture recovery in the unsaturated levee zone.

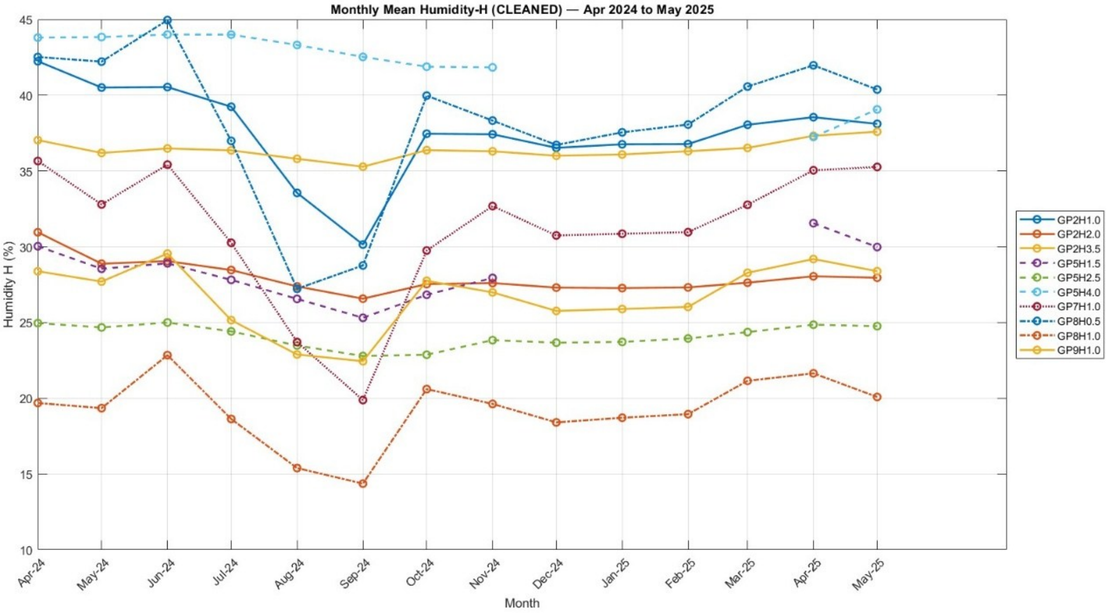

Figure 7.11 Monthly mean Humidity-H (%) after QC cleaning (Apr 2024–May 2025).

Figure 7.11 shows a coherent seasonal response in the horizontal humidity probes, with a **general drying phase from late spring to summer (approximately Jun–Sep 2024)** followed by **rewetting and recovery from autumn to spring (Oct 2024–May 2025)**. This pattern is consistent with the environmental forcing shown in **Figure 7.2**, where monthly rainfall is relatively lower in the warm season and increases markedly from autumn onward, and with **Figure 7.3**, where river-stage variability becomes more pronounced during the wet season. The simultaneous reduction in several H-sensor readings around **August–September 2024** (e.g., GP7H1.0, GP8H1.0, and parts of GP2/GP5 groups) indicates seasonal moisture depletion in the levee body under drier atmospheric and surface conditions.

A second clear feature is the **autumn rewetting transition (around Oct 2024)**, visible as a recovery in many sensors after the summer minimum. This timing aligns with the increase in cumulative rainfall in **Figure 7.2** and the return of more active hydrometric conditions in **Figure 7.3**, suggesting that both **local infiltration (rainfall-driven)** and **boundary-condition effects (river-stage fluctuations)** contribute to moisture recharge. The response magnitude differs by sensor, which is physically expected: some probes (e.g., **GP2H1.0, GP2H3.5, GP8H0.5**) remain at comparatively higher moisture levels and show smoother seasonal fluctuations, while others (e.g., **GP8H1.0, GP7H1.0**) show stronger amplitude and sharper summer drops, indicating local heterogeneity in soil texture, compaction, or hydraulic connectivity.

Finally, Fig. 7.7 highlights **persistent spatial variability between stations and depths**, even under the same seasonal forcing. Sensors such as **GP2H1.0 / GP2H3.5** maintain relatively high monthly mean humidity throughout the year, whereas **GP8H1.0** remains much lower and more variable, and **GP5H2.5** stays comparatively stable with limited seasonal amplitude. This behavior supports the interpretation that the levee does not respond as a uniform body; instead, moisture evolution reflects a combination of **depth-dependent damping**, **local stratigraphic differences**, and **position relative to hydraulic boundaries**. Overall, the H-sensor trends in **Figure 7.11** are physically consistent with the seasonal wetting–drying framework established by the rainfall and river-level series (Figs. 7.2 and 7.3).

Table 7.3 Descriptive statistics of cleaned Humidity-H sensors (Apr 2024–May 2025).

Sensor	**Mean (%)**	**Std (%)**	**Min (%)**	**Max (%)**	**Valid Count**	**Total Count**	**Missing (%)**
GP2H1.0	38.16	3.29	23.5	44.3	23214	23214	0.00
GP2H2.0	28.38	1.69	26.3	38.0	23214	23214	0.00
GP2H3.5	36.49	0.68	34.6	38.4	23213	23214	0.00
GP5H1.5	28.64	2.00	25.0	58.7	16935	23214	27.05
GP5H2.5	24.21	0.75	22.4	25.5	23214	23214	0.00
GP5H4.0	42.47	2.11	34.6	44.7	17197	23214	25.92
GP7H1.0	31.69	4.62	18.7	38.4	23214	23214	0.00
GP8H0.5	38.83	5.10	24.3	49.2	23214	23214	0.00
GP8H1.0	19.30	2.37	13.6	28.3	23214	23214	0.00
GP9H1.0	26.95	2.38	21.7	49.9	23214	23214	0.00

The descriptive statistics of the cleaned Humidity-H sensors confirm clear differences in moisture regime between stations and depths. The highest mean humidity values are observed at **GP5H4.0 (42.47%)**, **GP8H0.5 (38.83%)**, and **GP2H1.0 (38.16%)**, while the lowest mean value is recorded at **GP8H1.0 (19.30%)**, indicating persistently drier conditions at this sensor. Variability is generally moderate, but larger standard deviations are observed for **GP8H0.5 (5.10%)** and **GP7H1.0 (4.62%)**, suggesting stronger seasonal fluctuations and/or short-term wetting events. In contrast, **GP2H3.5 (Std = 0.68%)** and **GP5H2.5 (Std = 0.75%)** show very stable behavior over time. Missing data are negligible for most sensors; however, **GP5H1.5 (27.05%)** and **GP5H4.0 (25.92%)** present substantial missing percentages, consistent with the previously identified data gaps and segmented usability in the QC assessment.

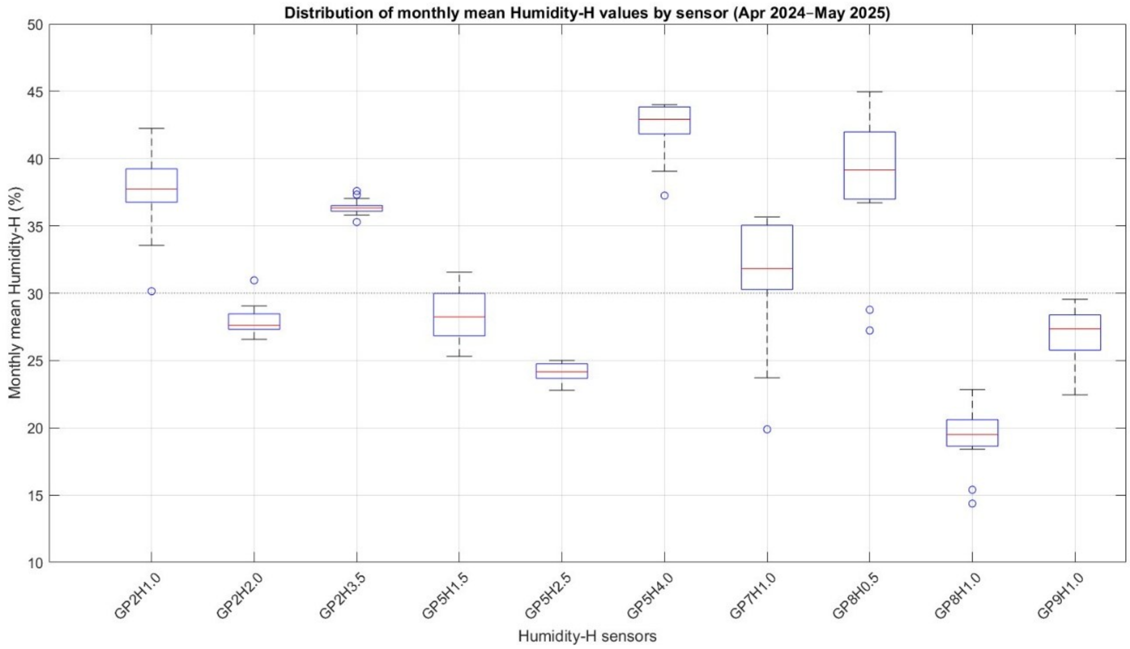

Figure 7.12 Boxplot distribution of monthly mean Humidity-H values for all horizontal humidity sensors (GP2, GP5, GP7, GP8, and GP9) over the monitoring period (April 2024–May 2025).

Figure 7.12 summarizes the distribution of monthly mean Humidity-H values for all horizontal humidity sensors during April 2024–May 2025. The boxplots confirm the seasonal patterns observed in the time-series plot, while providing a compact comparison of central tendency and variability among sensors. GP5H4.0 and GP8H0.5 show the highest humidity levels (highest median values), indicating persistently wetter conditions at those locations/depths, whereas GP8H1.0 and GP5H2.5 exhibit the lowest humidity ranges, indicating comparatively drier conditions. Sensors such as GP2H3.5 and GP5H2.5 display narrow interquartile ranges, suggesting relatively stable monthly behavior, while GP7H1.0, GP8H0.5, and GP2H1.0 show wider spreads and/or outliers, reflecting stronger seasonal variability and sensitivity to hydrometeorological forcing. Overall, the boxplot supports the interpretation that Humidity-H responses differ by station and depth, with variability patterns consistent with the rainfall and river water-level fluctuations presented in Figures 7.2 and 7.3.

Humidity-V sensors: depth profiles and monthly evolution:

Figures (7.10-7.12) present the monthly mean evolution of the **GP-V (volumetric water content / humidity V)** sensors after QC cleaning for three stations (GP3, GP4, GP6) and four depths (0.5, 1.0, 1.5, and 2.0 m). Overall, the three stations show a coherent seasonal signal characterized by:

1. **Drying phase from spring to late summer 2024**, with decreasing monthly means and a minimum typically occurring between **July–September 2024**.

2. **Recovery and stabilization from autumn 2024 onward** (approximately **October 2024**), where values increase and then remain relatively steady through winter–spring 2025, with a slight wetting tendency toward March–May 2025 in several series.

Across the vertical arrays, the recovery after autumn rainfall is typically stronger and earlier in shallower sensors, while deeper sensors show a delayed and damped response, consistent with vertical attenuation of infiltration and slower moisture redistribution with depth.

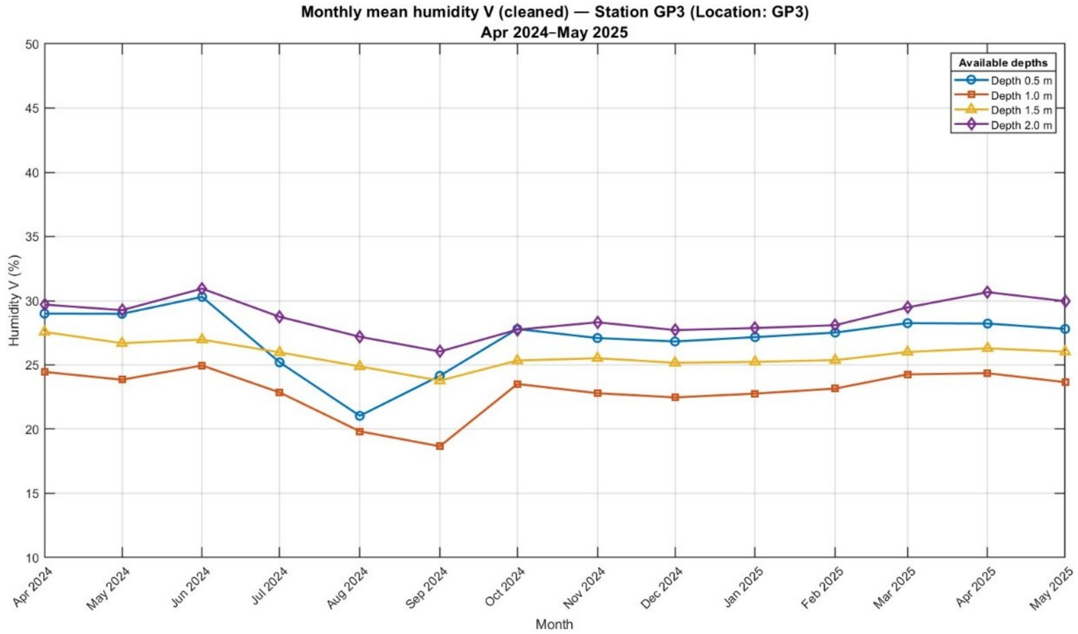

Figure 7.13 Monthly mean volumetric water content (Humidity-V) at station GP3 (depths 0.5–2.0 m) for the study period (Apr 2024–May 2025).

At **GP3**, the Humidity-V series show a **moderate and coherent seasonal signal** across depths, with a general decrease from late spring/early summer toward **August–September 2024**, followed by a recovery from autumn onward. The lowest values around late summer are consistent with the **dry summer phase** identified from the forcing variables (lower rainfall and generally lower river influence), while the gradual increase after September is consistent with the transition to **autumn–winter rewetting** driven by increased rainfall. Depth-dependent damping is visible: the deeper sensors (especially **2.0 m**) remain more stable and show smaller fluctuations than the shallower levels, indicating a buffered response to atmospheric forcing.

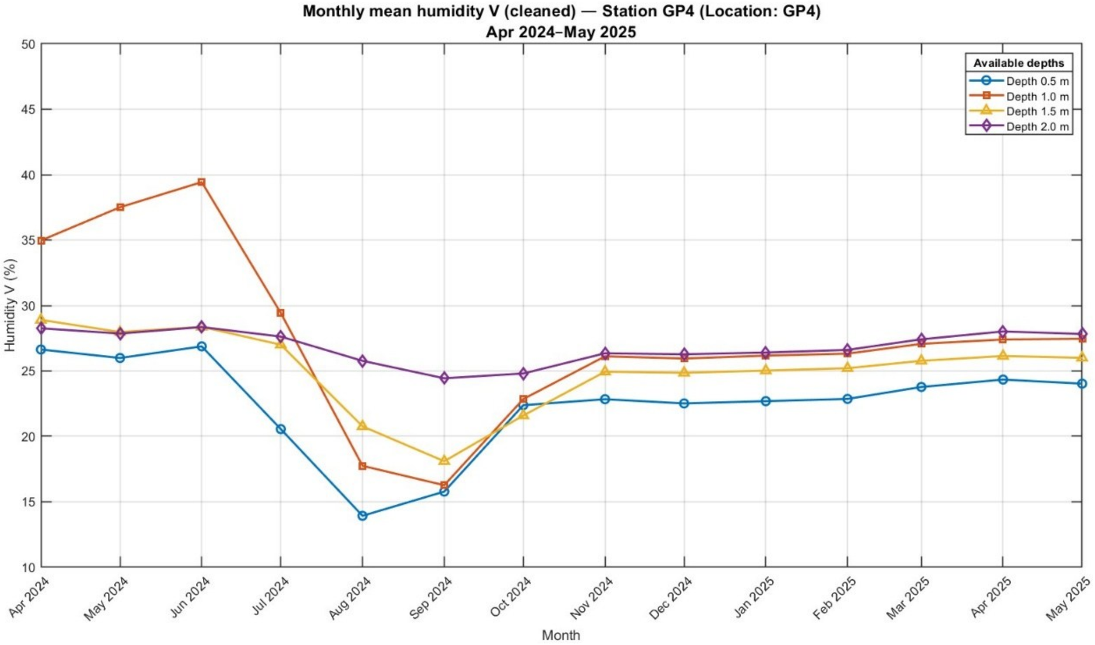

Figure 7.14 Monthly mean volumetric water content (Humidity-V) at station GP4 (depths 0.5–2.0 m) for the study period (Apr 2024–May 2025).

At **GP4**, the Humidity-V sensors show the **strongest seasonal drying–rewetting cycle** among the three V stations. A marked reduction is observed from early summer to a minimum in **August–September 2024**, especially at the shallower and intermediate depths, followed by a clear recovery from **October 2024** onward. This pattern aligns well with the forcing series: the summer drying phase corresponds to relatively low rainfall and weaker hydrometric forcing, while the autumn recovery corresponds to increased rainfall and more frequent river-stage activity. The larger amplitude at GP4 suggests stronger sensitivity to near-surface moisture changes and/or more direct hydraulic connection to seasonal boundary conditions compared with GP3.

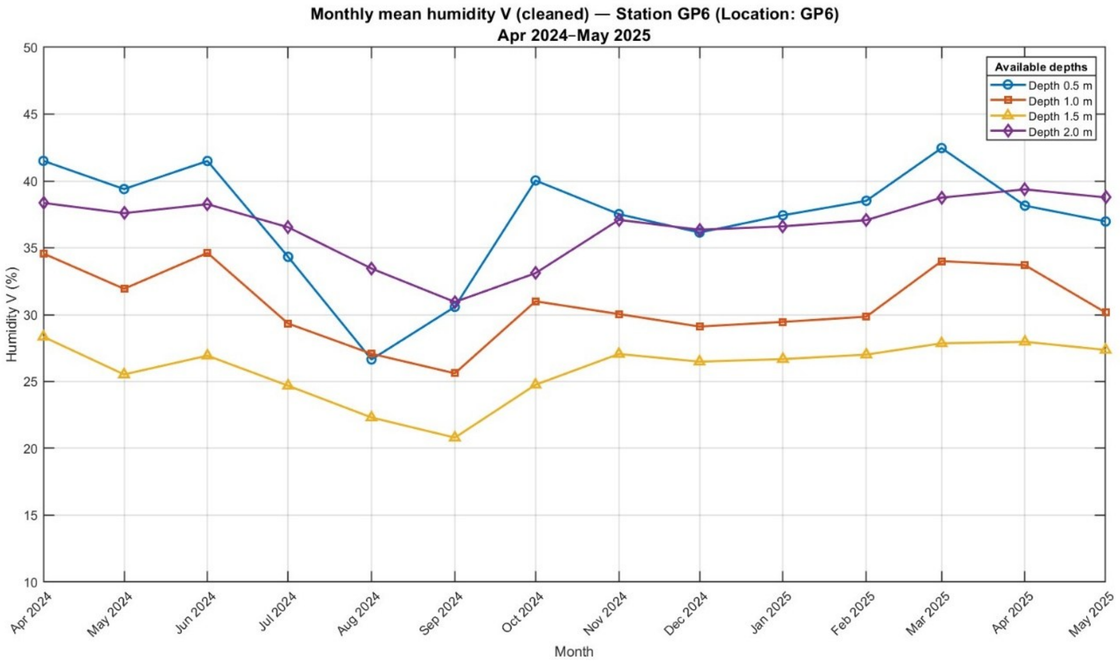

Figure 7.15 Monthly mean volumetric water content (Humidity-V) at station GP6 (depths 0.5–2.0 m) for the study period (Apr 2024–May 2025).

At **GP6**, the Humidity-V series remain **consistently higher overall** and show a smoother seasonal evolution compared with GP3 and GP4, although a summer minimum is still visible around **August–September 2024**. After this period, all depths recover and remain relatively stable through the wet season, with only moderate month-to-month variation. This behavior is consistent with the rainfall and hydrometric trends, but the smaller seasonal amplitude suggests a **more buffered moisture regime** (e.g., stronger storage capacity and/or reduced sensitivity to short-term atmospheric forcing). The depth ordering is generally preserved, and the curves remain relatively parallel, indicating good internal consistency of the vertical moisture response at this station.

Table 7.4 Descriptive statistics of cleaned Humidity-V sensors (Apr 2024–May 2025).

Sensor	**Mean (%)**	**Std (%)**	**Min (%)**	**Max (%)**	**Valid Count**	**Total Count**	**Missing (%)**
GP3V0.5	27.33	2.72	17.2	56.5	23414	23414	0.00
GP3V1.0	23.16	1.84	15.8	37.0	23414	23414	0.00
GP3V1.5	26.01	1.10	23.0	28.5	23414	23414	0.00
GP3V2.0	28.82	1.43	25.7	34.8	23414	23414	0.00
GP4V0.5	23.03	3.93	12.5	40.2	23414	23414	0.00
GP4V1.0	28.42	6.63	15.3	66.1	23414	23414	0.00
GP4V1.5	25.53	3.16	17.0	32.3	23414	23414	0.00
GP4V2.0	27.03	1.27	23.4	29.0	23414	23414	0.00
GP6V0.5	37.76	4.75	22.3	56.1	23414	23414	0.00
GP6V1.0	31.23	3.29	25.1	41.6	23414	23414	0.00
GP6V1.5	26.28	2.31	20.3	29.8	23414	23414	0.00
GP6V2.0	36.81	2.44	30.0	40.1	23414	23414	0.00

The descriptive statistics of the cleaned Humidity-V sensors show consistent differences among stations and depths, with all sensors having complete records (0% missing data). The highest mean values are observed at **GP6V0.5 (37.76%)** and **GP6V2.0 (36.81%)**, indicating relatively wetter conditions at station GP6, while the lowest means occur at **GP4V0.5 (23.03%)** and **GP3V1.0 (23.16%)**. Variability is generally moderate, but **GP4V1.0** shows the largest dispersion (**Std = 6.63%**, Max = 66.1%), reflecting stronger fluctuations and episodic peaks, which is consistent with the QC interpretation of spike-prone behavior. In contrast, sensors such as **GP3V1.5 (Std = 1.10%)** and **GP4V2.0 (Std = 1.27%)** show comparatively stable responses. Overall, the Humidity-V statistics confirm that station GP6 tends to maintain higher volumetric moisture levels, while GP3 and GP4 exhibit more depth-dependent variability and stronger temporal fluctuations in selected sensors.

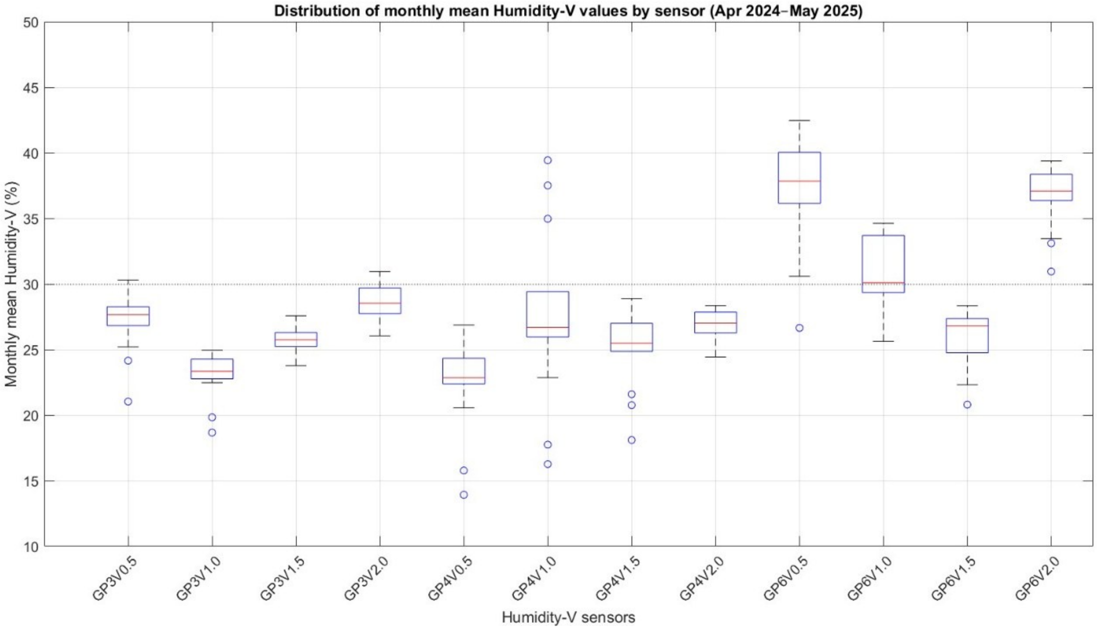

Figure 7.16 Boxplot of monthly mean Humidity-V values for the monitored vertical-profile sensors over the study period (Apr 2024–May 2025).

The boxplot of monthly mean Humidity-V values (**Figure 7.16**) provides a compact comparison of the distribution and variability of volumetric water content across the vertical-profile sensors during Apr 2024–May 2025. The GP6 sensors generally exhibit the highest humidity levels (notably GP6V0.5 and GP6V2.0), indicating persistently wetter conditions at this station. In contrast, the GP4 sensors show stronger variability, particularly GP4V1.0, which presents a wider spread and several outlier months, suggesting higher sensitivity to seasonal wetting–drying cycles and transient hydrometeorological forcing. The GP3 sensors are comparatively more stable, with narrower interquartile ranges and more compact distributions. These statistical patterns are consistent with the monthly trends shown in Figs. 7.10–7.12 and align with the rainfall and water-level forcing discussed in previous sections, where wetter periods (autumn–winter and high-stage events) correspond to higher monthly humidity values, while drier summer conditions produce lower values and occasional low outliers.

7.4.2.1 Seasonal depth profiles of humidity

To complement the monthly evolution plots, seasonal depth-profile plots were prepared for the Humidity-V arrays using representative dry (Jul–Sep 2024), transition (Oct–Nov 2024), and late wet/early spring (Jan–Mar 2025) periods. These figures provide a more direct visualization of how the vertical moisture distribution changes through the seasonal cycle. In particular, they help identify whether the strongest drying and rewetting response is concentrated in shallow layers, whether the response becomes damped with depth, and whether the profile shape remains stable or changes between stations. Unlike the time-series plots, which emphasize temporal evolution, the seasonal depth profiles highlight the internal vertical structure of the response and therefore provide a more intuitive basis for physical interpretation of infiltration, buffering, and depth-dependent damping.

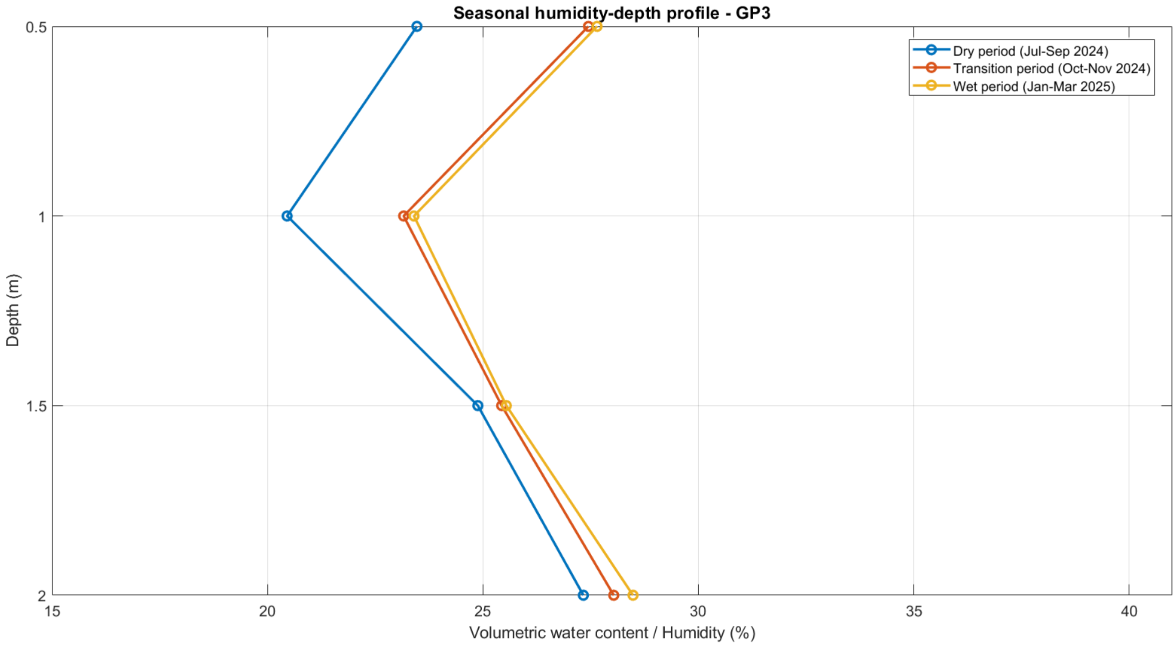

Figure 7.17 Seasonal depth profile of volumetric water content at station GP3 for representative dry (Jul–Sep 2024), transition (Oct–Nov 2024), and late wet/early spring (Jan–Mar 2025) periods.

Figure 7.17 shows the seasonal depth profile of monthly mean volumetric water content at station GP3 for the representative periods July–September 2024 (dry period), October–November 2024 (transition period), and January–March 2025 (wet period). The profile indicates a consistent seasonal shift toward higher water content from the dry period to the transition and wet periods. At 0.5 m, the volumetric water content increases from about 23.5% in the dry period to about 27.8% in the transition period and about 28.0% in the wet period. At 1.0 m, the corresponding values are about 20.4%, 23.1%, and 23.2%, respectively. At 1.5 m, the increase is more moderate, from about 24.9% in the dry period to about 25.5% in the transition period and 25.6% in the wet period. At 2.0 m, the water content rises from about 27.4% in the dry period to about 28.2% in the transition period and about 28.6% in the wet period.

The profile therefore confirms a real seasonal wetting signal throughout the monitored vertical array, but the response is not uniform with depth. The 1.0 m level is the driest part of the profile in all three representative periods, whereas the shallowest (0.5 m) and deepest (2.0 m) sensors remain wetter. This indicates that the GP3 vertical distribution is not characterized by a simple monotonic increase or decrease of water content with depth. Instead, it suggests a local minimum at intermediate depth, with wetter conditions both above and below.

The seasonal differences are clearest between the dry period and the two wetter representative periods. At all depths, the dry-period profile plots to the left of the transition and wet profiles, confirming lower water content during summer drying and moisture recovery afterward. However, the transition and wet profiles are relatively close to one another, which suggests that much of the seasonal recharge had already occurred by October–November 2024, with more limited additional increase by January–March 2025. This indicates that the main seasonal shift at GP3 is from the summer dry state toward a wetter autumn–winter state, rather than a continuous large increase throughout the whole wet season.

From a physical point of view, the profile suggests that moisture redistribution at GP3 is influenced not only by seasonal atmospheric forcing but also by local hydraulic and stratigraphic controls. In particular, the relatively low water content at 1.0 m may indicate a more freely draining or more seasonally sensitive intermediate horizon, while the deeper 2.0 m level appears more buffered and moisture-retaining. Therefore, the GP3 response is better interpreted as a non-uniform depth-dependent moisture structure, rather than a simple linear damping or monotonic wetting pattern with depth.

Overall, the GP3 profile shows a coherent but moderate seasonal moisture redistribution, with a clear dry-to-wet shift and a non-monotonic vertical structure. The figure supports interpretation in terms of seasonal wetting, intermediate-depth drying, and deeper buffering, without assuming that the moisture response changes uniformly with depth.

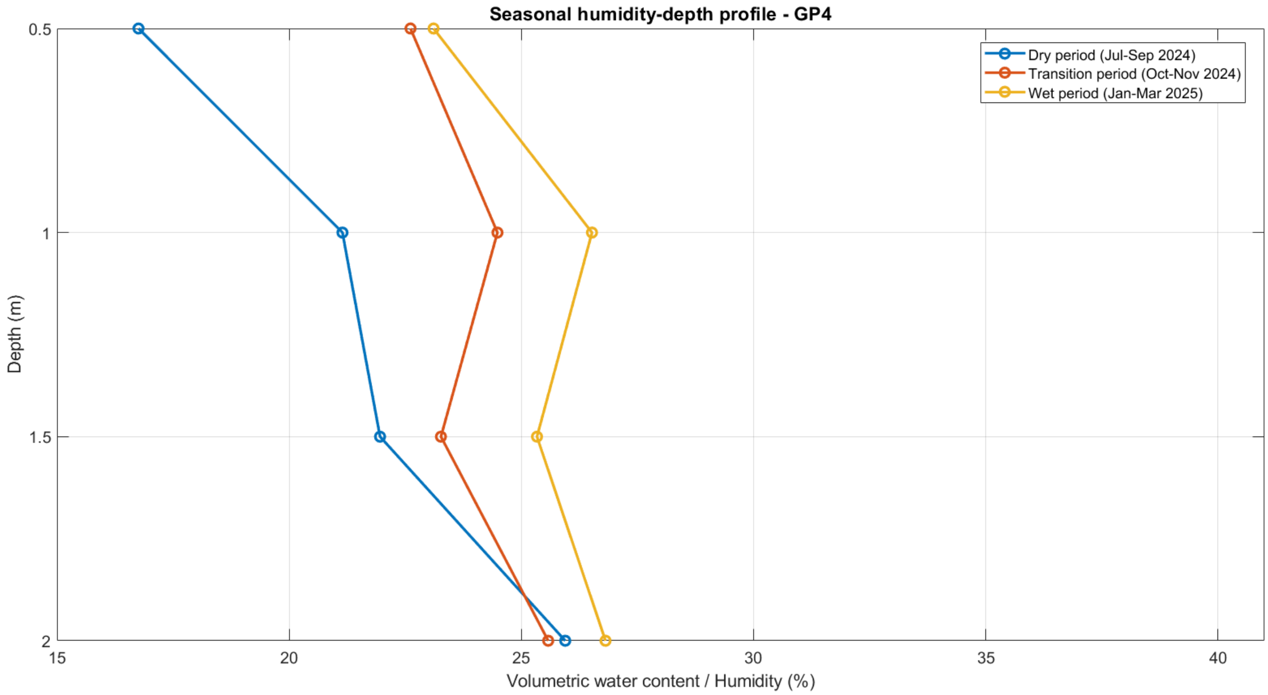

Figure 7.18 Seasonal depth profile of volumetric water content at station GP4 for representative dry (Jul–Sep 2024), transition (Oct–Nov 2024), and late wet/early spring (Jan–Mar 2025) periods.

Figure 7.18 shows the seasonal depth profile of monthly mean volumetric water content at station GP4 for the representative periods July–September 2024 (dry period), October–November 2024 (transition period), and January–March 2025 (wet period). The profile shows a clear and systematic seasonal shift toward higher water content from the dry period to the transition and wet periods at all monitored depths. At 0.5 m, the water content increases from about 16.7% in the dry period to about 22.6% in the transition period and about 23.1% in the wet period. At 1.0 m, the corresponding values are about 21.1%, 24.5%, and 26.5%. At 1.5 m, they increase from about 21.9% to 23.2% and then to about 25.4%. At 2.0 m, the values rise from about 26.0% in the dry period to about 25.6% in the transition period and about 26.8% in the wet period.

Compared with GP3, the GP4 profile shows a more regular vertical structure. In all three representative periods, the shallowest level (0.5 m) is the driest part of the profile, while deeper levels are wetter. This is physically plausible, because the upper layer is more exposed to seasonal drying, whereas deeper layers retain moisture more effectively. However, the profile is still not perfectly monotonic. In particular, the 2.0 m level remains the wettest in the dry and wet periods, while the 1.0 m and 1.5 m levels show intermediate values and respond more clearly to seasonal recharge.

The strongest seasonal contrast is observed in the shallow and intermediate part of the profile. At 0.5 m, the increase from the dry period to the wetter periods is particularly marked, indicating a strong surface-controlled seasonal response. At 1.0 m and 1.5 m, the water content also increases consistently, showing that seasonal wetting penetrates beyond the shallowest layer. By contrast, the 2.0 m sensor remains relatively stable and already wet in all three periods, suggesting a more buffered hydraulic condition at depth. This indicates that the GP4 vertical response is controlled by both surface seasonal forcing and depth-dependent moisture retention, with the deepest level showing the smallest relative seasonal variability.

The transition-period profile lies between the dry and wet profiles at most depths, which supports a coherent seasonal progression from summer drying toward autumn–winter rewetting. At the same time, the differences between transition and wet periods are smaller than those between dry and transition, suggesting that a substantial part of the seasonal recharge had already taken place by October–November 2024. Thus, the GP4 profile reflects a relatively orderly wetting evolution, with the most pronounced recovery occurring in the upper part of the profile.

Overall, the GP4 humidity profile is the most physically consistent of the humidity arrays, showing a clear dry-to-wet seasonal shift and a plausible increase in moisture retention with depth. Even so, the profile still highlights that the response is not governed by depth alone, but by the combination of seasonal drying at the surface, downward wetting propagation, and deeper buffering within the monitored vertical section.

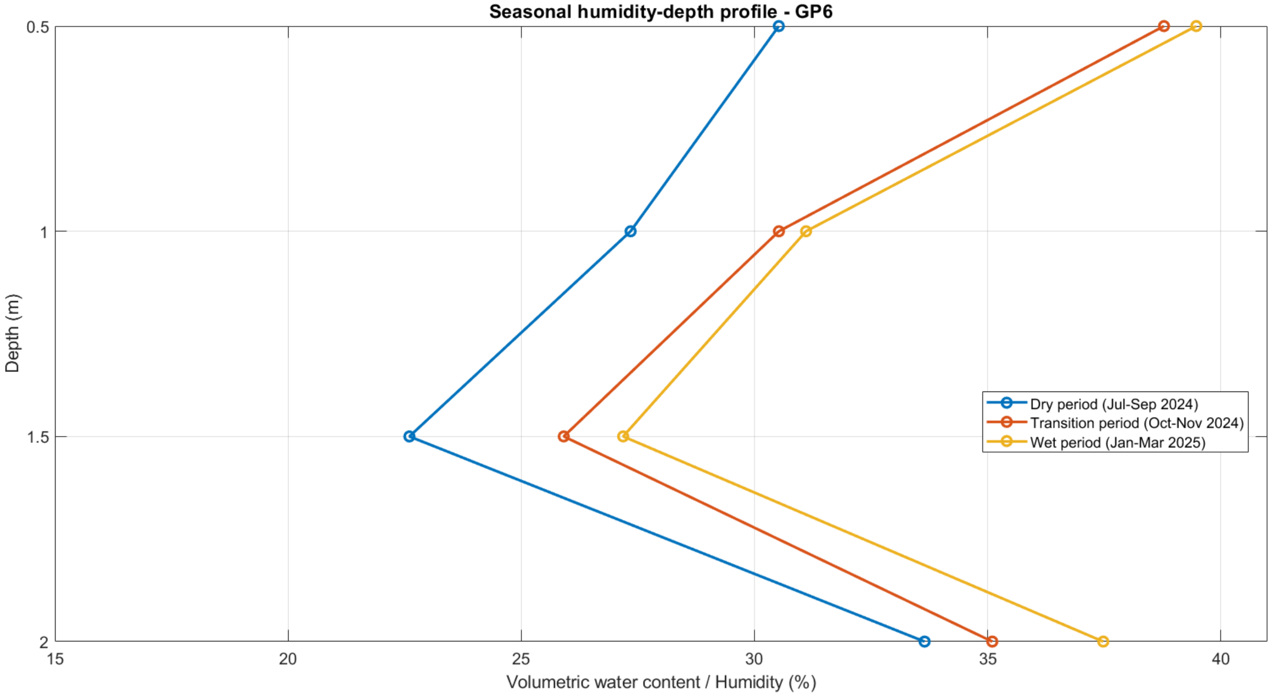

Figure 7.19 Seasonal depth profile of volumetric water content at station GP6 for representative dry (Jul–Sep 2024), transition (Oct–Nov 2024), and late wet/early spring (Jan–Mar 2025) periods.

Figure 7.19 shows the seasonal depth profile of monthly mean volumetric water content at station GP6 for the representative periods July–September 2024 (dry period), October–November 2024 (transition period), and January–March 2025 (wet period). The profile indicates a clear seasonal shift toward higher water content from the dry period to the transition and wet periods at all monitored depths. At 0.5 m, the volumetric water content increases from about 30.5% in the dry period to about 38.8% in the transition period and about 39.5% in the wet period. At 1.0 m, the corresponding values are about 27.3%, 30.5%, and 31.1%. At 1.5 m, the values rise from about 22.6% in the dry period to about 25.9% in the transition period and about 27.1% in the wet period. At 2.0 m, the water content increases from about 33.7% in the dry period to about 35.1% in the transition period and about 37.5% in the wet period.

The GP6 profile shows a strong seasonal moisture signal, but, as in the other humidity arrays, the response is not monotonic with depth. The 1.5 m level is the driest part of the profile in all three representative periods, whereas the shallowest (0.5 m) and deepest (2.0 m) sensors remain wetter. This indicates that the vertical moisture distribution at GP6 is characterized by a pronounced intermediate-depth minimum, rather than by a simple increase or decrease of water content with depth.

The shallowest sensor at 0.5 m shows the highest water contents and also one of the strongest seasonal shifts, suggesting that this level is highly responsive to seasonal wetting and remains relatively moisture-rich even during the dry period. At the other extreme, the 2.0 m sensor is also consistently wet and becomes even wetter during the transition and wet periods, indicating a buffered deeper zone with high moisture retention. Between these two wetter levels, the 1.0 m and especially 1.5 m sensors define a drier intermediate part of the profile. This pattern suggests that the GP6 array is influenced by layered hydraulic behaviour, where the middle part of the section drains or dries more efficiently than both the shallow and deep parts.

The seasonal progression is also clear. At every depth, the dry-period profile plots to the left of the transition and wet profiles, confirming lower water content during summer conditions and progressive recharge afterward. The transition profile already shows substantial wetting relative to the dry period, while the wet profile shifts slightly further to the right, especially at 0.5 m and 2.0 m. This indicates that seasonal moisture recovery had already begun by October–November 2024, but continued into January–March 2025, particularly in the shallowest and deepest levels.

Overall, the GP6 profile shows one of the clearest examples of a non-monotonic vertical moisture structure, with wetter conditions near the surface and at depth, separated by a drier intermediate zone. The figure therefore supports interpretation in terms of seasonal wetting superimposed on a layered hydraulic profile, rather than a simple linear damping or uniform moisture increase with depth.

Depth-dependent behaviour and physical consistency

Across the monitored profiles, the seasonal signal shows a generally physical but **station-specific** depth response rather than a single uniform pattern of damping with depth. In several cases, shallower sensors exhibit stronger seasonal shifts and faster response to drying and rewetting, while deeper sensors appear more buffered. However, the revised tension and humidity depth profiles also show that the vertical response is not always monotonic. At some stations, intermediate depths define local minima or maxima, indicating that the observed behaviour is controlled not only by depth, but also by **local hydraulic conditions, moisture redistribution, and stratigraphic contrasts** within the monitored section.

The common seasonal progression from the summer dry period toward wetter autumn–winter conditions supports the interpretation that the observed variations are predominantly **physical** and linked to seasonal boundary conditions. At the same time, the figures indicate that the timing and amplitude of the response differ between depths and stations. Therefore, the depth profiles should not be interpreted using an oversimplified assumption such as "suction always increases with depth" or "water content always increases with depth." Instead, they should be read as evidence of a **depth-dependent but locally modulated vertical response**, in which some layers are more responsive, while others remain wetter, drier, or more buffered through the seasonal cycle.

Where minor deviations occur, interpretation should be supported by: (i) the **usable time windows and QC classifications** defined in Chapter 6, (ii) the corresponding behaviour of nearby or co-located sensors where comparison is meaningful, and (iii) the monthly data coverage, so that months with fewer valid records are not over-interpreted. In this way, the depth-profile figures are used not as strict proof of a simple vertical gradient, but as a physically guided basis for identifying which parts of the profile respond most strongly to seasonal forcing and which parts reflect more stable or buffered hydraulic conditions.

7.5 Water retention curve analysis

This section presents the water retention curve (WRC) analysis developed from paired tension-humidity measurements at the San Giorgio monitoring stations. Unlike the particle-size distribution and Atterberg limits results discussed in the previous sections, the WRC analysis is not a direct laboratory determination performed under controlled suction conditions. Instead, it represents a field-derived interpretation obtained by pairing tension sensors, used here as a proxy for matric suction, with co-located humidity sensors converted to water content. The objective is to evaluate whether the paired signals define a physically coherent retention relationship and to assess how data cleaning improves the reliability of the fitted response.

The interpretation is based on the van Genuchten model, which is widely used to describe the relationship between water content and suction in unsaturated soils. The results are then discussed in the light of the soil types identified earlier in Chapter 4 and compared qualitatively with the laboratory-type retention behaviour described in the literature, particularly the conceptual framework presented by Fredlund, Rahardjo, and Fredlund in "Unsaturated Soil Mechanics in Engineering Practice" and the predictive approach proposed by Aubertin et al. (2003). Because no direct laboratory SWCC measurements and no void-ratio dataset were available for the tested samples, the comparison remains qualitative rather than a strict one-to-one validation.

7.5.1 van Genuchten model and rationale

The van Genuchten equation was adopted to describe the soil-water retention behaviour because it provides a flexible analytical form capable of reproducing the main shape of drying curves for a wide range of unsaturated soils. In this study it was used to fit paired field observations of water content and suction, allowing the dominant retention branch to be described with a small set of physically interpretable parameters.

In terms of volumetric water content θ, the model can be written as:

$$\theta(\mathrm{h}) = \theta_r + (\theta_s - \theta_r) / [1 + (\alpha\ \mathrm{h})^{\mathrm{n}}]^{\mathrm{m}}$$

$$m = 1 - 1/n$$

where θr is the residual volumetric water content, θs is the saturated volumetric water content, α is an inverse air-entry parameter controlling the horizontal position of the curve, and n and m govern the overall shape and steepness of the retention response. Within the present work, suction h was expressed in kPa using the absolute magnitude of tension. The model was fitted separately for each paired sensor dataset so that differences between locations and depths could be evaluated.

A key point is that the curves obtained here are field-derived WRCs rather than laboratory-measured soil-water characteristic curves. For this reason, the fitted parameters reflect not only material behaviour but also field effects such as seasonal wetting-drying cycles, sensor drift, hysteresis, local heterogeneity, and temporary mismatches between paired sensors. The model is therefore used here as an interpretative fitting tool rather than as a strictly laboratory calibration curve.

7.5.2 Field-derived WRC from paired sensor data

The WRC analysis was carried out using co-located pairs of tension and humidity sensors installed at the same depth and location. Physically, periods of increasing moisture content should correspond to lower suction, whereas drying should correspond to higher suction. This expected inverse relationship was used as the main consistency criterion for evaluating the coherence of the paired measurements. Only locations with sufficiently usable paired records after the Chapter 5 quality-control workflow were retained for fitting.

Four sensor pairs were analysed: GP2 at 1.0 m, GP5 at 1.5 m, GP8 at 0.5 m, and GP8 at 1.0 m. For each pair, the fit quality was evaluated first on the raw matched dataset and then on the cleaned dataset after excluding invalid values and non-representative periods. Table 4.3 summarizes the coefficient of determination obtained for the raw and cleaned datasets, showing the effect of the cleaning strategy on the coherence of the retention relationship.

Table 7.5 Summary of field-derived WRC analysis outcomes for each paired sensor set.

Pair (location, depth)	**Sensors**	**R² (Raw data)**	**R² (Cleaned data)**
GP2 (1.0 m)	GP2T1.0 & GP2H1.0	0.243	0.711
GP5 (1.5 m)	GP5T1.5 & GP5H1.5	0.557	0.925
GP8 (0.5 m)	GP8T0.5 & GP8H0.5	0.292	0.993
GP8 (1.0 m)	GP8T1.0 & GP8H1.0	0.701	0.896

As shown in Table 7.5, the cleaned datasets consistently produce stronger and more physically coherent retention relationships than the raw datasets. The improvement is particularly marked for GP2 (1.0 m) and GP8 (0.5 m), where large scatter and anomalous periods in the unfiltered data mask the main drying branch. The cleaned results confirm that preprocessing is essential before fitting any retention model to field monitoring data.

7.5.3 Effect of cleaning and fitting on representative WRC plots

To evaluate how data treatment influences the field-derived water retention relationship, the GP5 sensor pair at **1.5 m depth** was analysed using both the **raw matched dataset** and the **cleaned dataset**. In both cases, tension was plotted against interpolated volumetric water content and the points were colored by time to show temporal progression. The field data were then fitted using the **van Genuchten model**. In addition, an **Aubertin-based predictive WRC** was superimposed as a laboratory-informed reference curve.

For the updated Aubertin comparison, the predictive curve was no longer generated using only arbitrarily assumed void-ratio values. Instead, the **wet-end volumetric water content at very low suction** was interpreted as an estimate of the **porosity, n**, consistent with the condition of near-full saturation. The corresponding **void ratio, $e = n/(1 - n)$**, was then calculated and used in the Aubertin model. This procedure provides a more physically consistent comparison between the field-derived WRC and the predictive curve, especially near the low-suction end where the previous assumed values tended to overestimate the water content.

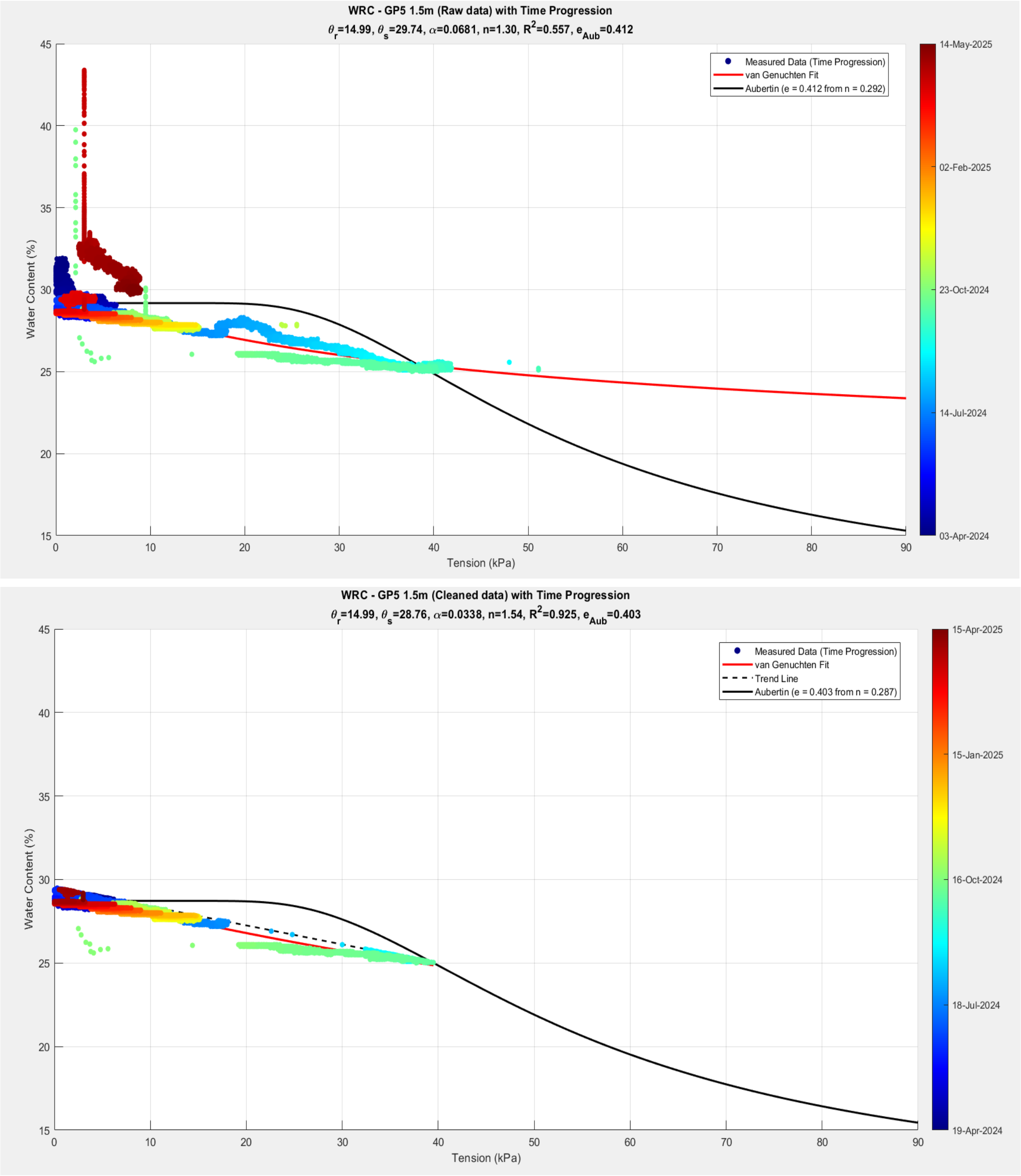

Figure 7.20 Field-derived water retention plots for the GP5 sensor pair at 1.5 m depth: raw matched data (top) and cleaned data (bottom), both coloured by time progression and fitted using the van Genuchten model. The figure also includes the Aubertin-based predictive WRC computed using a field-informed void ratio derived from the estimated porosity at very low suction, together with the trend-line filter used for the cleaned dataset.

For the sensor pair at GP5, depth 1.5 m, the water retention correlation was evaluated using both the raw matched tension–humidity dataset and the corresponding cleaned dataset. In the raw dataset, the measured points form a broad and scattered cloud, especially at low suction, and do not define a single coherent retention branch. This is reflected in the relatively weak van Genuchten fit ($R^2 = 0.557$), indicating that the untreated data include substantial variability associated with transient effects, hysteresis, seasonal path dependence, or non-representative periods.

After cleaning and filtering, the retained data define a much narrower and more coherent branch, and the van Genuchten fit improves substantially to $R^2 = 0.925$. The cleaned dataset shows a more regular decrease in water content with increasing tension and therefore provides a more physically interpretable representation of the dominant field response. The time colouring also indicates a clearer progression along the retained branch, suggesting that the cleaned data capture the main seasonal retention behaviour more consistently than the raw cloud.

The Aubertin-based predictive curve was computed using a field-informed porosity estimate derived from the low-suction end of the observed data. Following the physical interpretation of the model, the volumetric water content at very low suction was treated as an estimate of the porosity, n, corresponding to near-saturated conditions, and the associated void ratio was then calculated as $e = n/(1 - n)$. For GP5, this procedure yielded $n \approx 0.292$ and $e \approx 0.412$ for the raw dataset, and $n \approx 0.287$ and $e \approx 0.403$ for the cleaned dataset. These values were then used in the Aubertin model to provide a physically based predictive reference curve tied to the wet-end behaviour of the field data.

The predictive Aubertin curve does not exactly coincide with the van Genuchten fit, particularly at higher suction where it predicts a broader decrease in water content than is observed in the cleaned field branch. This difference is physically reasonable. The van Genuchten model is fitted directly to the measured field data, whereas the Aubertin model provides an idealized estimate derived from soil properties and porosity. Therefore, the Aubertin curve should be interpreted as a soil-informed predictive envelope, while the van Genuchten fit represents the measured dominant branch more closely.

Overall, the combined GP5 figure shows that the cleaned dataset defines a well-structured and physically interpretable field-derived retention branch at this depth. The figure also shows that the use of a porosity-based void ratio provides a physically consistent basis for the Aubertin comparison at low suction, while the remaining differences between the predictive and fitted curves reflect the distinction between an idealized model and the actual in-situ field response.

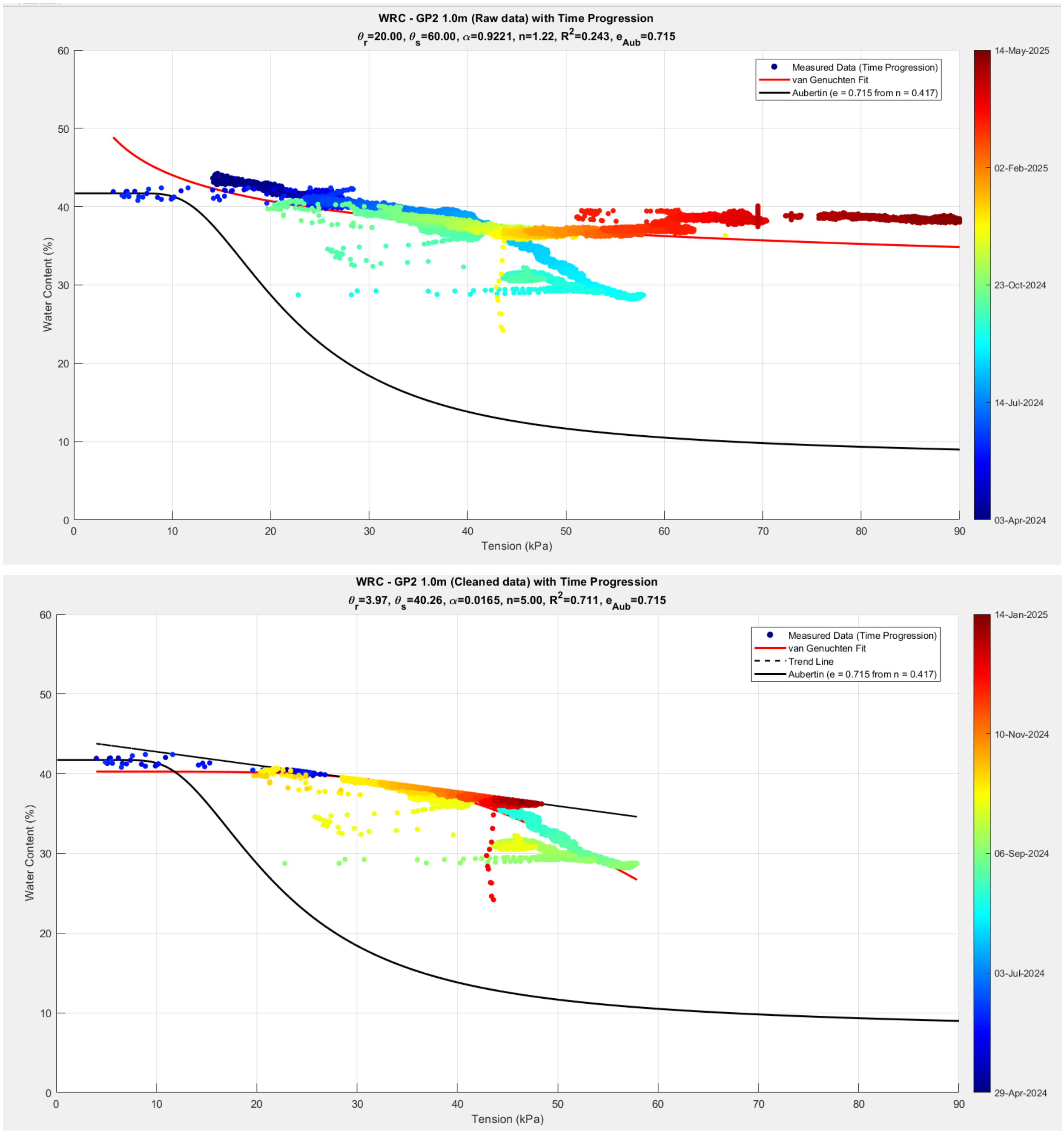

Figure 7.21 Field-derived water retention plots for the GP2 sensor pair at 1.0 m depth: raw matched data (top) and cleaned data (bottom), coloured by time progression and fitted with the van Genuchten model. The Aubertin-based predictive WRC is shown using a field-informed void ratio derived from the estimated low-suction porosity.

For the sensor pair at GP2, depth 1.0 m, the water retention correlation was evaluated using both the raw matched tension–humidity dataset and the corresponding cleaned dataset. In the raw dataset, the measured points are widely scattered and distributed across several temporal clusters, indicating that the field correlation does not follow a single well-defined retention branch. This behaviour is reflected in the relatively weak van Genuchten fit ($R^2 = 0.243$), which suggests that the untreated data include substantial variability associated with seasonal transitions, path dependence, and possible mismatch between paired sensor responses.

After cleaning and filtering, the retained data define a narrower and more coherent branch, and the van Genuchten fit improves to $R^2 = 0.711$. Although some spread is still visible, the cleaned dataset better captures the dominant field response, with water content generally decreasing as tension increases. The time colouring also shows a more orderly progression through the retained branch, indicating that the cleaned data provide a more interpretable representation of the seasonal retention behaviour than the raw cloud.

The Aubertin-based predictive curve was computed using a field-informed porosity estimate derived from the low-suction end of the observed data. Following the physical interpretation of the model, the volumetric water content at very low suction was treated as an estimate of the porosity, n, corresponding to near-saturated conditions, and the associated void ratio was then calculated as $e = n/(1 - n)$. For GP2, this procedure yielded $n \approx 0.417$ and $e \approx 0.715$, which were then used in the Aubertin model. This provides a physically based predictive reference curve tied to the wet-end behaviour of the field data.

The predictive Aubertin curve does not coincide exactly with the van Genuchten fit, especially away from the wet end, and this is physically reasonable. The van Genuchten model is fitted directly to the measured field branch, whereas the Aubertin model provides an idealized estimate derived from soil properties and porosity. Therefore, the Aubertin curve should be interpreted as a soil-informed predictive envelope, while the van Genuchten fit represents the measured dominant branch more closely.

Overall, the combined GP2 figure shows that the field-derived water retention relationship at this depth is only moderately coherent, with the cleaned dataset defining the most interpretable branch. The figure also shows that the use of a porosity-based void ratio provides a physically consistent basis for the Aubertin comparison at low suction, while the remaining differences between the predictive and fitted curves reflect the distinction between an idealized model and the actual in-situ field response.

7.5.4 Fitted parameter summary

Table 7.5 reports the cleaned van Genuchten parameters for the analysed sensor pairs. The cleaned fits are emphasized because they are considered more representative of the actual retention behaviour after the quality-control and branch-selection procedure. Together with Table 7.6, they provide a concise summary of both fit quality and fitted curve shape.

Table 7.6 reports the fitted van Genuchten parameters for the WRC analysis, comparing the fits using the full dataset (Raw data) and the cleaned dataset..

Sensor pair	**All data**						**Cleaned data**					
Sensor pair	**θ_r**	**θ_s**	**α**	**n**	**m**	**R^2**	**θ_r**	**θ_s**	**α**	**n**	**m**	**R^2**
GP2@1.0m	20.00	60.00	0.9221	1.22	0.18	0.243	3.97	40.26	0.0165	5.00	0.80	0.711
GP5@1.5m	14.99	29.74	0.0681	1.30	0.23	0.557	14.99	28.76	0.0338	1.54	0.35	0.925
GP8@0.5m	15.00	39.18	0.0169	3.95	0.75	0.292	15.00	38.09	0.1159	1.34	0.26	0.993
GP8@1.0m	0.00	28.94	0.0781	1.42	0.29	0.701	0.00	25.00	0.0674	1.34	0.26	0.896

Based on the paired-sensor WRC plots, the cleaning strategy (Chapter 5) and the adopted usable windows (Table 7.5) substantially improve the coherence between tension and moisture signals:

- GP2 (1.0 m): the fit quality increases from $R^2 \approx 0.243$ (all data) to $R^2 \approx 0.711$ after cleaning, indicating that outliers/anomalous periods were masking an otherwise consistent drying–rewetting behaviour.
- GP5 (1.5 m): the cleaned dataset provides a very good fit ($R^2 \approx 0.925$) compared to the all-data fit ($R^2 \approx 0.557$). The time-coloured scatter suggests seasonal progression along the main retention branch, while discontinuities/spikes correspond to the excluded windows.
- GP8 (1.0 m): the fit improves from $R^2 \approx 0.701$ to $R^2 \approx 0.896$ after cleaning, showing a stable inverse relationship (higher suction with lower water content).

Overall, the time progression colouring highlights that the sensor pairs follow a seasonal wetting–drying cycle; deviations from the main trend (loops, clusters, or vertical ‘spikes’) are interpreted as either hysteresis (physical) or sensor artefacts (non-physical), and are treated accordingly in the QC workflow.

7.6 Physical interpretation and discussion

The seasonal behaviour observed across the monitoring network is quantitatively consistent with the environmental forcing data presented in Figures 7.2 and 7.3. Monthly rainfall indicates a relatively dry summer phase in **July–August 2024** (minimum monthly rainfall in July and low values in August), followed by a wetter and more variable period from **September–October 2024 onward**, with major rainfall peaks in **December 2024** and **January 2025**. The hydrometric series at Latisana 1 shows the same general seasonal structure, with lower mean river levels in summer and stronger monthly maximum peaks during the wet season. The sensor responses therefore show a physically meaningful seasonal cycle: **decreasing humidity and/or increasing tension during summer**, followed by **autumn rewetting** and **winter stabilization**. However, the amplitude and clarity of this response vary substantially between stations, depths, and sensor types.

A first quantitative distinction is between sensors with **large seasonal amplitude** and sensors with **buffered response**. For tension, the clearest example is **GP2T1.0**, whose monthly mean values increase from about **21 kPa in April 2024** to about **49 kPa in September 2024**, and continue increasing to about **93 kPa by May 2025**, indicating both a strong seasonal response and a long-term upward trend. In contrast, **GP2T0.5** remains nearly constant around **−16 kPa**, with a monthly amplitude of only about **2 kPa**, while **GP2T1.5** varies from about **10 to 31 kPa** (amplitude ≈ **21 kPa**). At GP5, **GP5T1.5** varies from about **2 to 40 kPa** (amplitude ≈ **38 kPa**), whereas **GP5T4.0** remains in a much narrower negative range (about **−30 to −20 kPa**, amplitude ≈ **10 kPa**). At GP8, **GP8T1.0** ranges from about **20 to 61 kPa** (amplitude ≈ **41 kPa**), while **GP8T0.5** shows a mixed behaviour with a sharp summer peak followed by a strong drop, consistent with segmented or reset-affected response. These values confirm that seasonal damping is not only qualitative: in the most coherent tension profiles, the deeper or more buffered sensors show substantially smaller amplitude than the more reactive intermediate/shallow ones.

The humidity records show the same seasonal structure but in the opposite direction: **higher summer suction corresponds to lower water content**, and rewetting from autumn onward produces humidity recovery. The boxplots and descriptive statistics confirm this quantitatively. For Humidity-H, the highest mean values are recorded at **GP5H4.0 (42.47%)**, **GP8H0.5 (38.83%)**, and **GP2H1.0 (38.16%)**, whereas the lowest mean is observed at **GP8H1.0 (19.30%)**. For Humidity-V, the wettest station overall is GP6, with **GP6V0.5 = 37.76%** and **GP6V2.0 = 36.81%**, while the lowest means occur at **GP4V0.5 = 23.03%** and **GP3V1.0 = 23.16%**. The variability also differs significantly: for example, **GP4V1.0** has the largest standard deviation among V sensors (**6.63%**), whereas **GP3V1.5** and **GP4V2.0** are much more stable (**1.10%** and **1.27%**, respectively). For Humidity-H, the most variable sensors are **GP8H0.5 (Std = 5.10%)** and **GP7H1.0 (Std = 4.62%)**, while **GP2H3.5 (Std = 0.68%)** and **GP5H2.5 (Std = 0.75%)** are comparatively stable.

7.6.1 Drying phase: late spring–summer 2024

The drying phase is best identified between **June and September 2024**, when rainfall is reduced and mean river level remains relatively low. In this period, the tension sensors show systematic increase in suction magnitude at the most responsive depths. At GP2, **GP2T1.0** increases by about **28 kPa** between April and September (from ~21 to ~49 kPa), while **GP2T1.5** increases by about **21 kPa** (from ~10 to ~31 kPa). At GP5, **GP5T1.5** increases from about **3 to 40 kPa**, which is the clearest summer drying signal at that station. At GP8, **GP8T1.0** rises from about **23 to 61 kPa** by September, indicating strong drying before the autumn transition. These changes are too large and too coherent across multiple stations to be attributed to noise alone.

The humidity sensors show the complementary response. In the Humidity-H group, several sensors reach their seasonal minima around **August–September 2024**. The strongest drops are seen in **GP7H1.0** (from about **35.5% to 20.0%**, amplitude ≈ **15.5%**) and **GP8H0.5** (from about **42% to 27%**, amplitude ≈ **15%**). In the Humidity-V arrays, the strongest summer drying occurs at **GP4**, especially at **1.0 m**, where the monthly mean falls from nearly **39.5% in June** to about **16.3% in September** (amplitude ≈ **23%**). At GP3, the seasonal amplitudes are smaller: about **9.5%** at **0.5 m**, **6.2%** at **1.0 m**, **4.2%** at **1.5 m**, and **5.0%** at **2.0 m**. At GP6, the amplitudes are about **15.7%**, **9.0%**, **7.1%**, and **8.4%** from **0.5 to 2.0 m**, respectively. These values confirm that the summer drying phase is strongest at selected shallow to intermediate depths and weaker in deeper or more buffered positions.

7.6.2 Transition and rewetting: autumn 2024

The autumn transition occurs mainly between **September and November 2024**, coinciding with the rise in rainfall and the increase in river-stage variability. In the tension data, this transition appears as a clear decrease or stabilization after the summer maxima. At GP5, **GP5T1.5** drops from about **40 kPa in September** to about **22 kPa in October**, consistent with rapid rewetting. At GP8, **GP8T1.0** decreases from about **61 kPa in September** to about **31 kPa in October**, while **GP8T0.5** shifts from strongly positive values to negative values over the same interval, indicating a pronounced change in shallow conditions. At GP2, the transition is more moderate, with **GP2T1.5** decreasing from about **31 to 19 kPa** and **GP2T1.0** dropping from about **49 to 36 kPa** around October. These values quantitatively support the interpretation of autumn rewetting and reduced suction.

The humidity series show the same transition in the opposite direction. In the Humidity-H data, several sensors recover by about **2–8 percentage points** from their late-summer minima toward autumn and winter values. In the Humidity-V data, the recovery is particularly clear in the GP4 profile, where the **0.5 m** sensor rises from about **14% in August** to about **22–24% in October–November**, and the **1.0 m** sensor rises from about **16–18%** to about **26%** over the same period. At GP3 and GP6, the rewetting signal is also visible but smoother, indicating less abrupt moisture redistribution. This confirms that autumn rewetting is not only visible qualitatively but can be measured as a clear reversal in the seasonal trajectories of both tension and humidity.

7.6.3 Winter stabilization and spring 2025 evolution

During **winter 2024–2025**, many sensors enter a more stable regime, with smaller month-to-month fluctuations than during the summer and autumn transition periods. This is visible in both the time-series plots and the boxplots, where several sensors show relatively narrow interquartile ranges. For example, **GP2H3.5** has a very small standard deviation (**0.68%**) and **GP5H2.5** also remains highly stable (**Std = 0.75%**), indicating weak seasonal variability after the main transition. In the tension data, **GP5T4.0** remains one of the most stable sensors (**Mean = −24.26 kPa; Std = 3.34 kPa**), and **GP2T0.5** also shows very limited variability (**Std = 1.03 kPa**). These sensors behave as buffered references compared with the more responsive sensors.

Spring 2025 shows two different tendencies. Some sensors continue the wet-season stabilization, while others begin to move again toward renewed drying or redistribution. The clearest example is **GP2T1.0**, which continues to increase after winter and reaches its highest monthly mean value

(**~93 kPa**) by **May 2025**, suggesting either strong delayed seasonal response, persistent drying tendency, or possible long-term drift superimposed on the seasonal signal. In contrast, several humidity sensors show mild recovery or slight wetting from late winter to spring. For example, the GP6V profile remains overall wet and relatively stable, with **GP6V0.5** and **GP6V2.0** staying near **38–39%** by spring 2025, while GP4 and GP3 show more modest spring increases. Thus, winter and spring do not represent a single uniform regime: they combine stable periods, delayed recovery, and in some cases renewed divergence between sensors.

7.6.4 Quantitative depth effect and station contrasts

A central result of Chapter 7 is that the seasonal signal exhibits **quantitative depth-dependent damping**, but the effect is not identical at all stations. In the tension data, the clearest damping appears at **GP2**, where the amplitude is approximately **72 kPa** at **1.0 m**, **21 kPa** at **1.5 m**, and only **~2 kPa** at **0.5 m**. At **GP5**, the amplitude is about **38 kPa** at **1.5 m** and only **10 kPa** at **4.0 m**, while the **2.5 m** sensor shows a non-smooth shift that is better interpreted as a segmented or reset-affected response. At **GP8**, the **1.0 m** sensor shows an amplitude of about **41 kPa**, whereas the **0.5 m** sensor is affected by a strong discontinuity and is therefore less suitable for direct seasonal comparison.

In the Humidity-V arrays, depth effects can also be quantified. At **GP3**, the seasonal amplitude generally decreases from shallow to deeper sensors (about **9.5% at 0.5 m**, **6.2% at 1.0 m**, **4.2% at 1.5 m**, and **5.0% at 2.0 m**), indicating moderate damping with depth. At **GP4**, the profile is more heterogeneous: **1.0 m** shows the largest amplitude (**~23%**), larger than both **0.5 m (~13%)** and **2.0 m (~4%)**, suggesting that the strongest seasonal response is concentrated at an intermediate depth rather than simply at the shallowest level. At **GP6**, the amplitudes are again lower than at GP4 and more regular with depth (**~16%, 9%, 7%, and 8%** from **0.5 to 2.0 m**). The Humidity-H sensors also show strong contrasts between stations and depths, but because they are not organized as full vertical arrays, the most useful quantitative metrics are their means and standard deviations rather than depth-sequence amplitudes. For example, **GP5H4.0** and **GP8H0.5** are among the wettest H sensors, whereas **GP8H1.0** is consistently the driest; **GP8H0.5** and **GP7H1.0** are also the most variable. Overall, these quantitative comparisons confirm that depth matters, but the response is also strongly controlled by local position, soil heterogeneity, and sensor-specific hydraulic context.

7.7 Chapter summary

This chapter analysed the seasonal evolution of the cleaned monitoring dataset by combining monthly aggregation, station/depth comparison, and paired tension–humidity interpretation. The integration of the environmental forcing variables showed that the observed sensor responses are consistent with the hydro-climatic conditions during the study period: a relatively dry summer phase in 2024, followed by autumn rewetting and a wetter winter–spring period. The monthly tension, Humidity-H, and Humidity-V series confirmed that the seasonal signal is physically meaningful, although its magnitude and clarity vary across stations and depths.

For tension, the strongest seasonal responses were observed in selected shallow to intermediate sensors, while deeper sensors generally showed more buffered behavior and lower variability. The station-based plots highlighted clear differences between GP2, GP5, and GP8, including cases of coherent seasonal response as well as cases requiring cautious interpretation due to segmented or reset-affected behavior. The descriptive statistics and boxplots supported these interpretations quantitatively by showing differences in mean values, spread, and outlier structure among sensors.

For humidity, the combined interpretation of H and V sensors showed a coherent drying–rewetting pattern over the study period, with minima generally occurring in late summer and recovery beginning in autumn. The Humidity-V profiles provided particularly useful evidence of depth-dependent damping and time lag, while the Humidity-H sensors highlighted persistent spatial contrasts in moisture regime and variability. The statistical summaries confirmed that some stations remained consistently wetter than others, and that variability differs markedly between sensors, reflecting the combined effects of depth, local stratigraphy, hydraulic position, and sensor performance.

The chapter also used paired tension–humidity datasets to derive empirical water-retention relationships using the van Genuchten model. By comparing raw-data and cleaned-data fits for representative sensor pairs, it was shown that the preprocessing strategy substantially improves the physical coherence of the correlation and the quality of the fit. The cleaned-data approach, including threshold- and trend-based filtering, provided a more robust representation of the dominant retention branch and made the fitting workflow transparent and reproducible.

Overall, Chapter 7 demonstrates that the seasonal response of the monitored levee is controlled by both environmental forcing and local subsurface heterogeneity. The results confirm the importance of combining QC-based data screening, monthly aggregation, quantitative comparison, and physically based interpretation in order to distinguish meaningful hydrological signals from instrument-related artefacts. These findings provide the basis for the final conclusions of the thesis and for future work aimed at linking seasonal sensor response more explicitly to levee stratigraphy and hydraulic boundary conditions.

Chapter 8 Conclusions and Recommendations

8.1 General conclusions

This thesis investigated the hydro-mechanical behaviour of the San Giorgio principal levee section through an integrated analysis combining literature review, site characterization, laboratory investigations, quality control of monitoring data, and seasonal interpretation of field measurements. The work was developed with the objective of improving the understanding of how suction/tension and water content evolve in a monitored river embankment under natural hydraulic and climatic forcing, and of evaluating how data quality affects the interpretation of such behaviour. The adopted workflow moved progressively from the general theoretical framework of unsaturated embankment response, to the local stratigraphic and material characterization of the San Giorgio site, and finally to the analysis of monitored seasonal signals and field-derived water retention behaviour.

Overall, the thesis demonstrates that the monitored levee response cannot be interpreted reliably from raw sensor outputs alone. Meaningful physical interpretation requires the integration of four complementary elements: (i) an understanding of embankment behaviour under transient hydraulic and climatic forcing, (ii) a site-specific stratigraphic and material framework, (iii) a rigorous quality-control procedure to distinguish real behaviour from instrumental artefacts, and (iv) quantitative seasonal comparison of validated tension and humidity records. When these elements are combined, the San Giorgio monitoring dataset reveals a coherent drying–rewetting behaviour governed by environmental forcing, modulated by depth, local stratigraphy, and sensor location.

8.2 Main findings of the thesis

8.2.1 Findings from the literature framework

The literature review confirmed that levee behaviour is strongly influenced by transient seepage processes, unsaturated soil mechanics, and the combined action of river-stage fluctuations and climatic forcing. In particular, the reviewed studies highlighted the importance of suction in controlling effective stress and shear strength, the central role of the Soil–Water Retention Curve (WRC) in linking suction and water content, and the need to integrate monitoring, laboratory characterization, and modelling when analysing embankment performance. The review also identified clear research needs related to data quality, long-term monitoring interpretation, and the integration of field observations with physically based frameworks. These ideas provided the conceptual basis for the present work.

8.2.2 Findings from site characterization and stratigraphic interpretation

The study area analysis showed that the San Giorgio principal station represents a suitable field-scale case for investigating monitored levee behaviour under natural forcing. The levee body and shallow foundation are mainly composed of sandy to silty-sandy materials, while the deeper profile includes a transition toward coarser fluvial deposits. By combining borehole SA1 with CPTG1 and CPTE1 and the updated levee geometry, a five-unit correlated stratigraphic model was established. This model includes a thin topsoil cover, an upper silty sand / sand-mixture unit forming much of the levee body, a local finer interlayer beneath the crest, a lower mixed sandy foundation unit, and a deeper coarse fluvial foundation. This stratigraphic interpretation is important because it explains why the monitored response is not uniform across the section: permeability contrasts, lateral heterogeneity, and the presence of the finer lens can influence infiltration, retention, drainage, and the timing of the seasonal signal.

8.2.3 Findings from laboratory investigations and soil classification

The laboratory program, based on 61 samples from the San Giorgio area, showed that the investigated soils are predominantly silty to sandy-silty materials with local variability in the proportion of fine sand and silt. Grain-size distribution curves indicated that the materials do not belong to a single uniform soil type, but rather to a heterogeneous succession of fine-dominated and mixed soils. A smaller subset of 11 samples exhibited plastic behaviour and was tested for Atterberg limits; these samples were found to fall within the low-plasticity range, with behaviour consistent mainly with ML soils. Therefore, the laboratory evidence supports the interpretation of the monitored materials as generally low-plasticity, fine-dominated to mixed silty–sandy soils rather than highly plastic clays.

The laboratory-based hydraulic interpretation, developed using the Aubertin predictive framework for representative samples, further indicated that the selected San Giorgio soils exhibit retention behaviour consistent with silty to sandy-silty materials. The predictive WRCs suggested that finer or ML-type soils retain water over a wider suction range than more sandy materials, while also showing sensitivity to assumed void ratio. Although these curves were not direct suction-controlled laboratory measurements, they provided a useful first-order hydraulic characterization and helped place the later field-derived WRC discussion within a broader material context.

8.2.4 Findings from the QC methodology and monitoring-data treatment

A central contribution of this thesis is the structured QC workflow applied to the monitoring dataset before any physical interpretation. The monitoring records, covering April 2024 to May 2025, included tension and volumetric water content measurements at multiple depths, but the raw data were affected by anomalies such as spikes, resets, flatlines, and unrealistic values. The adopted methodology combined visual inspection, rule-based screening, anomaly logging, replacement of invalid values, and classification of sensor reliability. Invalid data were replaced with missing-value labels in order to preserve the time axis while preventing biased statistics. Monthly means and subsequent analyses were then computed only from valid observations.

This workflow showed that sensor reliability varies substantially across the network. Some sensors displayed stable and physically coherent behaviour and could be treated as reliable references, while others required segmentation or partial exclusion due to resets, spikes, or loss of responsiveness. In particular, the results showed that not all monitored series are equally suitable for seasonal analysis, and that the distinction between reliable, partially reliable, and unreliable sensors is essential for defensible interpretation. The QC results therefore demonstrate that quality assessment is not a secondary processing step but a necessary foundation for any hydro-mechanical interpretation of long-term levee monitoring data.

8.2.5 Findings from sensor performance evaluation

The sensor-by-sensor performance assessment confirmed that the most recurrent problems in the network are spikes/outliers, step-change discontinuities, flatline behaviour, and local unrealistic values. Tension sensors were particularly affected by spike episodes, reset-like behaviour, and flatline periods, whereas humidity sensors more commonly showed offsets, discontinuities, or short segments requiring separate interpretation. At the same time, the network also included sensors with sufficiently coherent behaviour to support a robust seasonal analysis. This distinction made it possible to retain useful information from partially reliable sensors while excluding intervals that would otherwise distort the physical interpretation.

An important conclusion of this stage is that the monitoring system remains valuable even when some sensors exhibit limitations, provided that the dataset is processed critically and interpreted through validated time windows only. Rather than discarding the monitoring system as a whole, the thesis shows that a filtered and classified use of the records allows meaningful seasonal signals to be extracted from the network.

8.2.6 Findings from seasonal analysis and environmental forcing

The seasonal analysis of the cleaned dataset showed a coherent annual cycle across much of the monitored network. The combined interpretation of monthly rainfall, river-stage/hydrometric variability, tension, and humidity demonstrated that the monitored levee underwent a relatively dry phase during late spring and summer 2024, followed by a transition and rewetting phase in autumn 2024, and then a wetter and more stable winter–spring regime. This seasonal evolution was visible in both tension and humidity records, although with different amplitudes and degrees of clarity depending on location, depth, and sensor quality.

For the tension sensors, the strongest seasonal responses were generally observed in shallow to intermediate depths, while deeper sensors showed more buffered and less variable behaviour. A representative example is GP2, where the seasonal amplitude clearly decreased with depth, indicating depth-dependent damping of the hydro-climatic signal. Similar behaviour was observed in the humidity data: the Humidity-H and Humidity-V sensors showed a drying phase with late-summer minima, followed by recovery from autumn onward. The vertical arrays in particular provided useful evidence of attenuation and time lag with depth, confirming that shallower sensors respond faster and more strongly, whereas deeper sensors are more buffered.

The results also showed that the depth effect is not spatially uniform. Some stations presented stronger damping with depth, while others showed more heterogeneous behaviour, implying that local stratigraphy, hydraulic connectivity, and position within the levee section influence the response in addition to depth alone. In this sense, the monitoring results are consistent with the stratigraphic interpretation of the site as a laterally variable system containing both more permeable sandy units and finer, more retentive interlayers.

8.2.7 Findings from field-derived water retention analysis

The paired tension–humidity analysis showed that empirical field-derived WRC relationships can be extracted from the monitoring data, but only after careful cleaning and selection of representative data windows. The application of the van Genuchten model to co-located sensor pairs demonstrated that raw data often produce highly scattered and physically inconsistent relationships due to anomalies, branch mixing, and non-representative periods. After QC-based cleaning and filtering, the fitted relationships became significantly more coherent, and the agreement between tension and humidity improved markedly.

This result has two important implications. First, it confirms that the coupling between suction/tension and water content is physically present in the field data and can be exploited to derive meaningful retention trends. Second, it shows that the reliability of this type of interpretation depends strongly on preprocessing. The field-derived curves should therefore be considered as empirical retention relationships reflecting both soil behaviour and field conditions, rather than direct equivalents of laboratory SWRC measurements. Nevertheless, they provide valuable support for understanding how local material properties and environmental forcing combine to shape the observed seasonal response.

8.3 Main contribution of the thesis

The main contribution of this thesis lies in the development of an integrated and reproducible framework for interpreting monitored levee behaviour at the San Giorgio principal station. Rather than treating laboratory characterization, monitoring interpretation, and water-retention analysis as separate exercises, the work combines them into a single workflow that links material properties, site stratigraphy, sensor quality, environmental forcing, and seasonal response. This integrated structure helps bridge the gap between theoretical unsaturated-soil concepts and the practical difficulties of interpreting real field data.

A second important contribution is methodological. The thesis shows that long-term levee monitoring data can only support robust hydro-mechanical interpretation when a clear QC framework is applied first. The anomaly classification, traceable anomaly table, replacement strategy for invalid data, and final sensor reliability classes together provide a transparent basis for deciding which data can be used and how. This is particularly relevant in practical monitoring programs, where the presence of spikes, resets, flatlines, and offsets may otherwise lead to misleading conclusions.

A third contribution is interpretative. The seasonal analysis confirms that the monitored levee response at San Giorgio is governed by a combination of hydro-climatic forcing and local heterogeneity. The results demonstrate quantitatively that the seasonal signal is generally stronger in shallow zones and more damped at depth, while also showing that local station contrasts remain significant. This provides a field-based demonstration of how unsaturated-zone processes, stratigraphic variability, and hydraulic boundary conditions interact in a monitored embankment.

8.4 Limitations of the study

Despite the useful results obtained, several limitations should be acknowledged. First, the detailed interpretation developed in this thesis is focused mainly on the San Giorgio principal station. Although this focus allows a more coherent and site-specific analysis, it also means that the conclusions are not automatically generalizable to all monitored stations without additional comparison.

Second, the monitoring interpretation is affected by variable sensor performance. Some time series are complete and physically coherent, whereas others require segmentation or partial exclusion due to anomalies. This means that the seasonal analysis is based on a validated subset of the available data rather than on the entirety of the raw monitoring record. While this is a strength from the point of view of reliability, it also limits the continuity of interpretation for some sensor locations and depths.

Third, the field-derived WRC interpretation remains empirical. The fitted van Genuchten relationships are based on monitored tension–humidity pairs and therefore reflect not only intrinsic material behaviour, but also hysteresis, seasonal cycling, sensor characteristics, and local field conditions. Similarly, the Chapter 4 Aubertin-based WRCs are predictive estimates rather than direct laboratory measurements, and they depend on assumed void ratios and model assumptions. For these reasons, both the predictive and field-derived WRC results should be interpreted as support for hydraulic understanding rather than as definitive calibration curves.

Finally, the thesis does not develop a full numerical seepage or stability model calibrated against the monitoring data. The results therefore provide a physically based interpretation of the monitored behaviour, but not a complete predictive modelling framework for future scenarios or factor-of-safety evolution. Such modelling would represent a natural extension of the work.

8.5 Recommendations for future work

Future research should first extend the integrated workflow developed here to other monitored sections of the levee system in order to evaluate whether the same depth-dependent and station-dependent patterns are observed outside the San Giorgio principal station. A comparative analysis among stations would help distinguish site-specific behaviour from broader embankment-scale tendencies.

Second, the monitoring system would benefit from continued maintenance, recalibration, and targeted replacement of problematic sensors. The QC results identified specific recurring failure modes, such as flatline behaviour, resets, and spike-prone records. Reducing these problems in future data acquisitions would improve continuity and reduce the need for segmentation and exclusion in subsequent analyses.

Third, the relationship between stratigraphy and seasonal sensor response should be explored more explicitly. The present thesis already shows that local heterogeneity is important, but future work could quantify more directly how the finer interlayer, the mixed sandy units, and the deeper coarse foundation affect infiltration pathways, retention capacity, and response timing. This could be done by coupling the existing monitoring data with more detailed hydraulic interpretation or numerical seepage modelling.

Fourth, future studies should compare field-derived WRC behaviour with direct laboratory suction-controlled retention tests on representative samples. Such a comparison would help distinguish the influence of intrinsic material properties from field effects such as hysteresis, seasonal branch selection, and sensor-related uncertainty. It would also strengthen the use of monitoring data for hydraulic parameter estimation.

Finally, the seasonal framework established in this thesis could be expanded toward predictive analysis by integrating the validated monitoring results with transient numerical modelling. This would make it possible to test how the levee may respond under different rainfall sequences, river-stage fluctuations, or combined wet antecedent conditions, and would represent a valuable step toward practical flood-risk and embankment-management applications.

8.6 Final concluding statement

In conclusion, this thesis has shown that the hydro-mechanical response of the San Giorgio principal levee section can be interpreted meaningfully only through an integrated approach combining site characterization, laboratory evidence, rigorous QC of monitoring data, and seasonal comparison of validated tension and humidity records. The results confirm that the monitored levee exhibits a physically coherent drying–rewetting behaviour driven by hydro-climatic forcing, but strongly modulated by depth, local heterogeneity, and sensor reliability. The work therefore contributes both a practical interpretation of the San Giorgio monitoring dataset and a methodological framework for transforming imperfect long-term field records into defensible engineering understanding.

References

Aubertin, M., Mbonimpa, M., Bussière, B., & Chapuis, R. P. (2003). A model to predict the water retention curve from basic geotechnical properties. *Canadian Geotechnical Journal*, *40*(6), 1104–1122. https://doi.org/10.1139/t03-054

Cola, S. (n.d.). *Towards a better understanding and monitoring of levees behaviour to mitigate flooding risks*.

Gragnano, C. G., Rocchi, I., & Gottardi, G. (2021). Field Monitoring and Laboratory Testing for an Integrated Modeling of River Embankments under Transient Conditions. *Journal of Geotechnical and Geoenvironmental Engineering*, *147*(9), 05021006. https://doi.org/10.1061/(ASCE)GT.1943-5606.0002571

Rocchi, I., Gragnano, C. G., Govoni, L., Bittelli, M., & Gottardi, G. (2020). Assessing the performance of a versatile and affordable geotechnical monitoring system for river embankments. *Physics and Chemistry of the Earth, Parts A/B/C*, *117*, 102872. https://doi.org/10.1016/j.pce.2020.102872

Spaliviero, M. (2003). Historic fluvial development of the Alpine-foreland Tagliamento River, Italy, and consequences for floodplain management. *Geomorphology*, *52*(3–4), 317–333. https://doi.org/10.1016/S0169-555X(02)00264-7

Appendices

Appendix 3.A – Monitoring system details: installed sensors by station

Appendix 3.A.1 Bevazzana principal station (BP)

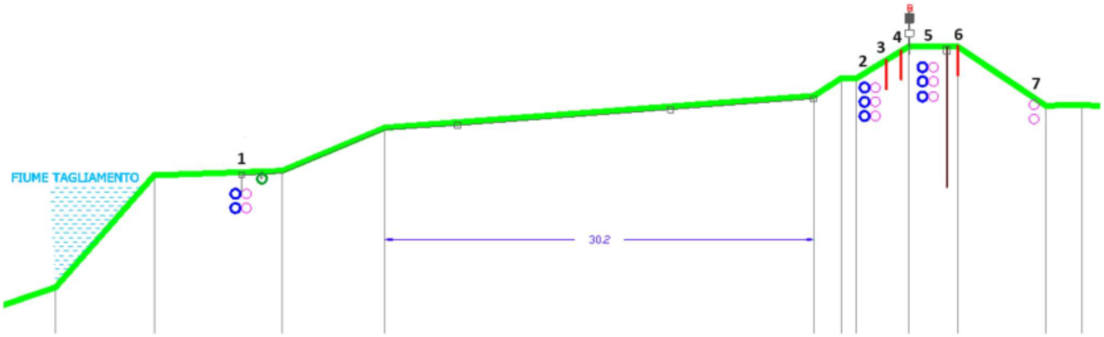

I codici dei sensori sono:

- T per i tensiometri
- H per gli igrometri
- V per gli igrometri organizzati in verticali

Tutti i sensori tranne la verticale in posizione 4 della stazione principale di Bevazzana sono stati installati con sigillatura superiore in bentonite ed è stato eseguito un test della buona riuscita della sigillatura bagnando ripetutamente le verticali 3 (con sigillatura) e 4 (senza sigillatura) e mettendo poi a confronto i dati. È stato inoltre osservato che i sensori non reagiscono a piogge di lieve entità dimostrando che la sigillatura impedisce che il cavo costituisca una via preferenziale di arrivo dell'acqua al sensore.

Attualmente le stazioni spediscono solo sulla piattaforma di backup online e vengono memorizzati nella memoria interna dei data logger in loco. Parte dei dati sono stati forniti all'università di Padova per una prima fase di collaudo.

- Pluviometro
- Piezometro I1-B1
- Piezometro I1-B1 MOD

Gruppo 1 - BP1T1.5 - BP1T2.5 - BP1H1.5 - BP1H2.5	Gruppo 2 - BP1T0.5 - BP1T1 - BP1T1.5 - BP1H0.5 - BP1H1 - BP1H1.5	Gruppo 3 - BP3V0.5 - BP3V1 - BP3V1.5 - BP3V2
Gruppo 4 - BP4V0.5 - BP4V1 - BP4V1.5 - BP4V2	Gruppo 5 - BP5T4 - BP5T2.5 - BP5T1.5 - BP5H4 - BP5H2.5 - BP5H1.5	Gruppo 6 - BP6V0.5 - BP6V1 - BP6V1.5 - BP6V2
Gruppo 7 - BP7H0.5 - BP7H1		

Appendix 3.A.2 Bevazzana south station (BS)

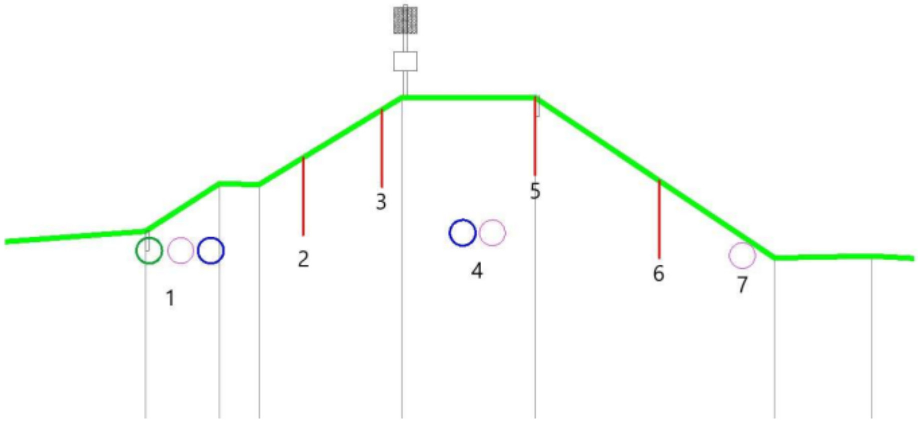

Sensori installati:

Gruppo 1 - BS1T1 - BS1H1	Gruppo 2 - BS2V0.5 - BS2V1 - BS2V1.5 - BS2V2	Gruppo 3 - BS3V0.5 - BS3V1 - BS3V1.5 - BS3V2
Gruppo 4 - BS4T4 - BS4H4	Gruppo 5 - BS5V0.5 - BS5V1 - BS5V1.5 - BS5V2	Gruppo 6 - BS6V0.5 - BS6V1 - BS6V1.5 - BS6V2
Gruppo 7 - BS7H1		

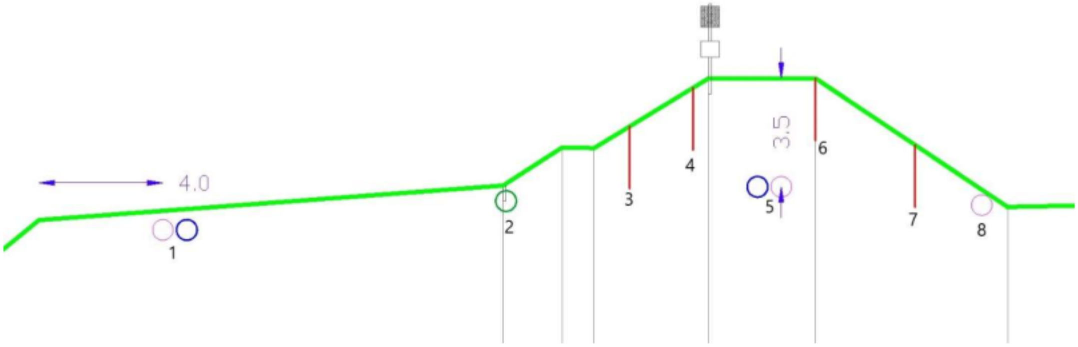

Sensori installati

Gruppo 1 - BN1T1 - BN1H1	Gruppo 3 - BN3V0.5 - BN3V1 - BN3V1.5 - BN3V2	Gruppo 4 - BN4V0.5 - BN4V1 - BN4V1.5 - BN4V2
Gruppo 5 - BN5T4 - BN5H4	Gruppo 6 - BN6V0.5 - BN6V1 - BN6V1.5 - BN6V2	Gruppo 7 - BN7V0.5 - BN7V1 - BN7V1.5 - BN7V2
Gruppo 8 - BN8H1		

Appendix 3.A.3 Bevazzana north station (BN)

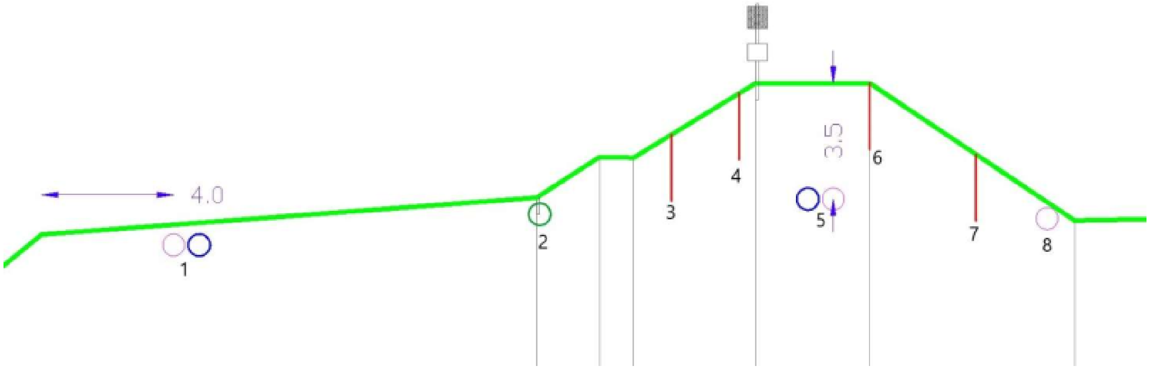

Sensori installati

Gruppo 1 - BN1T1 - BN1H1	Gruppo 3 - BN3V0.5 - BN3V1 - BN3V1.5 - BN3V2	Gruppo 4 - BN4V0.5 - BN4V1 - BN4V1.5 - BN4V2
Gruppo 5 - BN5T4 - BN5H4	Gruppo 6 - BN6V0.5 - BN6V1 - BN6V1.5 - BN6V2	Gruppo 7 - BN7V0.5 - BN7V1 - BN7V1.5 - BN7V2
Gruppo 8 - BN8H1		

Appendix 3.A.4 San Giorgio principal station (GP)

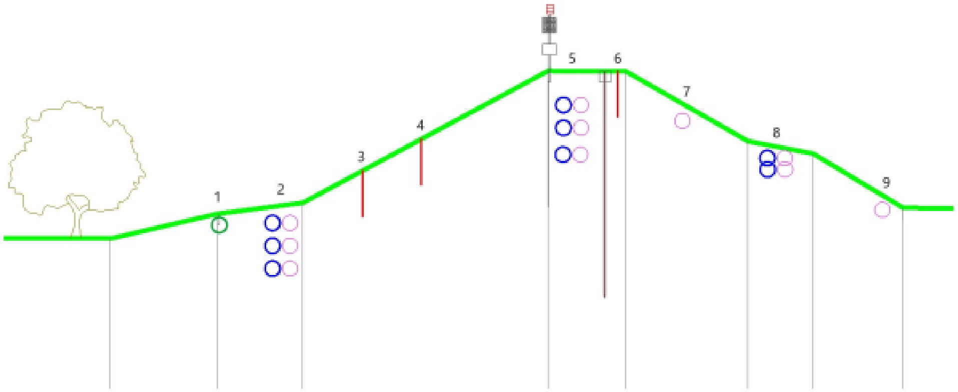

Nella stazione principale denominata San Giorgio sono installati:

- Pluviometro
- Piezometro I1-B1 (a piede argine verso il fiume)
- Piezometro I1-B1 MOD (spostato a 30 m circa dalla stazione verso la stazione principale NORD)

Gruppo 1 - Sensore di livello in pozzetto I1-B1	Gruppo 2 (cambiate rispetto a progetto per presenza di acqua a poca profondità tranne un igrometro a 3.5m) - GP2T0.5 - GP2T1 - GP2T1.5 - GP2H0.5 - GP2H1 - GP2H3.5	Gruppo 3 - GP3V0.5 - GP3V1 - GP3V1.5 - GP3V2
Gruppo 4 - GP4V0.5 - GP4V1 - GP4V1.5 - GP4V2	Gruppo 5 - GP5T4 - GP5T2.5 - GP5T1.5 - GP5H4 - GP5H2.5 - GP5H1.5	Gruppo 6 - GP6V0.5 - GP6V1 - GP6V1.5 - GP6V2
Gruppo 7 - GP7H1	Gruppo 8 - GP8H0.5 - GP8H1 - GP8T0.5 - GP8T1	Gruppo 9 - GP9H1

Appendix 3.A.5 San Giorgio south station (GS)

TECNOPENTA

TECNOPENTA s.r.l. con unico socio
Apparecchiature per la geologia tecnica - realizzazioni speciali

Stazione secondaria San Giorgio SUD installata sulla sommità arginale in corrispondenza della parte inferiore dell'idrometro storico.

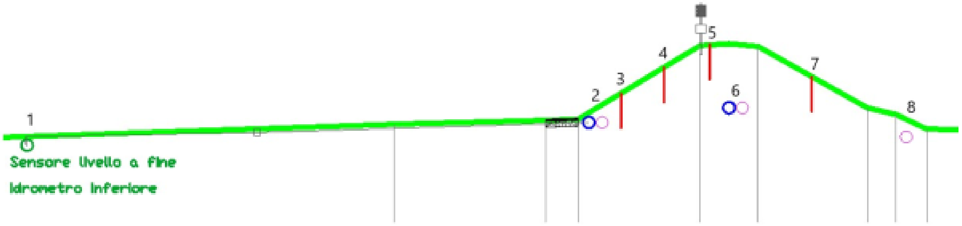

Sensori installati

Gruppo 1 - Sensore di livello I1-B1 in pozzetto locato alla base dell'idrometro storico	Gruppo 2 - GS2H1 - GS2T1	Gruppo 3 - GS3V0.5 - GS3V1 - GS3V1.5 - GS3V2
Gruppo 4 - GS4V0.5 - GS4V1 - GS4V1.5 - GS4V2	Gruppo 5 - GS5V0.5 - GS5V1 - GS5V1.5 - GS5V2	Gruppo 6 - GS6T4 - GS6H4
Gruppo 7 - GS7V0.5 - GS7V1 - GS7V1.5 - GS7V2	Gruppo 8 - GS8H1	

Appendix 3.A.6 San Giorgio north station (GN)

TECNOPENTA s.r.l. con unico socio
Apparecchiature per la geologia tecnica - realizzazioni speciali

Stazione secondaria San Giorgio NORD installata in corrispondenza di via San Mauretto

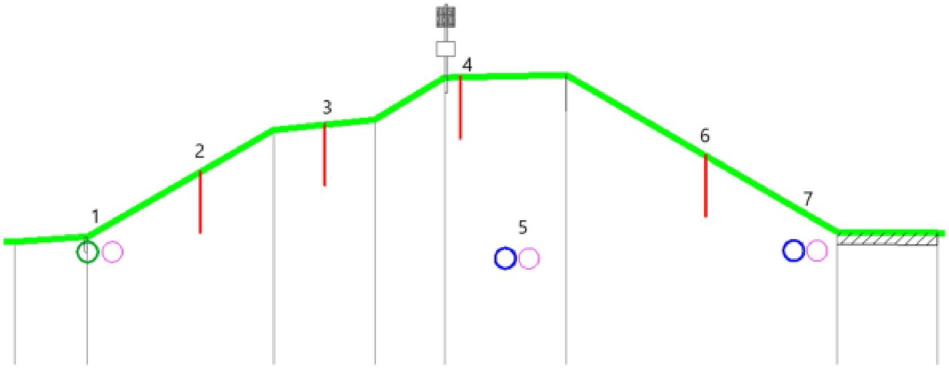

Sensori installati

Gruppo 1 - Sensore di livello I1-B1 - GN1H1	Gruppo 2 - GN2V0.5 - GN2V1 - GN2V1.5 - GN2V2	Gruppo 3 - GN3V0.5 - GN3V1 - GN3V1.5 - GN3V2
Gruppo 4 - GN4V0.5 - GN4V1 - GN4V1.5 - GN4V2	Gruppo 5 - GN5T4 - GN5H4	Gruppo 6 - GN6V0.5 - GN6V1 - GN6V1.5 - GN6V2
Gruppo 7 - GN7H1 - GN7T1		

Appendix 4.A Master table of laboratory sample properties

Sample ID	Station	Depth (m)	Descriptive soil classification (English)	Plastic / non-plastic behavior	LL	PL	PI	Final USCS class
GN1H1.0	N	1.0	Silt with fine sand and traces of medium sand	Non-plastic	NP	NP	NP	NP
GN2V0.5	N	0.5	Silt with traces of fine sand	Non-plastic	NP	NP	NP	NP
GN2V1.0	N	1.0	Silt with fine sand and traces of medium sand	Non-plastic	NP	NP	NP	NP
GN2V1.5	N	1.5	Silt with fine sand and traces of medium sand	Non-plastic	NP	NP	NP	NP
GN2V2.0	N	2.0	Silt with fine sand and traces of medium sand	Plastic	16	13	3	ML
GN2V2.0	N	2.0	Silt with fine sand and traces of medium sand	Plastic	16	13	3	ML
GN3V0.5	N	0.5	Silt with fine sand	Plastic	24	21	3	ML
GN3V1.0	N	1.0	Silt with fine sand and traces of medium sand	Plastic	21	19	2	ML
GN4V0.5	N	0.5	Silt with fine sand and medium sand	Non-plastic	NP	NP	NP	NP
GN4V1.0	N	1.0	Silt with fine sand and traces of medium sand	Non-plastic	NP	NP	NP	NP
GN4V1.5	N	1.5	Silt with fine sand and traces of medium sand	Non-plastic	NP	NP	NP	NP
GN4V2.0	N	2.0	Silt with fine sand and traces of medium sand	Non-plastic	NP	NP	NP	NP
GN4V2.0	N	2.0	Silt with fine sand and traces of medium sand	Non-plastic	NP	NP	NP	NP
GN5T4.0	N	4.0	Silt with fine sand and traces of medium sand	Non-plastic	NP	NP	NP	NP
GN6V0.5	N	0.5	Silt with traces of fine sand	Non-plastic	NP	NP	NP	NP
GN6V1.0	N	1.0	Silt with fine sand present	Non-plastic	NP	NP	NP	NP
GN6V1.5	N	1.5	Silt with fine sand	Non-plastic	NP	NP	NP	NP
GN6V2.0	N	2.0	Silt with fine sand present	Non-plastic	NP	NP	NP	NP
GN7H1.0	N	1.0	Silt with fine sand	Non-plastic	NP	NP	NP	NP
GP2H1.5	P	1.5	Fine sand with silt	Non-plastic	NP	NP	NP	NP
GP2H2.5	P	2.5	Silt with fine sand	Non-plastic	NP	NP	NP	NP
GP2H3.5	P	3.5	Silt with fine sand	Non-plastic	NP	NP	NP	NP
GP2T0.5	P	0.5	Silt with fine sand and traces of medium sand	Non-plastic	NP	NP	NP	NP
GP2T1.0	P	1.0	Silt with fine sand and traces of medium sand	Non-plastic	NP	NP	NP	NP
GP3V0.5	P	0.5	Fine sand with silt and traces of medium sand	Non-plastic	NP	NP	NP	NP

Sample ID	Station	Depth (m)	Descriptive soil classification (English)	Plastic / non-plastic behavior	LL	PL	PI	Final USCS class
GP3V1.0	P	1.0	Silt with fine sand and traces of medium sand	Non-plastic	NP	NP	NP	NP
GP3V1.5	P	1.5	Fine sand with silt and traces of medium sand	Non-plastic	NP	NP	NP	NP
GP3V1.5	P	1.5	Fine sand with silt	Non-plastic	NP	NP	NP	NP
GP3V2.0	P	2.0	Fine sand with silt	Non-plastic	NP	NP	NP	NP
GP3V2.0	P	2.0	Silt with fine sand and traces of medium sand	Non-plastic	NP	NP	NP	NP
GP4V0.5	P	0.5	Fine sand with silt and traces of medium sand	Non-plastic	NP	NP	NP	NP
GP4V1.0	P	1.0	Fine sand with silt and traces of medium sand	Non-plastic	NP	NP	NP	NP
GP4V1.5	P	1.5	Fine sand with silt and traces of medium sand	Plastic	24	22	2	ML
GP5H1.5	P	1.5	Fine sand with silt	Non-plastic	NP	NP	NP	NP
GP5H2.5	P	2.5	Fine sand with silt	Plastic	24	21	3	ML
GP5H4.0	P	4.0	Fine sand with silt	Plastic	25	24	1	ML
GP6V0.5	P	0.5	Fine sand with silt and traces of medium sand	Non-plastic	NP	NP	NP	NP
GP6V1.0	P	1.0	Silt with traces of medium sand	Non-plastic	NP	NP	NP	NP
GP6V1.5	P	1.5	Silt with fine sand	Non-plastic	NP	NP	NP	NP
GP6V2.0	P	2.0	Fine sand with silt	Non-plastic	NP	NP	NP	NP
GP7H1.0	P	1.0	Fine sand with silt and traces of medium sand	Plastic	28	23	5	ML
GP8 0.5	P	0.5	Silt with fine sand	Non-plastic	NP	NP	NP	NP
GP8 1.0	P	1.0	Silt with fine sand and traces of medium sand	Plastic	23	21	2	ML
GS2H1.0	S	1.0	Silt with fine sand and traces of medium sand	Non-plastic	NP	NP	NP	NP
GS3V0.5	S	0.5	Silt with fine sand and traces of medium sand	Non-plastic	NP	NP	NP	NP
GS3V1.0	S	1.0	Silt with fine sand and traces of medium sand	Non-plastic	NP	NP	NP	NP
GS3V1.5	S	1.5	Silt with fine sand and traces of medium sand	Non-plastic	NP	NP	NP	NP
GS3V2.0	S	2.0	Silt with fine sand and traces of medium sand	Non-plastic	NP	NP	NP	NP
GS5V0.5	S	0.5	Silt with fine sand and traces of medium sand	Plastic	13	11	2	ML
GS5V0.5	S	0.5	Fine sand with silt and traces of medium sand	Plastic	13	11	2	ML

Sample ID	Station	Depth (m)	Descriptive soil classification (English)	Plastic / non-plastic behavior	LL	PL	PI	Final USCS class
GS5V1.0	S	1.0	Fine sand with silt and traces of medium sand	Plastic	15	14	1	ML
GS5V1.0	S	1.0	Silt with fine sand and traces of medium sand	Plastic	15	14	1	ML
GS5V1.5	S	1.5	Silt with fine sand and traces of medium sand	Non-plastic	NP	NP	NP	NP
GS5V1.5	S	1.5	Silt with fine sand and traces of medium sand	Non-plastic	NP	NP	NP	NP
GS5V2.0	S	2.0	Silt with fine sand and traces of medium sand	Non-plastic	NP	NP	NP	NP
GS6T4.0	S	4.0	Silt with fine sand and traces of medium sand	Plastic	19	15	4	ML
GS7V0.5	S	0.5	Silt with fine sand present and traces of medium sand	Non-plastic	NP	NP	NP	NP
GS7V1.0	S	1.0	Silt with fine sand present and traces of medium sand	Non-plastic	NP	NP	NP	NP
GS7V1.5	S	1.5	Silt with fine sand	Non-plastic	NP	NP	NP	NP
GS7V2.0	S	2.0	Silt with fine sand present	Non-plastic	NP	NP	NP	NP
GS8H1.0	S	1.0	Silt with fine sand and medium sand	Non-plastic	NP	NP	NP	NP

Appendix 4.B Particle-size distribution data

Appendix 4.B – Part 1 of 8 (GN2V1.0 to GS3V0.5)

Sample ID	GN2V1.0	GN2V2.0	GN6V0.5	GN6V1.0	GN6V2.0	GP2T0.5	GP3V2.0	GS3V0.5
Depth (m)	**1**	**2**	**0.5**	**1**	**2**	**0.5**	**2**	**0.5**
101.6	100	100	100	100	100	100	100	100
76.2	100	100	100	100	100	100	100	100
50.8	100	100	100	100	100	100	100	100
38.1	100	100	100	100	100	100	100	100
25.4	100	100	100	100	100	100	100	100
19.1	100	100	100	100	100	100	100	100
12.7	100	100	100	100	100	100	100	100
9.52	100	100	100	100	100	100	100	100
4.76	100	100	100	100	100	100	100	100
2	100	100	100	100	100	100	100	100
0.84	100	100	100	100	100	100	100	100
0.42	99.94447529150472	100	100	100	100	99.78046103183316	100	98.5579589572934
0.25	98.33425874514158	99.55825510767532	100	100	100	98.6278814489572	99.17081260364843	96.83860232945091
0.177	88.83953359244863	97.01822197680839	98.89258028792912	99.22865013774104	99.17537108301265	94.73106476399562	96.01990049751244	91.73599556295063
0.105	63.29816768461965	80.12147984538929	97.78516057585824	98.40220385674931	97.96591533809786	84.68715697036225	84.74295190713102	78.5912368275097
0.074	60.24430871737923	78.07840971838763	97.12070874861571	96.74931129476583	96.5915338097856	77.00329308452251	75.95356550580432	70.32723239046034
0.04231320669737289	41.31189057863779	47.41439759715234	77.50519614421547	74.9191330658327	72.76664088820034	55.97781095169853	48.96947991550692	50.99776536502801
0.03142313728489964	29.44065765374188	38.29624421308459	69.90664750262572	63.45191882106239	61.51406755497348	40.76644928004132	28.06787263449787	37.13967695061822
0.02303455467206094	19.94367131382515	26.13870636766091	60.40846170063853	51.98470457629208	42.75977866626206	24.03395144121839	14.63112509670634	27.43901506053138
0.01670708916651355	12.8209315588876	17.02055298359315	47.11100157785647	40.51749033152176	31.5072053330352	16.42827060538979	8.65923730213232	17.73835317044453
0.01235135761265048	9.259561681418816	12.46147629155927	39.51245293626671	29.05027608675146	24.00548977755063	13.38599827105834	7.166265353488816	12.19511780468062
0.008838677161439741	5.698191803950041	7.902399599525393	31.91390429467697	21.40546659023791	16.50377422206606	10.3437259367269	5.673293404845314	9.423500121798654
0.006274430099204714	4.511068511460449	4.863015138169472	24.31535565308721	13.76065709372437	10.87748755545263	5.780317435229739	0	6.651882438916697
0.004349232267375871	0	3.343322907491512	16.71680701149745	8.027049971339219	7.126629777710342	0	0	5.266073597475719
0.003124944278786354	0	0	9.118258369907704	4.204645223082448	0	0	0	0
0.002218346035614317	0	0	7.218621209510266	0	0	0	0	0
0	0	0	0	0	0	0	0	0

Sample ID	GN2V1.0	GN2V2.0	GN6V0.5	GN6V1.0	GN6V2.0	GP2T0.5	GP3V2.0	GS3V0.5
Depth (m)	**1**	**2**	**0.5**	**1**	**2**	**0.5**	**2**	**0.5**
0	0	0	0	0	0	0	0	0
0	0	0	0	0	0	0	0	0
0	0	0	0	0	0	0	0	0
wL	**NP**	**NP**	**NP**	**NP**	**NP**	**NP**	**NP**	**NP**
wP	**NP**	**NP**	**NP**	**NP**	**NP**	**NP**	**NP**	**NP**
IP	**NP**	**NP**	**NP**	**NP**	**NP**	**NP**	**NP**	**NP**
Classification (USCS)	**NP**	**NP**	**NP**	**NP**	**NP**	**NP**	**NP**	**NP**

Appendix 4.B – Part 2 of 8 (GS3V1.0 to GS7V0.5)

Sample ID	GS3V1.0	GS3V1.5	GS3V2.0	GS5V0.5	GS5V1.0	GS5V1.5	GS5V2.0	GS7V0.5
Depth (m)	**1**	**1.5**	**2**	**0.5**	**1**	**1.5**	**2**	**0.5**
101.6	100	100	100	100	100	100	100	100
76.2	100	100	100	100	100	100	100	100
50.8	100	100	100	100	100	100	100	100
38.1	100	100	100	100	100	100	100	100
25.4	100	100	100	100	100	100	100	100
19.1	100	100	100	100	100	100	100	100
12.7	100	100	100	100	100	100	100	100
9.52	100	100	100	100	100	100	100	100
4.76	100	100	100	100	100	100	100	100
2	100	100	100	99.38990571270105	100	100	100	100
0.84	100	100	100	98.94620077648364	100	100	99.94447529150472	100
0.42	100	100	100	98.61342207432057	100	99.69574036511156	99.88895058300943	99.50221238938053
0.25	99.27817878956135	98.67183176535694	99.11160466407551	95.95119245701608	99.18610960390667	98.1237322515213	99.05607995558023	98.00884955752213
0.177	94.50305385896723	94.79800774764803	95.55802332037757	84.30393788130893	96.52740097666847	92.4949290060852	93.72570794003332	94.35840707964601
0.105	80.51082731815657	82.29109020475926	84.28650749583565	57.34886300610094	88.49701573521432	79.20892494929006	81.39922265408107	87.38938053097345
0.074	73.9033870072182	78.69396790260099	76.40199888950583	49.91680532445923	83.99348887683125	71.70385395537525	77.79011660188785	84.01548672566372
0.04231320669737289	48.10965585567929	57.25892593550596	52.52218185292629	32.02428484159742	57.03156680782672	44.87983904480166	53.08031485775875	67.21238938053096
0.03142313728489964	39.41513973718303	44.94517842249392	43.46663325759418	22.26078336550065	43.92086179453323	32.25738431345119	40.87794362609008	57.32821447162935
0.02303455467206094	24.92427953968927	32.63143090948189	31.39256846381802	12.49728188940387	34.0878330345631	21.03742455225078	28.6755723944214	34.26513968419226
0.01670708916651355	16.22976342119301	20.31768339646985	22.3370198684859	6.639181003745808	24.25480427459297	14.02494970150052	22.57438677858706	24.38096477529065
0.01235135761265048	8.984333322446131	17.23924651821685	16.29998747159782	5.66283085613613	17.69945176794623	8.41496982090031	13.42260835483555	21.08623980565677
0.008838677161439741	7.535247302696757	11.08237276171083	13.28147127315378	3.710130560916775	14.42177551462285	7.012474850750259	10.37201554691838	14.49678986638903
0.006274430099204714	4.637075263198004	8.003935883457821	7.244438876265695	0	7.8664230079761	0	7.321422739001208	7.90733992712129
0.004349232267375871	3.187989243448628	4.925499005204814	5.735180777043675	0	6.227584881314413	0	5.796126335042622	6.259977442304354
0.003124944278786354	0	3.386280566078309	0	0	0	0	0	0
0.002218346035614317	0	0	0	0	0	0	0	0
0	0	0	0	0	0	0	0	0

Sample ID	GS3V1.0	GS3V1.5	GS3V2.0	GS5V0.5	GS5V1.0	GS5V1.5	GS5V2.0	GS7V0.5
Depth (m)	**1**	**1.5**	**2**	**0.5**	**1**	**1.5**	**2**	**0.5**
0	0	0	0	0	0	0	0	0
0	0	0	0	0	0	0	0	0
0	0	0	0	0	0	0	0	0
wL	**NP**	**NP**	**NP**	**NP**	**NP**	**NP**	**NP**	**NP**
wP	**NP**	**NP**	**NP**	**NP**	**NP**	**NP**	**NP**	**NP**
IP	**NP**	**NP**	**NP**	**NP**	**NP**	**NP**	**NP**	**NP**
Classification (USCS)	**NP**	**NP**	**NP**	**NP**	**NP**	**NP**	**NP**	**NP**

Appendix 4.B – Part 3 of 8 (GS7V1.0 to GN4V)

Sample ID	GS7V1.0	GS7V1.5	GS7V2.0	GS8H1.0	GN2V	GN7H	GP2H	GN4V
Depth (m)	**1**	**1.5**	**2**	**1**	**1.5**	**1**	**2.5**	**0.5**
101.6	100	100	100	100	100	100	100	100
76.2	100	100	100	100	100	100	100	100
50.8	100	100	100	100	100	100	100	100
38.1	100	100	100	100	100	100	100	100
25.4	100	100	100	100	100	100	100	100
19.1	100	100	100	100	100	100	100	100
12.7	100	100	100	100	100	100	100	100
9.52	100	100	100	100	100	100	100	100
4.76	100	100	100	100	100	100	100	100
2	100	100	100	100	100	100	99.67231021299835	99.33811362382791
0.84	100	100	100	100	100	100	99.50846531949753	99.17264202978488
0.42	100	100	100	99.33333333333333	100	99.94484280198566	99.23539049699616	98.73138444567016
0.25	99.22523519645821	99.4550408719346	99.34354485776805	93.1111111111111	98.83849557522124	99.55874241588528	98.41616602949206	93.71207942636514
0.177	96.29219701162147	98.31062670299727	98.7417943107221	72.38888888888889	92.20132743362832	99.1726420297849	96.12233752048058	79.20573634859349
0.105	91.97565024903155	95.20435967302451	96.55361050328227	44.27777777777777	76.76991150442478	97.84886927744071	84.76242490442378	63.48593491450634
0.074	87.93580520199225	91.33514986376021	96.06126914660831	41.83333333333333	65.87389380530973	95.64258135686708	76.07864554888036	52.95091009376723
0.04231320669737289	63.60877697197109	62.63210247554304	72.72278187453884	27.57308823529412	38.13852211620076	73.71759514616659	48.69300492110076	37.65604668652454
0.03142313728489964	56.69477947501771	51.8334641176908	61.4769908630122	20.92897058823529	27.8308134361465	62.54826254826256	36.67004074305119	29.28803631174131
0.02303455467206094	46.32378322958764	33.83573352127038	42.73400584380117	14.28485294117647	20.10003192610581	47.65581908439052	24.64707656500162	20.92002593695808
0.01670708916651355	32.49578823568089	23.03709516341813	31.48821483227455	10.96279411764706	13.65771400107189	32.76337562051848	18.63559447597684	16.73602074956646
0.01235135761265048	25.58179073872751	14.03822986520792	23.99102082459014	7.640735294117646	9.792323246051547	25.31715388858246	9.618371342439659	10.46001296847904
0.008838677161439741	18.66779324177413	8.638910686281799	16.49382681690572	5.149191176470588	7.215396076037981	17.87093215664645	5.109759775671068	4.184005187391616
0.006274430099204714	11.75379574482075	6.839137626639757	12.74522981306351	3.488161764705882	3.350005321017635	10.42471042471042	2.104018731158674	3.138003890543711
0.004349232267375871	6.56829762210571	0	7.122334307300195	1.827132352941176	0.7730781510040694	4.840044125758412	0	1.046001296847904
0.003124944278786354	0	0	0	0	0	1.116933259790403	0	0
0.002218346035614317	0	0	0	0	0	0	0	0
0	0	0	0	0	0	0	0	0

Sample ID	GS7V1.0	GS7V1.5	GS7V2.0	GS8H1.0	GN2V	GN7H	GP2H	GN4V
Depth (m)	**1**	**1.5**	**2**	**1**	**1.5**	**1**	**2.5**	**0.5**
0	0	0	0	0	0	0	0	0
0	0	0	0	0	0	0	0	0
0	0	0	0	0	0	0	0	0
wL	**NP**	**NP**	**NP**	**NP**	**NP**	**NP**	**NP**	**NP**
wP	**NP**	**NP**	**NP**	**NP**	**NP**	**NP**	**NP**	**NP**
IP	**NP**	**NP**	**NP**	**NP**	**NP**	**NP**	**NP**	**NP**
Classification (USCS)	**NP**	**NP**	**NP**	**NP**	**NP**	**NP**	**NP**	**NP**

Appendix 4.B – Part 4 of 8 (GN2V to GN4V)

Sample ID	GN2V	GN4V	GN4V	GN1H	GN5T	GN6V	GP2T	GN4V
Depth (m)	**0.5**	**2**	**1**	**1**	**4**	**1.5**	**1**	**1.5**
101.6	100	100	100	100	100	100	100	100
76.2	100	100	100	100	100	100	100	100
50.8	100	100	100	100	100	100	100	100
38.1	100	100	100	100	100	100	100	100
25.4	100	100	100	100	100	100	100	100
19.1	100	100	100	100	100	100	100	100
12.7	100	100	100	100	100	100	100	100
9.52	100	100	100	100	100	100	100	100
4.76	100	100	100	100	100	100	100	100
2	100	100	100	100	100	100	100	100
0.84	100	100	100	100	100	100	100	100
0.42	100	100	99.66685174902831	100	99.55629506378258	100	100	100
0.25	99.16805324459234	98.50249584026622	97.7234869516935	98.94911504424779	97.39323349972268	100	99.38990571270105	98.11320754716981
0.177	92.95618413754853	84.74764281752634	85.73014991671293	95.29867256637168	92.12423738214088	99.16759156492786	95.06378258458125	84.57269700332964
0.105	76.81641708264004	57.62617859123682	61.13270405330371	84.73451327433628	83.4165280088741	98.1687014428413	82.4181919023849	65.98224195338513
0.074	67.0549084858569	47.47642817526344	56.30205441421432	79.70132743362832	81.30892956184137	95.78246392896783	72.04658901830283	58.10210876803551
0.04231320669737289	42.1778108123037	24.50621513164333	36.83342692811393	60.95959311732346	53.59215033767251	69.2169158451394	49.97305371697198	35.89938127196208
0.03142313728489964	31.63335810922777	18.85093471664872	25.73902122687479	51.6290431503862	40.67837917196829	50.20127962394726	38.61554150856925	26.69441171504873
0.02303455467206094	21.08890540615185	11.31056082998923	14.64461552563566	39.18830986113651	27.76460800626407	38.79189789123197	24.41865124806585	17.48944215813537
0.01670708916651355	13.1805658788449	7.540373886659488	10.20685324514	29.85775989419924	18.0792796319859	27.38251615851669	15.90051709176381	10.58571499045036
0.01235135761265048	7.908339527306944	4.71273367916218	5.769090964644351	23.6373932495744	11.6223940491338	19.77626167003983	10.22176098756245	5.983230211993681
0.008838677161439741	3.954169763653472	1.885093471664872	4.659650394520438	17.41702660494956	8.39395125770774	12.17000718156297	4.543004883361089	3.681987822765342
0.006274430099204714	1.318056587884491	0.942546735832436	2.44076925427261	9.641568299168506	6.779729861994714	6.465316315205329	3.123315857310749	2.531366628151173
0.004349232267375871	0	0	0	4.976293315699874	3.55128707056866	2.6621890709669	0.283937805210068	0.2301242389228338
0.003124944278786354	0	0	0	3.421201654543664	0	0	0	0
0.002218346035614317	0	0	0	0	0	0	0	0
0	0	0	0	0	0	0	0	0
0	0	0	0	0	0	0	0	0

Sample ID	**GN2V**	**GN4V**	**GN4V**	**GN1H**	**GN5T**	**GN6V**	**GP2T**	**GN4V**
Depth (m)	**0.5**	**2**	**1**	**1**	**4**	**1.5**	**1**	**1.5**
0	0	0	0	0	0	0	0	0
0	0	0	0	0	0	0	0	0
wL	**NP**	**NP**	**NP**	**NP**	**NP**	**NP**	**NP**	**NP**
wP	**NP**	**NP**	**NP**	**NP**	**NP**	**NP**	**NP**	**NP**
IP	**NP**	**NP**	**NP**	**NP**	**NP**	**NP**	**NP**	**NP**
Classification (USCS)	**NP**	**NP**	**NP**	**NP**	**NP**	**NP**	**NP**	**NP**

Appendix 4.B – Part 5 of 8 (GN4V to GPH)

Sample ID	GN4V	GS2H	GS5V	GP8	GP3V	GP4V	GP6V	GPH
Depth (m)	**2**	**1**	**1.5**	**0.5**	**1**	**1**	**1.5**	**3.5**
101.6	100	100	100	100	100	100	100	100
76.2	100	100	100	100	100	100	100	100
50.8	100	100	100	100	100	100	100	100
38.1	100	100	100	100	100	100	100	100
25.4	100	100	100	100	100	100	100	100
19.1	100	100	100	100	100	100	100	100
12.7	100	100	100	100	100	100	100	100
9.52	100	100	100	100	100	100	100	100
4.76	100	100	100	100	100	100	100	100
2	99.7780244173141	100	100	100	100	100	100	100
0.84	99.44506104328525	100	100	100	100	100	100	100
0.42	99.05660377358491	100	100	100	99.72222222222223	100	100	100
0.25	98.11320754716982	98.89258028792912	98.33978970669618	99.72283813747228	98.66666666666667	99.16759156492786	99.28453494771601	99.06487434248977
0.177	93.61820199778026	94.07530454042082	92.97177642501383	99.16851441241685	90.33333333333334	96.00443951165371	98.01871216290589	97.25306838106371
0.105	81.24306326304108	80.0110741971207	78.63862755949086	96.6740576496674	66.88888888888889	86.57047724750277	94.11117226197028	91.46697837521917
0.074	74.08435072142066	71.98228128460687	73.54731599335915	94.2350332594235	57.50000000000001	78.96781354051053	90.25866813428729	87.31735827001754
0.04231320669737289	55.64376617499923	51.6305546974979	52.8843299372793	71.12906412592478	36.80201931518876	55.67248230536799	64.90065777171314	63.09963213806856
0.03142313728489964	46.94942771015559	37.44633637400946	44.16713269487062	56.31050909969045	27.71510096575943	46.28947966963181	54.20274715000219	56.1656066283907
0.02303455467206094	35.35697642369742	28.9358053799164	35.44993545246195	41.49195407345612	14.08472344161545	33.77880948865024	36.37289611381726	45.7645683638739
0.01670708916651355	26.66263795885379	20.42527438582335	26.73273821005328	26.67339904722179	8.405399473222126	24.39580685291406	25.6749854921063	35.36353009935711
0.01235135761265048	20.86641231562471	11.91474339173029	18.0155409676446	19.26412153410463	3.861940298507463	15.01280421717788	18.54304507763233	28.42950458967924
0.008838677161439741	15.07018667239562	7.659477894683755	9.298343725235922	11.85484402098746	1.590210711150131	8.757469126687097	7.845134455921371	21.49547908000137
0.006274430099204714	6.375848207551994	3.404212397637224	4.939745104031584	6.29788588614959	0	5.629801581441707	4.279164248684383	11.09444081548458
0.004349232267375871	2.02867897513018	1.985790565288381	2.034012689895357	2.593247129591008	0	2.502134036196314	2.49617914506589	5.893921683226183
0.003124944278786354	0	0	0	0	0	0.9383002635736176	0	2.426908928387252
0.002218346035614317	0	0	0	0	0	0	0	0
0	0	0	0	0	0	0	0	0

Sample ID	**GN4V**	**GS2H**	**GS5V**	**GP8**	**GP3V**	**GP4V**	**GP6V**	**GPH**
Depth (m)	**2**	**1**	**1.5**	**0.5**	**1**	**1**	**1.5**	**3.5**
0	0	0	0	0	0	0	0	0
0	0	0	0	0	0	0	0	0
0	0	0	0	0	0	0	0	0
wL	**NP**	**NP**	**NP**	**NP**	**NP**	**NP**	**NP**	**NP**
wP	**NP**	**NP**	**NP**	**NP**	**NP**	**NP**	**NP**	**NP**
IP	**NP**	**NP**	**NP**	**NP**	**NP**	**NP**	**NP**	**NP**
Classification (USCS)	**NP**	**NP**	**NP**	**NP**	**NP**	**NP**	**NP**	**NP**

Appendix 4.B – Part 6 of 8 (GP5H to GP6V)

Sample ID	GP5H	GP3V	GP4V	GP6V	GP3V	GP6V	GP2H	GP6V
Depth (m)	**1.5**	**1.5**	**0.5**	**0.5**	**2**	**2**	**1.5**	**1**
101.6	100	100	100	100	100	100	100	100
76.2	100	100	100	100	100	100	100	100
50.8	100	100	100	100	100	100	100	100
38.1	100	100	100	100	100	100	100	100
25.4	100	100	100	100	100	100	100	100
19.1	100	100	100	100	100	100	100	100
12.7	100	100	100	100	100	100	100	100
9.52	100	100	100	100	100	100	100	100
4.76	100	100	100	100	100	100	100	100
2	99.39058171745152	100	100	100	100	100	100	100
0.84	99.00277008310249	100	100	100	100	100	100	100
0.42	98.5595567867036	99.44506104328524	98.89258028792912	99.72390944229707	100	100	99.66850828729282	99.2260917634052
0.25	97.6731301939058	98.77913429522752	97.3421926910299	98.72998343456653	99.55727725511898	99.28216454997239	98.95027624309392	98.67330016583747
0.177	94.34903047091412	94.173140954495	92.30343300110741	92.8768636112645	94.96402877697841	98.45389287686362	94.64088397790056	97.2360420121614
0.105	87.0360110803324	82.24195338512763	79.45736434108525	76.14577581446714	79.7454344216934	92.37990060739924	79.77900552486189	92.7584300718629
0.074	81.82825484764543	71.58712541620422	71.98228128460684	67.36609607951408	68.45600442722744	84.92545554942022	68.95027624309392	88.72305140961856
0.04231320669737289	58.69275205390885	48.76787596198508	50.3708275850059	48.56050992148042	45.32424990248192	57.71053783604147	46.27909855079175	67.30177034057104
0.03142313728489964	49.01812259447333	34.59116783350105	41.88136226169029	35.21971049250229	31.83488981245755	44.28948252533415	32.82587222788717	56.78586872485681
0.02303455467206094	39.3434931350378	23.24980133071382	33.39189693837469	27.2152308351154	21.04340174043804	34.22369104230366	19.37264590498259	42.76466657057118
0.01670708916651355	26.44398718912376	14.7437764536234	24.90243161505909	19.21075117772852	12.9497856864234	20.80263573159635	13.99135537582076	32.24876495485696
0.01235135761265048	16.76935772968825	6.237751576532975	16.41296629174349	13.87443140613727	7.554041650413652	14.09210807624269	8.610064846658931	25.23816387771414
0.008838677161439741	10.31960475673123	4.820080763684572	7.923500968427891	5.869951748750383	3.507233623406339	9.059212334727441	3.228774317497098	14.72226226199992
0.006274430099204714	3.86985178377421	1.984739137987765	3.678768306770094	3.201791862954753	0.8093616054014627	5.70394850705061	1.883451685206641	7.7116611848571
0.004349232267375871	2.257413540534956	0	0.8489465323315599	1.86771192005694	0	2.348684679373781	0	5.959010915571395
0.003124944278786354	0	0	0	0	0	0	0	2.453710376999986
0.002218346035614317	0	0	0	0	0	0	0	0
0	0	0	0	0	0	0	0	0

Sample ID	GP5H	GP3V	GP4V	GP6V	GP3V	GP6V	GP2H	GP6V
Depth (m)	**1.5**	**1.5**	**0.5**	**0.5**	**2**	**2**	**1.5**	**1**
0	0	0	0	0	0	0	0	0
0	0	0	0	0	0	0	0	0
0	0	0	0	0	0	0	0	0
wL	**NP**	**NP**	**NP**	**NP**	**NP**	**NP**	**NP**	**NP**
wP	**NP**	**NP**	**NP**	**NP**	**NP**	**NP**	**NP**	**NP**
IP	**NP**	**NP**	**NP**	**NP**	**NP**	**NP**	**NP**	**NP**
Classification (USCS)	**NP**	**NP**	**NP**	**NP**	**NP**	**NP**	**NP**	**NP**

Appendix 4.B – Part 7 of 8 (GP3V to GP5H)

Sample ID	GP3V	GP3V	GS5V	GN2V	GN3V	GN3V	GP4V	GP5H
Depth (m)	**0.5**	**1.5**	**1**	**2**	**0.5**	**1**	**1.5**	**2.5**
101.6	100	100	100	100	100	100	100	100
76.2	100	100	100	100	100	100	100	100
50.8	100	100	100	100	100	100	100	100
38.1	100	100	100	100	100	100	100	100
25.4	100	100	100	100	100	100	100	100
19.1	100	100	100	100	100	100	100	100
12.7	100	100	100	100	100	100	100	100
9.52	100	100	100	100	100	100	100	100
4.76	100	100	100	100	100	100	100	100
2	100	100	100	100	100	100	100	100
0.84	99.61261759822911	100	100	100	100	100	100	100
0.42	98.89319313779745	100	99.44690265486726	100	100	100	99.55947136563877	100
0.25	97.62036524626453	99.55727725511898	96.23893805309734	99.55825510767532	98.89073765945646	99.5	98.84361233480176	98.94561598224195
0.177	94.07858328721638	97.01162147205312	89.32522123893806	97.01822197680839	96.78313921242373	95.77777777777777	95.26431718061674	96.44839067702551
0.105	84.33868289983397	87.16104039845047	73.17477876106196	80.12147984538929	86.85524126455907	78.44444444444443	83.48017621145375	88.62375138734738
0.074	75.70558937465411	78.41726618705036	64.98893805309736	78.07840971838763	77.09373266777592	71.33333333333331	75.33039647577093	81.46503884572697
0.04231320669737289	56.09131100069249	54.33583928704787	40.46749521741546	47.41439759715234	48.73652069502122	52.28959276018097	51.19027820214809	60.20916382948603
0.03142313728489964	47.14056988356071	42.12553832366633	32.78379359385556	38.29624421308459	36.70281188143574	41.04451904831409	42.26174130642459	47.39870344023368
0.02303455467206094	38.18982876642893	29.91523736028479	25.10009197029567	26.13870636766091	26.17331666954843	29.79944533644722	30.35702544545992	31.38562795366825
0.01670708916651355	29.23908764929715	20.75751163774862	17.41639034673577	17.02055298359315	18.6522486610575	21.36564005254706	21.42848854973641	21.77778266172899
0.01235135761265048	20.28834653216537	14.65236115605785	9.732688723175867	12.46147629155927	12.63539425426476	15.74310319661362	15.47613061925408	12.16993736978973
0.008838677161439741	14.32118578741085	11.59978591521247	5.89083791139592	7.902399599525393	9.62696705086839	10.12056634068019	9.523772688771741	5.764707175163556
0.006274430099204714	9.845815228844955	5.494635433521695	3.329604036875955	4.863015138169472	5.114326245773832	4.498029484746751	5.059504240909987	2.562092077850469
0.004349232267375871	3.878654484090438	2.442060192676309	0.7683701623559896	3.343322907491512	2.10589904237746	3.092395270763391	2.083325275668818	0.9607845291939259
0.003124944278786354	0.8950741117131779	0.9157725722536157	0	0	0	0.2811268427966718	0	0
0.002218346035614317	0	0	0	0	0	0	0	0
0	0	0	0	0	0	0	0	0
0	0	0	0	0	0	0	0	0

Sample ID	GP3V	GP3V	GS5V	GN2V	GN3V	GN3V	GP4V	GP5H
Depth (m)	**0.5**	**1.5**	**1**	**2**	**0.5**	**1**	**1.5**	**2.5**
0	0	0	0	0	0	0	0	0
0	0	0	0	0	0	0	0	0
wL	**NP**	**NP**	**NP**	**16**	**24**	**21**	**24**	**24**
wP	**NP**	**NP**	**NP**	**13**	**21**	**19**	**22**	**21**
IP	**NP**	**NP**	**NP**	**3**	**3**	**2**	**2**	**3**
Classification (USCS)	**NP**	**NP**	**NP**	**ML**	**ML**	**ML**	**ML**	**ML**

Appendix 4.B – Part 8 of 8 (GP5H to GS6T)

Sample ID	GP5H	GP7H	GP8	GS5V	GS5V	GS6T
Depth (m)	**4**	**1**	**1**	**0.5**	**1**	**1**
101.6	100	100	100	100	100	100
76.2	100	100	100	100	100	100
50.8	100	100	100	100	100	100
38.1	100	100	100	100	100	100
25.4	100	100	100	100	100	100
19.1	100	100	100	100	100	100
12.7	100	100	100	100	100	100
9.52	100	100	100	100	100	100
4.76	100	100	100	100	100	100
2	100	99.88925802879291	100	100	100	100
0.84	100	99.77851605758582	100	99.3912562257886	100	100
0.42	100	99.39091915836102	100	98.50581073602656	100	100
0.25	99.16759156492786	97.2314507198228	99.61154273029966	96.45821804095185	99.18610960390667	98.8907376594564 6
0.177	96.61487236403995	91.0299003322259	99.11209766925637	89.92805755395683	96.52740097666847	94.2318358291736
0.105	88.62375138734738	81.7829457364341	97.11431742508323	78.47260653016049	88.49701573521432	83.08374930671104
0.074	83.0188679245283	74.58471760797342	95.5604883462819	72.38516878804649	83.99348887683125	76.65002773155852
0.04231320669737289	62.81853909221348	53.2330141358869	72.48837746372918	49.06681124677971	57.03156680782672	53.63716267878134
0.03142313728489964	53.00314235905513	44.45834147612533	61.16206848502149	40.50864649443441	43.92086179453323	41.58386769478553
0.02303455467206094	43.18774562589677	35.68366881636374	46.06032318007792	29.09776015797401	34.0878330345631	29.53057271078973
0.01670708916651355	30.10054998168563	23.98410527001498	30.95857787513434	20.53959540562872	24.25480427459297	20.49060147279287
0.01235135761265048	23.55695215958006	18.13432349684059	19.63226889642665	14.83415223739852	17.69945176794623	14.46395398079497
0.008838677161439741	13.7415554264217	12.28454172366621	12.08139624395487	9.12870906916832	14.42177551462285	8.437306488797063
0.006274430099204714	7.197957604316131	6.434759950491824	6.418241754601022	4.84962669299567	7.8664230079761	3.917320869798638
0.004349232267375871	2.29025923773695	2.047423620611035	2.642805428365126	1.99690510888057	6.227584881314413	0.9039971237996853
0.003124944278786354	2.29025923773695	0	0	0	0	0
0.002218346035614317	0	0	0	0	0	0
0	0	0	0	0	0	0

Sample ID	GP5H	GP7H	GP8	GS5V	GS5V	GS6T
Depth (m)	**4**	**1**	**1**	**0.5**	**1**	**1**
0	0	0	0	0	0	0
0	0	0	0	0	0	0
0	0	0	0	0	0	0
wL	**25**	**28**	**23**	**13**	**15**	**19**
wP	**24**	**23**	**21**	**11**	**4**	**15**
IP	**1**	**5**	**2**	**2**	**1**	**4**
Classification (USCS)	**ML**	**ML**	**ML**	**ML**	**ML**	**ML**